

5-2017

Synthesis and fundamental property studies of energy material under high pressure.

Meysam Akhtar
University of Louisville

Follow this and additional works at: <https://ir.library.louisville.edu/etd>

 Part of the [Condensed Matter Physics Commons](#)

Recommended Citation

Akhtar, Meysam, "Synthesis and fundamental property studies of energy material under high pressure." (2017). *Electronic Theses and Dissertations*. Paper 2621.
<https://doi.org/10.18297/etd/2621>

This Doctoral Dissertation is brought to you for free and open access by ThinkIR: The University of Louisville's Institutional Repository. It has been accepted for inclusion in Electronic Theses and Dissertations by an authorized administrator of ThinkIR: The University of Louisville's Institutional Repository. This title appears here courtesy of the author, who has retained all other copyrights. For more information, please contact thinkir@louisville.edu.

SYNTHESIS AND FUNDAMENTAL PROPERTY STUDIES OF ENERGY
MATERIAL UNDER HIGH PRESSURE

By

Meysam Akhtar
B.S., Shahid Beheshti University, 2007
M.S., University of Louisville, 2013

A Dissertation
Submitted to the Faculty of the
College of Arts and Sciences of the University of Louisville
in Partial Fulfillment of the Requirements
for the Degree of

Doctor of Philosophy
in Physics

Department of Physics and Astronomy
University of Louisville
Louisville, Kentucky

May 2017

Copyright 2002 by Meysam Akhtar

All rights reserved

SYNTHESIS AND FUNDAMENTAL PROPERTY STUDIES OF ENERGY
MATERIAL UNDER HIGH PRESSURE

By

Meysam Akhtar
B.S., Shahid Beheshti University, 2007
M.S., University of Louisville, 2013

A Dissertation Approved on

April 19, 2017

by the following Dissertation Committee:

Dr. Gamini Sumanasekera

Dr. Jacek B. Jasinski

Dr. Chakram S. Jayanthi

Dr. Ming Yu

Dr. Jinjun Liu

ACKNOWLEDGMENTS

I would like to express my deepest appreciation and thanks to both of my advisors Dr. Gamini Sumanasekera, and Dr. Jacek Jasinski. I am grateful to Dr. Gamini for his great support and guidance throughout my entire PhD program. In science, he is exceptionally knowledgeable and has a great drive for developing homemade equipment and experimental setup as they become required in a project. I am also thankful to Dr. Jasinski whose invaluable mentoring and encouragement were vital to the completion of this dissertation. I have been inspired by his efforts in contributing to the scientific community. I would like to acknowledge my Ph.D. committee members Dr. Chakram S. Jayanthi, Dr. Ming Yu, and Dr. Jinjun Liu for their valuable comments and suggestions. My particular thanks go to Dr. Jayanthi, Chair of the Department of Physics and Astronomy, for the discussions about my research work and PhD career in many occasions. I also wish to express my gratitude to Dr. Chris Davis, Graduate Program Director who is a great resource for graduate students in UofL Physics Department, and his advice was essential in achieving my academic goals.

My thanks also go to Dr. Mahendra Sunkara, Director of the Conn Center for Renewable Energy Research, who gave me the opportunity to be a member of the Conn-Center family. I have received generous financial support from Conn Center during my graduate studies. I would also like to thank Dr. Andriy Durygin, who trained me in high-pressure experimental methods using diamond anvil cell in CeSMEC at Florida

International University. Dr. Madhu Menon performed the theoretical DFT calculations required in my work. I am thankful for his contribution and insightful comments. I am also grateful to Ms. Afsar Safaeian, my high school mathematics teacher. Every encounter with math is a reminder of her great efforts in teaching me. I would like to acknowledge the support from School of Interdisciplinary and Graduate Studies through “doctoral dissertation completion award” and the support from “John Dillon Jr Physics Fellowship”. I am indebted to administrative and technical staff from Physics Department, and Conn Center, Mary Gayle Wrocklage, Rea Diehlmann, Eunice De Lourdes Salazar, Andrew Marsh, Rodica McCoy, and Joshua Rimmer for their assistance.

I was lucky to work with wonderful research associates and post-doctoral fellows during my research. I wish to express a sincere thank you to Dr. Bijandra Kumar, Dr. Ramchandra K. Rao, Dr. John Samuel Dilip Jangam, Dr. Dominika Ziolkowska, and Dr. Ruvini Dharmadasa. I am thankful to my former and current labmates, George Anderson, Ruwantha Jayasinghe, Venkat Kalyan Vendra, Swathi Sunkara, Ruchira Dharmasena, Rong Zhao, Sahar Pishgar, and Brandon Lavery.

My deepest gratitude and love to Farzaneh Hoveyda, my love, life partner, and soulmate who has been a constant source of encouragement and support. She also helped me in writing this dissertation through great discussion about various scientific aspects. I am heartily thankful to my parents, Faramarz, Soroor, and my brother, Misagh, for tremendous emotional support.

ABSTRACT

SYNTHESIS AND FUNDAMENTAL PROPERTY STUDIES OF ENERGY MATERIAL UNDER HIGH PRESSURE

Meysam Akhtar

April 19, 2017

Recently, high-pressure science and technology has flourished and rapidly advanced to impact a wide domain of materials and physical sciences. One of the most substantial technological developments is the integration of samples at ultrahigh pressure with a wide range of in-situ probing techniques. Applications of extreme pressure have significantly enriched our understanding of the electronic, phonon, and doping effects on the newly emerged two-dimensional (2D) materials. Under high pressure, materials' atomic volume radically decreases, and electronic density rises, which will lead to extraordinary chemical reaction kinetic and mechanisms. The promising capability of high pressure combine with the significance of novel emerging 2D materials in energy-related research was the main motivation of this dissertation.

Firstly, the application of high pressure to enable the direct synthesis of α -AgGaO₂ through a reaction of Ag₂O and Ga₂O₃ is demonstrated. The synthesized samples were extensively characterized, and their crystal phase and chemical composition were confirmed. Especially, the rhombohedral delafossite crystal phase of the prepared sample was verified by electron diffraction. The vibrational phonon modes

were investigated using a combination of *ab initio* density functional theory (DFT) and experimental Raman measurement. In addition, using a modified DFT to calculate the electronic band structure of α -AgGaO₂ reported a more accurate value of theoretical¹ band gap than those have been reported previously.

Two-dimensional (2D) materials with efficient ion transport between the layers and the large surface areas have demonstrated promise for various energy-related applications. Few-layer black phosphorus (phosphorene), as a novel two-dimensional (2D) material, is gaining researchers' attention due to the exceptional properties, including puckered layer structure, widely tunable band gap, strong in-plane anisotropy, and high carrier mobility. Phosphorene application expanded from energy storage and conversion devices to thermoelectrics, optoelectronic and spintronic to sensors and actuators. Several recent theoretical studies have indicated that strain engineering can be a viable strategy to tune the electronic structure of phosphorene. Although several theoretical studies have predicted an electronic phase transition such as direct-indirect bandgap and semiconductor-metal transitions, there is not experimental study to indicate the transition.

Next, in this dissertation, a systematic experimental study of in situ high-pressure Raman and PL spectroscopy of phosphorene was reported. Furthermore, short transport growth of bulk black phosphorus and also, liquid-phase exfoliation technique to preparing few-layer black phosphorus was described. The study motivated by a better understanding of high-pressure effects on optical properties and band structure of this

¹ Performed by Dr. Madhu Menon (Center for Computational Sciences at the University of Kentucky)

material system. This study help to verify theoretical predictions and to enhance fundamental understanding of relationships between strain and electronic band structure, enabling rational strain engineering towards additional functionalities and device applications of phosphorene and few-layer BP. In situ characterization techniques are invaluable for a fundamental understanding of materials, their processing, and functionalities.

Three-dimensional architecture of graphene has also attracted considerable attentions as an effective way to utilize the unique inherent properties of graphene sheets in practical applications. Three-dimensional graphene-based materials offer an easy and versatile platform for functionalization and integration into devices. Furthermore, the interlocking of graphene sheets into 3D structures solve the restacking issue and make 3D graphene-based materials more compatible with conventional material processing.

Finally, in the dissertation, we report a novel, inexpensive, and highly scalable, approach of fabricating a three-dimensional graphene network (foam) via pyrolysis of organic materials as the source of carbon. A template-assisted method to prepare and tune the properties of a high-quality 3D graphene network was described. In this simple method, the 3D graphene foam is synthesized in a controlled environment by thermal decomposition of the organic materials in the presence of Ni foam which plays a dual role of catalyst and 3D template. This technique can efficiently facilitate and control the in situ nitrogen doping of 3D graphene structure by adjusting the growth parameters and choosing the right organic materials (i.e. nitrogen-containing organic acids). In this work, inexpensive organic materials including caffeine ($C_8H_{10}N_4O_2$), urea (CH_4N_2O) and acetaminophen ($C_8H_9NO_2$) were used with a citric acid solution as the source of carbon

and nitrogen. Nitrogenation of 3D graphene foam create an effective improvement of properties which is suitable for an extensive range of new energy and environmental applications. Our Raman analysis indicated an improvement of graphene network quality with an increase of synthesis temperature between 650 °C and 1000 °C. Both Raman and TEM study (HRTEM, SAED, and EELS) showed uniform coverage and high crystallinity of multilayered graphitic shells formed in samples synthesis at 1000 °C. The motivation for this 3D graphene research is to use in-situ high-pressure measurements to study fundamental properties of these materials including its vibrational structures, doping and functionalization. With its distinct Raman signatures dependent on the quality and structure, defect distribution, as well types of dopants and their concertation, 3D graphene seems well-suited for high-pressure in-situ Raman studies. These type of measurements are proposed as part of the future, follow-up research.

TABLE OF CONTENTS

	PAGE
ACKNOWLEDGMENTS	iii
ABSTRACT.....	v
LIST OF TABLES	x
LIST OF FIGURES	xi
CHAPTER 1: BACKGROUND.....	1
1.1 High-Pressure Physics and Chemistry	1
1.2 The Nobel Prizes for High-Pressure Research	6
1.3 Kinetics, Thermodynamics and Metastability	6
1.4 Semiconductors under High Pressure	7
1.5 Conditions for Stable Phases	8
1.6 Rhombohedral α -AgGaO ₂ (Semiconductor Compounds with ABC ₂ Form).....	10
1.7 Three-Dimensional (3D) Graphene Architecture	11
1.8 Few-Layer Black Phosphorus (Phosphorene).....	13
CHAPTER 2: EXPERIMENTAL METHODS	15
2.1 High-Pressure Equipment.....	15
2.2 Diamond Anvil Cell (DAC).....	15

2.3 Characterization Equipment	29
2.4 Synthesis Method.....	41
CHAPTER 3: RESULTS AND DISCUSSION.....	52
3.1 Rhombohedral α -AgGaO ₂	52
3.2 Three-Dimensional (3D) Graphene Architecture	68
3.3 Phosphorene.....	83
CHAPTER 4: SUMMARY AND OUTLOOK.....	101
REFERENCES	106
CURRICULUM VITAE	129

LIST OF TABLES

	PAGE
Table 1.1 In-situ High Pressure Probes with references.	10
Table 2.1 The Wavelength Ranges and Sources of the Radiation.	30
Table 2.2 List of samples prepared for this work.....	43
Table 3.1 Crystallographic Parameters Obtained for the DFT-Optimized α -AgGaO ₂	64
Table 3.2 Experimental and calculated Raman modes.	67

LIST OF FIGURES

	PAGE
Figure 1.1 Range of pressure in the universe and obtainable range in available laboratory equipment [3,4,6-12].....	2
Figure 1.2 High pressure impact on materials and its applications in materials science. .	3
Figure 1.3 Phenomena under High Pressure [30].	6
Figure 1.4 Energy Profile Diagram of a Phase Transformation.....	7
Figure 2.1 Schematics of the diamond anvil cell (DAC) and a photograph of our gas membrane driven DAC. Typical DAC is composed of two opposed diamond anvils with a metallic gasket in between providing a small chamber for the sample.....	16
Figure 2.2 Magnified Photograph of a Diamond Anvil under Optical Microscope.	18
Figure 2.3 Schematic of two diamond anvils with the standard design cut (Culet and Table of the Anvils is indicated.	18
Figure 2.4 Few Different Diamond Anvil Designs and Cuts that is commercially available from Almax easyLab Inc).....	19
Figure 2.5 Increasing the pressure inside the sample chamber by applying a force onto the pistons.	20
Figure 2.6 Top View through Diamonds with Optical Microscope Showing the Misalignment of Anvils.	21

Figure 2.7 Alignment of the diamond anvils and Loading Samples (Powder) in Gasket Hole (Sample Chamber) under the Microscope.....	22
Figure 2.8 Small Hole at the Center of the Metallic Gasket as a Sample Chamber.	23
Figure 2.9 The Micro EDM System and Optical Zoom Microscope.....	24
Figure 2.10 Internal Resistive Heater DAC System and the External Furnace that we used for temperature below 300 °C.....	26
Figure 2.11 Compact resistive heater (80 W), heater components, and DC power supply.	26
Figure 2.12 Burned heater components due to excess of current into the metal resistor.	27
Figure 2.13 Right: Ruby Photoluminescence Spectrum undergo a Red-Shift by Increasing the Pressure. Right: The gas pressure in the membrane of the DAC can be calibrated to be a scale of the sample pressure.	28
Figure 2.14 Top Row: SEM Images of Two different Ruby Chips and Photograph of Ruby Chips inside Gasket Hole. Bottom Row: The Gas Controller and Gas Membrane along with the DAC.	29
Figure 2.15 The sketch shows different forms of energy exchange between a photon and the Sample.....	31
Figure 2.16 Raman spectra energy states diagram.....	32
Figure 2.17 Photoluminescence energy states diagram.	33
Figure 2.18 Our modified Raman and PL system for in situ high-pressure measurements.	34
Figure 2.19 Our developed optical setup for in situ high-pressure UV/Vis spectroscopy.	35

Figure 2.20 Testing Optical Setup for In Situ High-Pressure UV/Vis Spectroscopy. Transmission Absorption Spectra of a Gasket Hole (200 μm in diameter) Covered by Orange Filter.	36
Figure 2.21 Temperature-Pressure diagram representing conditions used in our DAC-based $\alpha\text{-AgGaO}_2$ synthesis experiments. Each square represents one experiment and its specific conditions. Green check mark denotes formation of rhombohedral $\alpha\text{-AgGaO}_2$. Red crosses show experiments, which did not produce rhombohedral $\alpha\text{-AgGaO}_2$	44
Figure 2.22 Schematic image of single graphene sheet and graphite layers.	44
Figure 2.23 Chemical Vapor Deposition System setup. It was used for both CVD and the developed pyrolysis methods.	45
Figure 2.24 Optical and scanning electron microscopy (SEM) images of nickel foam.	46
Figure 2.25 Photograph of three-dimensional graphene foams fabricated at 500, 650, 800, and 1000 $^\circ\text{C}$ temperature and with different pre-treatment of nickel surface.	46
Figure 2.26 Nickel foam (center), three-dimensional graphene before (left) and after (right) etching the nickel template.	47
Figure 2.27 Molecular structure and chemical formula of organic precursors used for graphene growth.	47
Figure 2.28 Vacuum system for synthesis of black phosphorus by short way transport reaction methods.	49
Figure 2.29 The tube furnace and the temperature profile that was used to synthesis black phosphorus.	50
Figure 2.30 Pyrex tubes before sealing and evacuated glass (Pyrex) tube after annealing at 600 $^\circ\text{C}$	51

Figure 3.1 | Representative Raman spectra of various samples: (a) Ag_2O ($T = 600\text{ }^\circ\text{C}$, $P = 10\text{ GPa}$), (b) Ga_2O_3 ($T = 600\text{ }^\circ\text{C}$, $P = 10\text{ GPa}$), (c) Mixed powder of $\text{Ag}_2\text{O} + \text{Ga}_2\text{O}_3$ (1:1, $T = 600\text{ }^\circ\text{C}$, $P = 10\text{ GPa}$), (d) Mixed powder of $\text{Ag}_2\text{O} + \text{Ga}_2\text{O}_3$ (3:1, $T = 600\text{ }^\circ\text{C}$, $P = 10\text{ GPa}$), (e) Mixed powder of $\text{Ag}_2\text{O} + \text{Ga}_2\text{O}_3$ (1:1, $T = 480\text{ }^\circ\text{C}$, $P = 10\text{ GPa}$), (f) Mixed powder of $\text{Ag}_2\text{O} + \text{Ga}_2\text{O}_3$ (1:2, $T = 600\text{ }^\circ\text{C}$, $P = \text{ambient}$). Vertical red lines represent the location of our theoretically calculated Raman modes. Vertical light blue lines show the positions of Raman modes calculated by Kumar and Gupta [136]. Vertical dark blue lines show the location of Raman peaks measured by Nagarajan and Tomar [80]...... 52

Figure 3.2 | Raman spectra of pure silver (I) oxide before (top three curves) and after (bottom curve) DAC experiment. Before applying high pressure, Ag_2O is unstable under the illumination of 633 nm laser during Raman measurements. Hence, several shown spectra, measured from the same area at different times differ from each other (top three curves). However, after the high-pressure experiment, Ag_2O is stable, and its spectrum (bottom curve) does not change under laser illumination. The spectral regions shaded in yellow indicate the location of four peaks characteristic of rhombohedral $\alpha\text{-AgGaO}_2$ 53

Figure 3.3 | Gallium (III) oxide before (top curve) and after (bottom curve) applying high pressure. The spectral regions shaded in yellow indicate the location of four peaks characteristic of rhombohedral $\alpha\text{-AgGaO}_2$ 54

Figure 3.4 | Representative Raman spectra of a mixed powder of $\text{Ag}_2\text{O} + \text{Ga}_2\text{O}_3$ with a molar ratio of 1:1 in different pressure and temperature conditions. Characteristic Raman spectrum of rhombohedral $\alpha\text{-AgGaO}_2$ is only present in red spectra. 55

Figure 3.5 The experimental Raman spectrum of DAC-synthesized AgGaO ₂ and calculated frequencies of Raman modes for the three known structures of AgGaO ₂ . (There is a five percent uncertainty due to temperature effects.)	56
Figure 3.6 Electron microscopy characterization of AgGaO ₂ nanocrystals synthesized during high-temperature DAC experiments: (a) SEM and (b-e) TEM images showing the size and morphology of the nanocrystals. (f) EDX-based elemental mapping was confirming the uniformity and perfect overlap of elemental distributions of Ag, Ga, and O (insets).....	59
Figure 3.7 An EDX spectrum from a typical α -AgGaO ₂ crystallite synthesized at high pressure.	60
Figure 3.8 Results of the FullProf-based pattern matching analysis (black curves) of the radial intensity distribution (red curve) of the averaged SAED pattern of the DAC-synthesized AgGaO ₂ for crystal structure models of AgGaO ₂ with (a) R3m (166), (b) P63/mmc (194) and (c) Pna21 (33) space groups. It can be seen that the best fit was obtained for the R3m (166) space group.	60
Figure 3.9 (a) A SAED ring pattern acquired from a typical cluster of a few AgGaO ₂ crystallites. (b) The SAED pattern obtained after averaging the data from about 40 separate clusters. (c) The optimized crystal structure of α -AgGaO ₂ using our DFT method (see text). (d) Experimental intensity profile obtained after rotational averaging of the pattern shown in b (red curve) and diffraction pattern calculated using the pattern matching mode of the FullProf software suite (black curve).....	62
Figure 3.10 TEM-based single crystal study of individual α -AgGaO ₂ crystallite: (a) and (b) low-magnification and high-resolution TEM images; (c) Filtered HRTEM image of	

the area marked using yellow frame in b; (d) corresponding [421] zone axis SAED pattern measured from this crystallite.....	63
Figure 3.11 The calculated electronic energy band structure of α -AgGaO ₂	67
Figure 3.12 A SEM Image of 3D Graphene After Etching Ni Foam with HCl 5M (Right) and Photographs of 3D graphene Samples Before and After Etching Ni foam (right).	68
Figure 3.13 A representative averages of obtained Raman spectra from 3D graphene foam grown at different temperatures.....	69
Figure 3.14 Deconvolution of 3D graphene Raman peaks with a Lorentzian function to find FWHM, positions, and area under the peaks for statistical analysis.	71
Figure 3.15 Raman spectral parameters of synthesized 3D graphene samples at different temperatures.....	72
Figure 3.16 SEM images Show Morphology of a Ni Foam.	73
Figure 3.17 After the Growth, Graphene Coat Has a Morphology Similar to the Morphology of the Substrate (Ni Foam).....	73
Figure 3.18 Photograph of as-prepared 3D graphene foams synthesized under different growth conditions.....	74
Figure 3.19 Scanning Electron Microscopy (SEM) imaging of Ni foam before (top row) and after (bottom row) the graphene growth.	75
Figure 3.20 a, Transmission Electron Microscopy (TEM) image, b, Selected Area Electron Diffraction (SAED) pattern, and c, Electron Energy Loss Spectroscopy (EELS) of pure 3D graphene foam prepared by pyrolysis of Citric Acid as the carbon source.	76

Figure 3.21 a, Transmission Electron Microscopy (TEM) image, b, Selected Area Electron Diffraction (SAED) pattern, and c, Electron Energy Loss Spectroscopy (EELS) of Nitrogen-doped 3D graphene foam prepared by caffeine as the carbon source.....	77
Figure 3.22 TEM Analysis of Top: Pure 3D Graphene (precursor: Citric Acid) and Bottom: In Situ Nitrogen doped 3D Graphene (precursor: Citric Acid + Caffeine)	78
Figure 3.23 Raman spectroscopy of nitrogen-doped 3D graphene foam (three upper spectra) and Raman spectrum of pure 3D graphene foam (red) all grown at 1000 °C.....	79
Figure 3.24 SEM Images of a Nitrogen Doped Sample	79
Figure 3.25 Deconvoluted high-resolution C (1s) X-ray photoelectron spectroscopy (XPS) spectra of Nitrogen-doped 3D graphene foam using Urea as the carbon source. ..	80
Figure 3.26 Deconvoluted high-resolution N (1s) X-ray photoelectron spectroscopy (XPS) spectra of Nitrogen-doped 3D graphene foam prepared by Urea as the carbon source.....	81
Figure 3.27 nitrogen-bonding configurations in the nitrogen-doped carbon	81
Figure 3.28 Catalytic activity of Nickel foam, Three-dimensional graphene network on nickel foam (Ni-G), Carbon doped with Nitrogen (polyaniline) with core-shell of 3D graphene (Ni-PG), and Silver film (Ag Film).....	82
Figure 3.29 Ruby fluorescence spectra at different gas membrane pressures (measured by gas controller unit). These pressures correspond to the actual pressures inside the DAC.....	84
Figure 3.30 The ruby fluorescence R2 line peak position as a function of pressure inside the gas membrane (measured by gas controller unit).	85

Figure 3.31 Pressure inside the diamond anvil cell as a function of gas membrane pressure.	86
Figure 3.32 Raman spectra of a few-layer black phosphorus (sample no. 1) under pressure range of 0 GPa (bottom spectrum) to 13.4 GPa (top spectrum) with vertical displacements for clarity.	87
Figure 3.33 Raman spectra of a few-layer black phosphorus under pressure range of 0 GPa (bottom spectrum) to 12.56 GPa (top spectrum) with vertical displacements for clarity.	88
Figure 3.34 Raman shift of three prominent peaks of phosphorene as a function of pressure.	94
Figure 3.35 Raman A_{1g} peak position of phosphorene vs. pressure (red) and its linear fit (black)	95
Figure 3.36 Raman shift of A_{2g} mode of phosphorene vs. pressure (blue) and its linear fit (black)	95
Figure 3.37 Raman shift of B_{2g} mode of phosphorene vs. pressure (green) and its linear fit (black).....	96
Figure 3.38 Raman shift of a full pressure cycle of phosphorene from normal pressure (bottom spectrum) to 13 GPa (indicated by the arrow) and returning to ambient pressure (upper one).	97
Figure 3.39 Normalized Raman spectra of phosphorene vs. pressure	98
Figure 3.40 Full-Width Half Maximum (FWHM) of A_{1g} Raman mode as a function of the pressure.	98

Figure 3.41 | Full-Width Half Maximum (FWHM) of A_{2g} Raman mode as a function of the pressure. 99

Figure 3.42 | Full-Width Half Maximum (FWHM) of B_{2g} Raman mode as a function of the pressure. 99

CHAPTER 1: BACKGROUND

1.1 High-Pressure Physics and Chemistry

History of high pressure is about understanding the behavior of matter under extreme conditions and it is extended from planetary science to nuclear explosion and semiconductor physics to crystallography [1]. Pressure is an important thermodynamic variable, which has been less explored comparing to temperature and other thermodynamic variables. High pressure can tremendously influence the physical and chemical properties of materials. Pressure is a valuable tool for synthesizing new phases of material with enhanced properties, and for investigating the available phases.

Under extreme conditions interatomic distances, electron configuration, density, and free energy of materials can be modified [2]. Pressure variation range in nature extending over 60 orders of magnitude [3,4] and the range of attainable static pressures with current equipment available in research laboratory exceeding more than 10 orders of magnitude [5]. In this regards pressure is unique among physical variables. In the universe pressure is ranging from the $\sim 10^{-27}$ Pa of hydrogen gas in the intergalactic spaces to the $\sim 10^{30}$ Pa in center of neutron star and its available domain in laboratory is from $\sim 10^{-12}$ to $\sim 10^{14}$ Pa.[6-9]

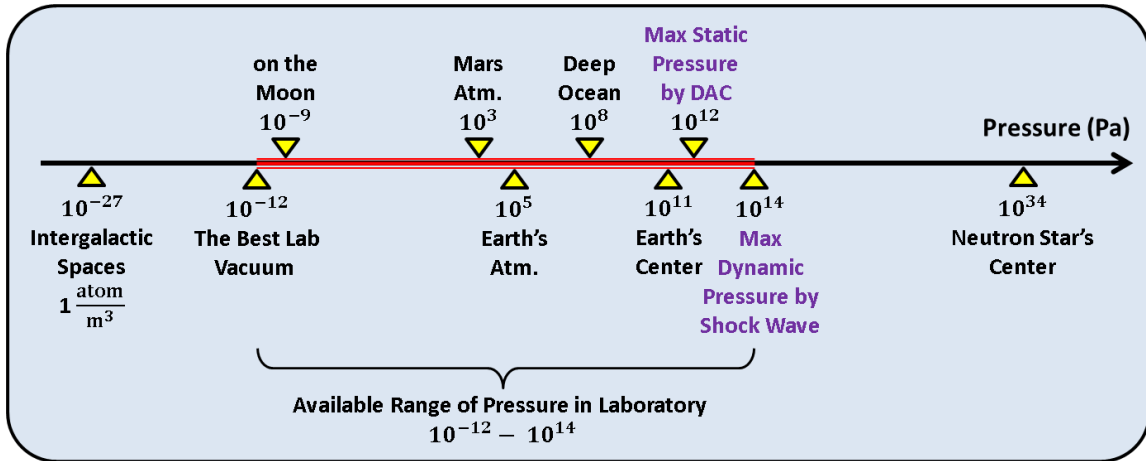


Figure 1.1 | Range of pressure in the universe and obtainable range in available laboratory equipment [3,4,6-12].

Since pressure significantly influences the reaction equilibrium [13] it can be utilized to produce metastable materials. Many thermodynamically metastable materials that synthesized under high pressure can remain kinetically stable at normal pressure for a long time [14]. High pressure can facilitate synthesis of metastable materials by significantly reducing the reaction temperature. High-pressure synthesis of metastable materials are important because many of novel and valuable materials are metastable. Under high pressure, volume changes considerably therefore properties can be explored and tuned with respect to interatomic distances. In contrast to high pressure tuning, chemical modification and modification with temperature have many disadvantages such as imposing melting, boiling, phase separation, disorder, and substantial variations in entropy. The data obtained during high pressure probing and tuning can be used to understand properties of existing materials and designing novel materials for the first time.

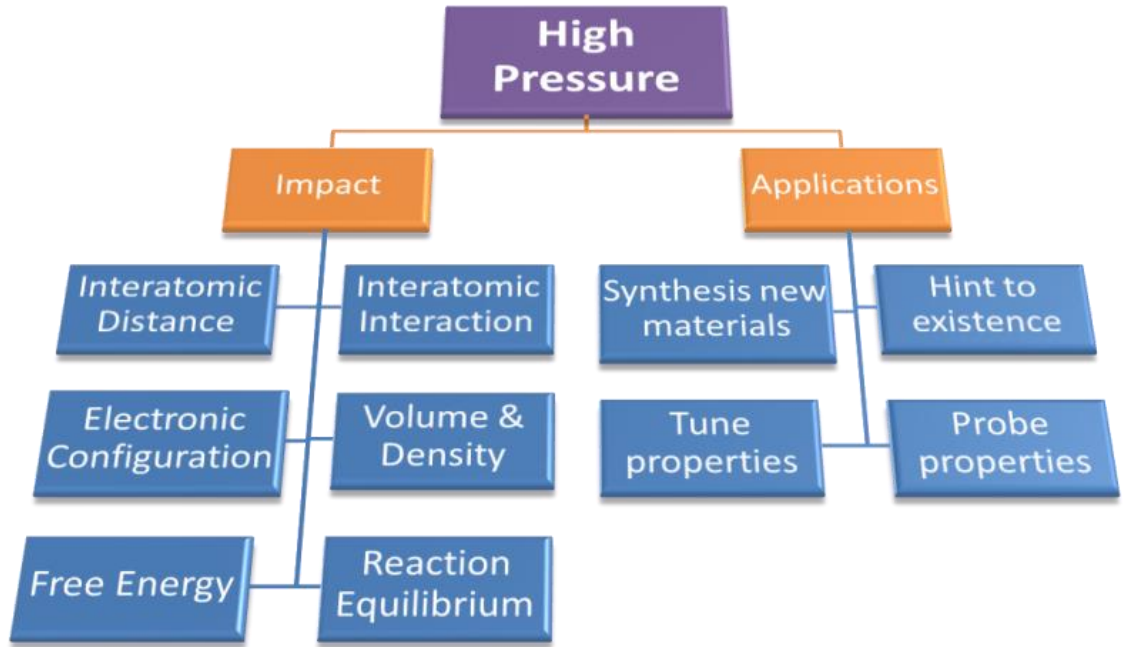


Figure 1.2 | High pressure impact on materials and its applications in materials science.

Fundamental thermodynamic variables (pressure, temperature, and concentration) control the chemical reactions, the equilibrium, and rate of materials transformations. However, in solid state of materials, only temperature and concentration influence on the chemical reaction [15] and equilibrium have been investigated thoroughly and the effect of high pressure is remained less explored. One of the reasons behind the underutilizing the high pressure in materials science in comparison with other thermodynamics parameters is the fact that the equipment of high pressure experiment is not routinely available in physics and chemistry laboratory and they are limited to specialized laboratory. The other reason is the very small volume of the samples in high pressure experiment as it is not possible to reach very high pressure in large volume. Recently, the number of high pressure research works has growth explosively and the study of materials under extreme conditions has attracted substantial attentions among scientist [16]. The main reason for

this rapid increase is the latest advancement in both experimental and theoretical capabilities that have simplified the high-pressure experiments.

The small volume of the sample and its chamber opening in high-pressure experiments make the signal to noise ratio considerably small and consequently severely hampered an effective in situ measurement. However, development in high pressure instrumentation help researcher to overcome the limitations that arise from the sample size [17]. In last few years, advances in high pressure equipment specially improvement in design of diamond anvil cell (DAC) has led to major breakthrough in application of high pressure in materials science [1]. Nowadays, using a diamond Anvil Cell (DAC), one can achieve to the pressure over 700 GPa [11] and also using laser heating techniques to the temperature up to ~ 6000 °C [18]. Recent developments in high-pressure equipment have created new opportunities for investigating the behavior of materials at high-pressures. Diamond anvils in DAC is transparent to wide range of electromagnetic radiation and this property of diamond along with its hardness make diamond anvil cell (DAC) extremely powerful tool for various in situ high-pressure measurements. Currently, using DAC a broad range of probing techniques can be performed from X-ray and neutron diffraction to spectroscopic techniques such as Raman, Fourier transform infrared (FTIR) and photoluminescence (PL).

Advances in theoretical and computational calculations also attributed to the rapid growth in high pressure research works. On the one hand, developments in calculation algorithm [19,20] and on the other hand sharp increases of computers power resulted in reliable theoretical predictions of phase stability [17] and also calculation of structural, vibrational and electronic properties of materials accurately. This theoretical data can

provide research direction for high pressure experiments and also help to interpret the experimental results [1,21].

The most frequent computational modelling method in high pressure research is density functional theory (DFT) [22,23] with local-density approximations (LDA) to the exchange–correlation (XC) energy functional [24-27]. In first principles theoretical calculation approaches like DFT pressure can be considered as a probe to study variations in properties of condensed matter as a function of interatomic distances.

Therefore influence of pressure compared to temperature can be incorporated into ab initio modelling easier which need sampling of several configurations. This makes pressure very attractive thermodynamic parameter for first principles calculations [1].

High pressure and its severe impact on interatomic distances and consequently overlap of the electron clouds increase the energy of the electrons and put the system in very unstable state. Therefore, the system tries to recover and minimize the free energy which leads to several phenomena, namely, amorphization, condensation, polymerization, direct to indirect band gap transition, dissociation, ionization, semiconductors to superconductors transition, ferromagnetic to paramagnetic transition, crystal phase transformation, and metallization [28,29].

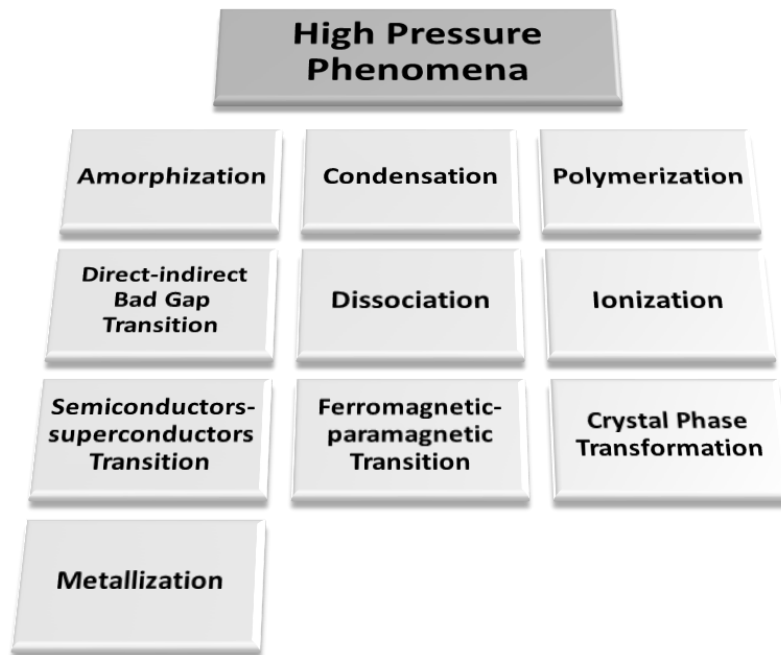


Figure 1.3 | Phenomena under High Pressure [30].

1.2 The Nobel Prizes for High-Pressure Research

Three nobel prizes in physics and chemistry for high pressure related research are another indication of the importance of high pressure. In 1918, a German chemist, Fritz Haber (1868 – 1934), was received the Nobel Prize for invention of a high pressure method to synthesize ammonia [31]. In 1931, Carl Bosch (1874 – 1940) and Friedrich Karl Rudolf Bergius (1884 – 1949), who were both German chemists, were received the Nobel Prize for the invention and development of chemical high-pressure methods [32]. In 1946, Percy Williams Bridgman (1882 – 1961), an American physicist won the physics Nobel Prize for his high pressure research [33].

1.3 Kinetics, Thermodynamics and Metastability

In any chemical reaction or phase transformation one can think of atleast three energy state for the system during the process as it shown in Figure 1.4.

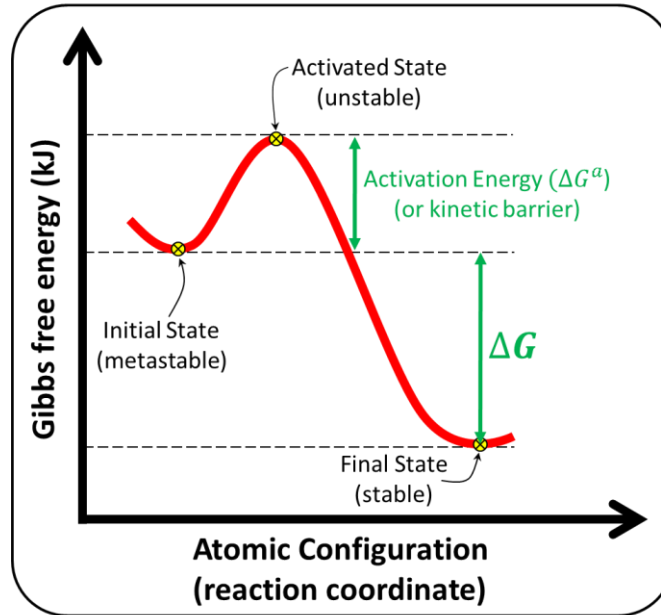


Figure 1.4 | Energy Profile Diagram of a Phase Transformation.

Activation energy (kinetic barriers) determines the transformation rate of a process from initial state to the final [34] equilibrium. When the rate of transformation is very slow due to the kinetic barrier and there is an alternative phase (metastable) with lower energy barrier the crystal may transform to the metastable phase instead of the stable one [14]. Many metastable phases have such a long lifetime that experimentally they are not distinguishable with equilibrium phases. Interestingly, metastable phases are common among materials with covalent bonds therefore many semiconductor structures are metastable. Diamond is an example of metastable structure with long lifetime that if heated at high temperature transforms to more stable graphite phase.

1.4 Semiconductors under High Pressure

Semiconductors are significantly important materials with extremely wide range of applications from electronic and information technology to energy harvesting and energy

storage[17]. Majority of semiconductors are covalently bonded materials and consequently the metastable phases are very common among semiconductors. Furthermore, semiconductor materials naturally tend to transform progressively to a denser structures through a chain of high pressure structural transitions. As a result of the metastability and typical tendency toward high-pressure phase transitions, studies of semiconductors under high pressure become considerably important. High pressure can severely affect the interatomic distances and consequently all the interatomic interactions which control materials properties. In other words high pressure impose such a drastic changes to semiconductor physical properties that is not possible to achieve by temperature variation alone. Band gap closure and metalization or indirect to direct band gap transition are exaples of high pressure influence on semiconductors. Typically, electron bands get broader under high pressure and this leads to a band gap reduction. Moreover, band gap closure and metallization commonly occur in the first step of phase transitions under high pressure.

Another important advantage of high pressure probing of semiconductors is the possibility of studying the defect nature in these materials. This is possible because the high pressure can locally change neighboring defect structure and move its correlated electronic states. However, the amount of pressure needed to change the local structure around a crystal defects is relatively low compare to pressure needed for phase transitions.

1.5 Conditions for Stable Phases

In a structure transition process Gibbs free energy (G) of the system determines the stability of the final phase. In other words during the tarnsition process Gibbs free enrgy

of the system must be minimized to reach the equilibrium phase at specific temperature and pressure. For Gibbs free energy we have:

$$G(P, T) = U + PV - TS \quad (1)$$

where U is the internal energy (joule), P is pressure (pascal), V is the volume (m^3), T is the temperature (kelvin) and S is the entropy (joule per kelvin).

In a high pressure experiments we are dealing with a system that P and T are external parameters, and other variables in Gibbs free energy function (i.e. U , V , and S) are free to adjust in a way to minimize Gibbs free energy. That is to say we work with statistical constant pressure ensemble.

In equation (1) it is evident that by increasing the pressure, phases with smaller volume are more favorable. Furthermore, temperature and entropy are linked together according to the equation and we know configurational entropy are same for all solids crystals. This makes temperature less effective in solids structural transformation compare to pressure.

In high pressure phase transformation process if the pressure is hydrostatic there is another condition that must be satisfied for the stable structures. That is the stress tensor σ_{ij} must be in diagonal form:

$$\sigma_{ij} = \frac{d^2 U}{d\varepsilon_i d\varepsilon_j} = \begin{pmatrix} P & 0 & 0 \\ 0 & P & 0 \\ 0 & 0 & P \end{pmatrix} \quad (2)$$

In this equation ε_i and P are strain in i direction external pressure, respectively. If above two conditions are satisfied for a specific crystal structure then it can be considered as the stable phase after the transformation process [1].

Table 1.1 | In-situ High Pressure Probes with references.

In Situ High Pressure Measurements			
X-ray Diffraction (XRD)	[35-38]	UV - Vis Spectroscopy	[39]
Single-Crystal X-Ray Diffraction	[38,40,41]	Resistivity Measurement	[42-44]
X-ray Absorption Spectroscopy (XAS)	[38,45,46]	Raman Spectroscopy	[47-50]
Extended X-ray Absorption Fine Structure (EXAFS)	[34]	Neutron Diffraction	[51]
X-ray Absorption Near Edge Structure (XANES)	[45]	Mössbauer Spectroscopy	[52,53]
X-ray Fluorescence (XRF)	[45]	Impedance Measurements	[54]
X-ray Magnetic Circular Dichroism (XMCD)	[46]	Hall Effect Measurement	[55]
Hall Effect Measurement	[55]	Infrared Spectroscopy	[38,48,50]
Brillouin Spectroscopy	[56,57]	FTIR Spectroscopy	[48,58]
Photoluminescence Spectroscopy	[59,60]	X-ray Raman Spectroscopy	[61]
Nuclear Resonant Inelastic X-Ray Scattering	[61,62]	Ultrasonic Interferometry	[63,64]
Resonant Inelastic X-Ray Scattering Spectroscopy	[61]	Optical Interferometry	[65]
Electronic Inelastic X-Ray Scattering Spectroscopy	[61]		

1.6 Rhombohedral α -AgGaO₂ (Semiconductor with ABC₂ Form)

As mentioned earlier, in materials science and solid-state physics, high-pressure techniques are employed for tuning a variety of material properties such as magnetic ordering, electronic and heat transport and optical response. Moreover, they are being used in synthesizing non-equilibrium phases or novel compounds [2,66-68]. Applying

high-pressure leads to shrinkage of the inter-atomic distances and enhancing the reactivity of materials [30].

In particular, high-pressure techniques are useful in cases of decomposition of one of the precursors under normal pressure (i.e., at 1 atm.) and at temperatures below the reaction temperatures. Applying high-pressure increases the decomposition temperature and consequently, stabilizes the precursor. This method has been reported for stabilizing HgO [69], MnO₂ [70] and PbO₂ [71].

In this work, we synthesized α -AgGaO₂ [72] by mixing Ag₂O and Ga₂O₃ powders under high-pressure. Since Ag₂O is instable under the atmospheric pressure and undergoes decomposition at a temperature of about 300 °C [73-76], it is challenging to synthesize AgGaO₂ in a single step using the common open-system methods. Thus, producing silver delafossite has been done using closed-system techniques such as cation exchange (metathetical) [77], hydrothermal reactions [78], oxidizing flux [79] and ultrasound assisted reactions [80]. However, each of these methods imposes different limitations such as producing undesired by-products. Also, they are time consuming and require multiple steps [79,81,82].

1.7 Three-Dimensional (3D) Graphene Architecture

For years, graphene materials family has been studied intensively and remains in the center of researchers' attention in the field of materials science owing to its astonishing properties. Combinations of the tremendously large surface area, elegant electrical and thermal conductivity, superior chemical stability, and extreme mechanical strength make graphene an essential component for fabricating functional materials for a broad range of applications. However, practical limitations such as the difficulty of mass

production of high-quality samples render a barrier to extensive implementation of graphene in practical devices. For example, during the processing of graphene into an actual device, the strong π - π interaction between graphene sheets cause the isolated graphene flakes to restack to form graphite-like powders which can substantially reduce the specific surface area and thereby resulting in inefficient utilization of the graphene layers [83-89].

Recently, three-dimensional structures of graphene have attracted tremendous attentions as an effective way to utilize the distinctive inherent properties of graphene sheets in practical applications. Three-dimensional graphene-based materials offer an easy and versatile platform for functionalization and integration into devices. Furthermore, the interlocking of graphene sheets into 3D structures solve the restacking issue and make 3D graphene-based materials more compatible with conventional material processing. As a result, 3D graphene materials and their derivatives triggered extensive studies for numerous potential applications in energy, electrochemistry, bioelectrochemistry and pollution management [90-97].

Particularly, in the field of energy, the superior performance of both electric double-layer capacitors and pseudocapacitors can be achieved by functionalization of 3D graphene foam due to its unique structural properties. 3D Graphene foam structure enhances the access of electrolyte with its surfaces while providing electrically conductive pathways for the functional materials. Generally, in electrode systems, the porous structures of 3D graphene facilitate incorporation of active materials to form 3D graphene-based composites. Therefore, the performance of the electrode systems is enhanced by the combination of 3D graphene structural features and electrochemical

activity of incorporated materials. Moreover, 3D graphene-based materials have been identified as an ideal candidate for environmental applications. The exceptional large surface area along with well-defined porous arrangement allow 3D structures of graphene to capture molecules of contaminations efficiently [98-101]. Also, three-dimensional graphene-based materials can be recycled easily. Removal of oils, organic dyes and solvents, heavy metals, and gas pollutants are few examples of environmental applications for 3D graphene-based materials [102-104].

1.8 Few-Layer Black Phosphorus (Phosphorene)

Since 2004 that graphene was discovered [105], there has been a search for new two-dimensional (2D) materials. Phosphorene is one of the newly discovered 2D materials with most interesting properties and multiple possible applications [106]. A single atomic layer of black phosphorus (BP) is called phosphorene. Two-dimensional materials are composed of a single-atom-thick layer and can be categorized into diverse groups [107-110].

Despite the superior properties of Graphene such as high carrier mobility, ultrahigh surface area, excellent thermal conductivity, and quantum confinement effect [111] the lack of band gap limits its electronic applications. However, BP has a highly tunable thickness-dependent band gap. It can be changed with functionalization, doping and the number of layers from ~ 1.5 eV (monolayer) to 0.3 eV (bulk BP) [112]. Other significant properties of BP include high carrier mobility, and strong in-plane anisotropy, particularly the anisotropy of electric conductance [113]. Moreover, the carrier mobility and on/off ratio are layer-dependent as well [114].

BP was first discovered by Bridgman more than a century ago [115]. Similar to graphite, it is a van der Waals material, and is comprised of vertically stacked 2D sheets. Unlike graphite, the in-plane bonding in BP stems from sp^3 hybridization which prevents phosphorene from forming atomically flat sheets [116]. They arrange a puckered honeycomb-structured layers [117]. The layers are attached together by weak van der Waals forces[118]. The electronic band gap of bulk BP is 0.3 eV, which is much smaller than the predicted 1.5 eV value of phosphorene.

CHAPTER 2: EXPERIMENTAL METHODS

2.1 High-Pressure Equipment

Diamond anvil cell (DAC) is a small device to generate extreme thermodynamic conditions i.e. high pressure and high temperature. DAC consists of two opposing diamond anvils with small flat culet. DAC compresses small samples between diamond culets and can generate very high pressure of above 100 GPa easily [11]. The current record of pressure with DAC is about 1 TPa [119]. Moreover, samples in DAC can reach to the temperature as high as 5000 C. The first diamond anvil cell was made by Charlie Weir in 1958 in the NBS laboratory[120].

2.2 Diamond Anvil Cell (DAC)

Diamond anvil cell (DAC) was developed by Weir et al. and Van Valkenberg [120] for generating high-pressure conditions. This device followed the pioneering work in high pressure by Percy W. Bridgman [33]. They replaced the tungsten carbide in traditional anvils with a diamond, which is significantly smaller and harder. Moreover, the optical properties of diamond allow in-situ spectroscopy at high-pressure conditions.

The DAC is composed of two opposed diamond anvils (Figure 2.1). Due to the smaller surface area at the tip of the diamond, the pressure is considerably higher in this region comparing to the back of the diamond (referred as table). A metallic gasket is placed between the flattened tips (called culet) to prevent them from touching. The gasket is drilled at the center to create a sample chamber where a pressure transmitting medium

surrounds the sample. Applying a small force to the diamond tables will apply a significant pressure to the sample. The pressure is measured using a small amount of ruby between the culets. Using DAC, one can achieve pressures in the gigapascal range [11,119].

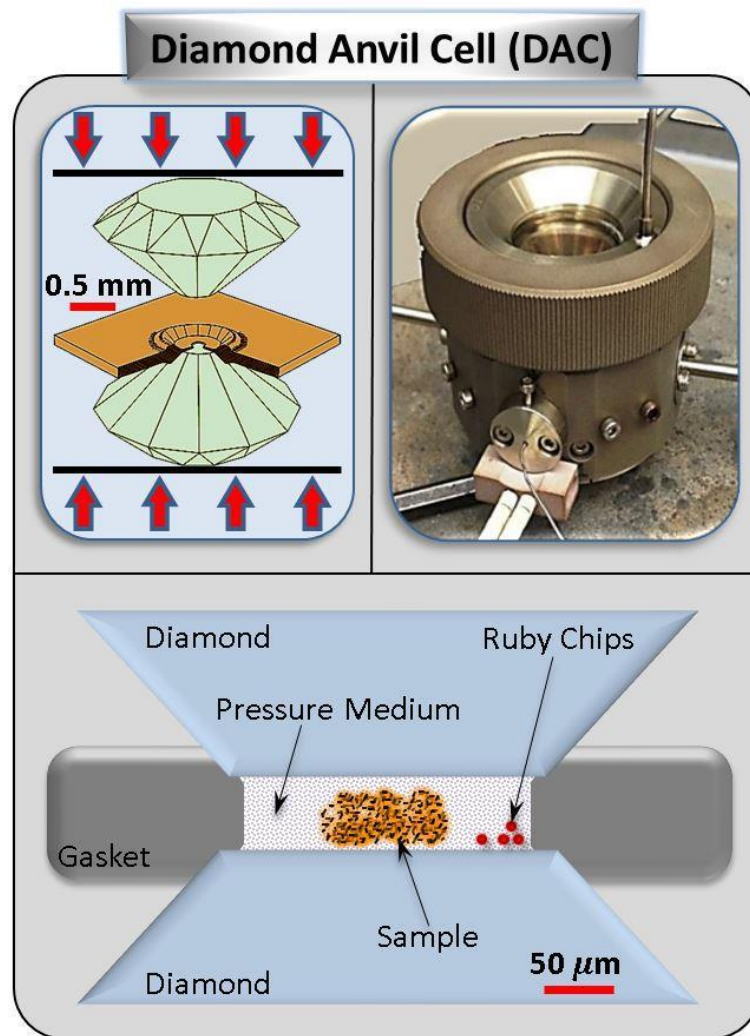


Figure 2.1 | Schematics of the diamond anvil cell (DAC) and a photograph of our gas membrane driven DAC. Typical DAC is composed of two opposed diamond anvils with a metallic gasket in between providing a small chamber for the sample.

The diamonds are attached to the backing plates of the DAC. The pressure can be increased by applying a force on the membrane or by twisting the screws so that the two

parts of DAC approach further. Since there are four screws, one must make sure to turn all the screws in the same manner. This can be done by keeping the screws at equal height. A caliper can be used to measure the height. It is more reliable to raise the pressure by applying a force on the membrane as the force transforms uniaxially through the membrane.

2.2.1 Diamond Anvils

The geometry, purity, and color of the diamond play a deterministic role in the outcome of high-pressure experiments. Hence, it is important to choose the right diamond. This can be done by using the classification of the '4cs' of diamond: carat, clarity, cut and color [121]. A carat is a unit of mass, equal to 200 mg for measuring gemstones and pearls.

The clarity represents the quality of diamond in the sense of impurities. The level of clarity is determined based on the appearance of the diamond under 10X magnification.

The surface and internal defects are called blemishes and inclusions respectively.

Inclusions can lead to cracks under high pressures. Moreover, for spectroscopic applications, high clarity diamonds are desired as the defects can shift optical paths causing a drift in the experimental results. A diamond of grade F (Flawless) shows no blemishes or inclusions under 10X magnification and is the most suitable choice for spectroscopic measurements.

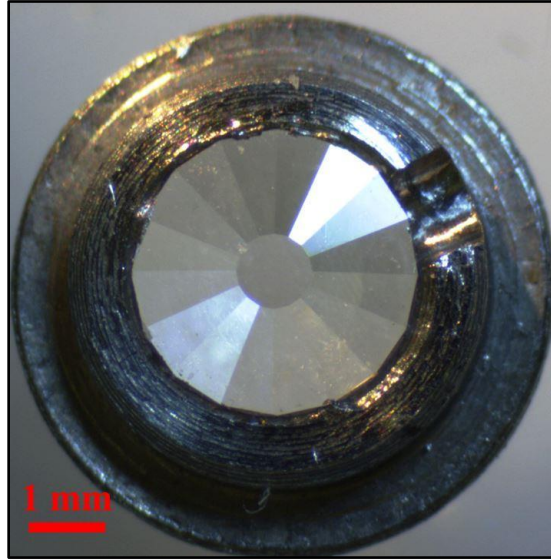


Figure 2.2 | Magnified Photograph of a Diamond Anvil under Optical Microscope.

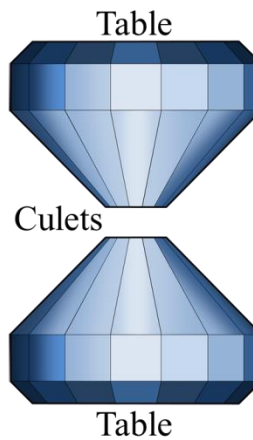


Figure 2.3 | Schematic of two diamond anvils with the standard design cut (Culet and Table of the Anvils is indicated).

The cut and design of the diamond anvil plays a major role in the high-pressure experiments, as the size of the diamond culet is the major factor to find out the maximum attainable pressure. A well-known design is the modified brilliant cut with a smaller distance between the table and the girdle (Figure 2.4). This allows a larger table resulting to a larger area for applying the force [121].

Another typical design of diamond anvil is the Boehler-Almax cut (Figure 2.4). Boehler-Almax cut provides a larger aperture for in-situ X-ray diffraction experiments.

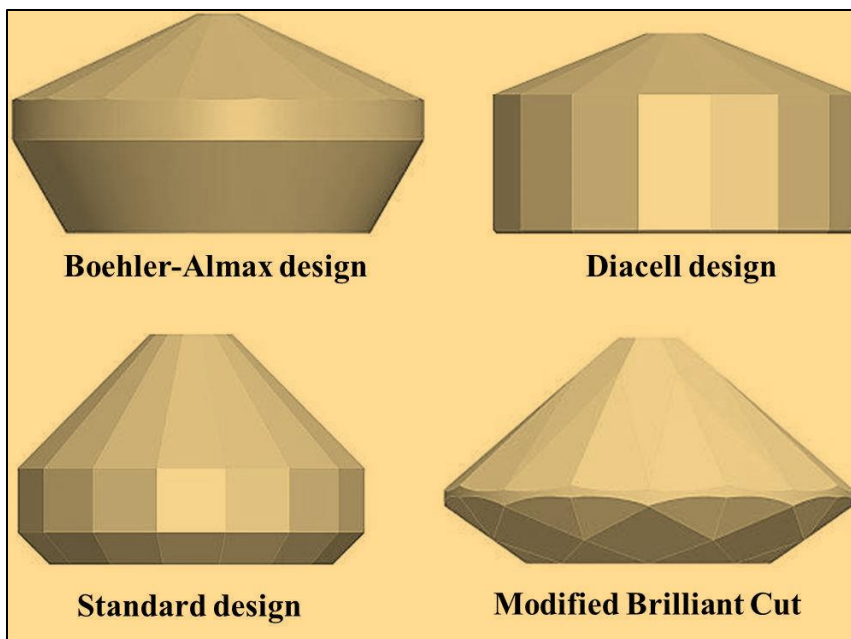


Figure 2.4 | Few Different Diamond Anvil Designs and Cuts that is commercially available from Almax easyLab Inc).

The diamond color scale is set by Gemological Institute of America (GIA). The color of diamond is defined by GIA as the lack of color. They provide a D to Z color-grading scale based on the degree of colorlessness where D and Z represent “completely colorless” and “pale yellow/brown” respectively. The diamond color is specifically important in the spectroscopic measurements as the fluorescence from the diamond can raise the background signal. Raman spectroscopy can be used to examine the fluorescence level of the diamond.

The DAC is composed of several parts including but not limited to diamond anvils, metal gasket, and backing plates. A crucial step in DAC experiment is putting all the

components together. For instance, it is important to ensure that diamond anvils are well aligned before loading the sample or applying force to the DAC.

2.2.2 Backing Plates

Typically, backing plates (diamond anvil seats) are made of tungsten carbide and hold the diamond anvils in place. Depending on the experiment temperature, different materials can be used to glue the diamond anvils onto the backing plates. Hysol 9437 and STYCAST epoxies are used for high- and low-temperature experiments respectively. Before attaching, the anvils and backing plates must be cleaned carefully as the dust can initiate an asymmetry and consequently a crack in the diamonds at high pressures. A mounting device can be used to hold the anvils and plates in the right position close to each other while applying the glue.

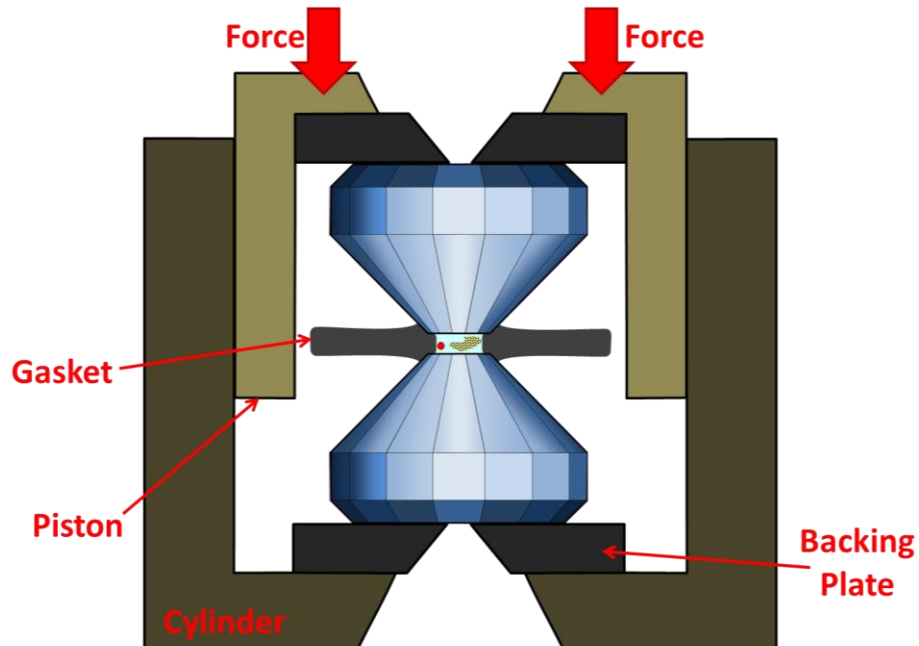


Figure 2.5 | Increasing the pressure inside the sample chamber by applying a force onto the pistons.

2.2.3 The Alignment of the diamond Anvils and preparing the sample chamber

Other than aligning the anvils with backing plates, the two diamonds must be lined up so that their culets are parallel with each other.

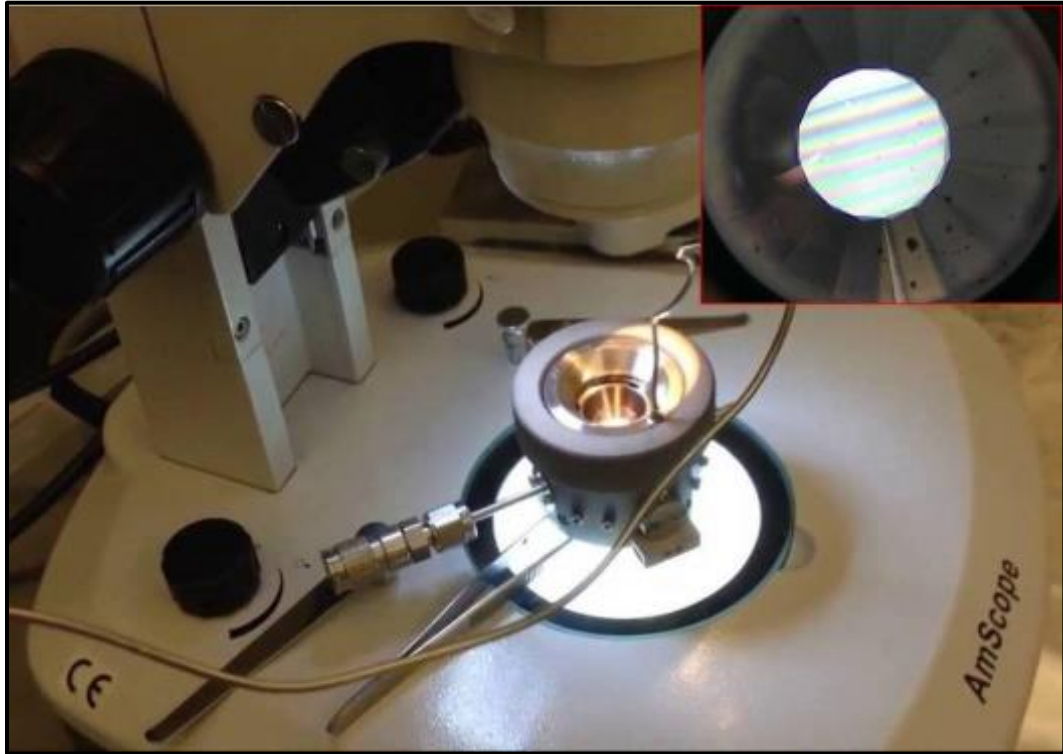


Figure 2.6 | Top View through Diamonds with Optical Microscope Showing the Misalignment of Anvils.

The alignment process should be done under optical microscope. Top and lateral view of diamond anvils when they are close reveal any misalignment. Figures 2.6 and 2.7 show the top and lateral views of anvils under the microscope. In top view (Figure 2.6) under the microscope if the anvils are not parallel the newton rings reveals the misalignment. Moreover, with high magnification optical microscope it is necessary to check all lateral direction to make sure that diamond anvils are aligned perfectly. Any small asymmetry in the system under very high-pressure can resulted in breaking the diamond anvils.

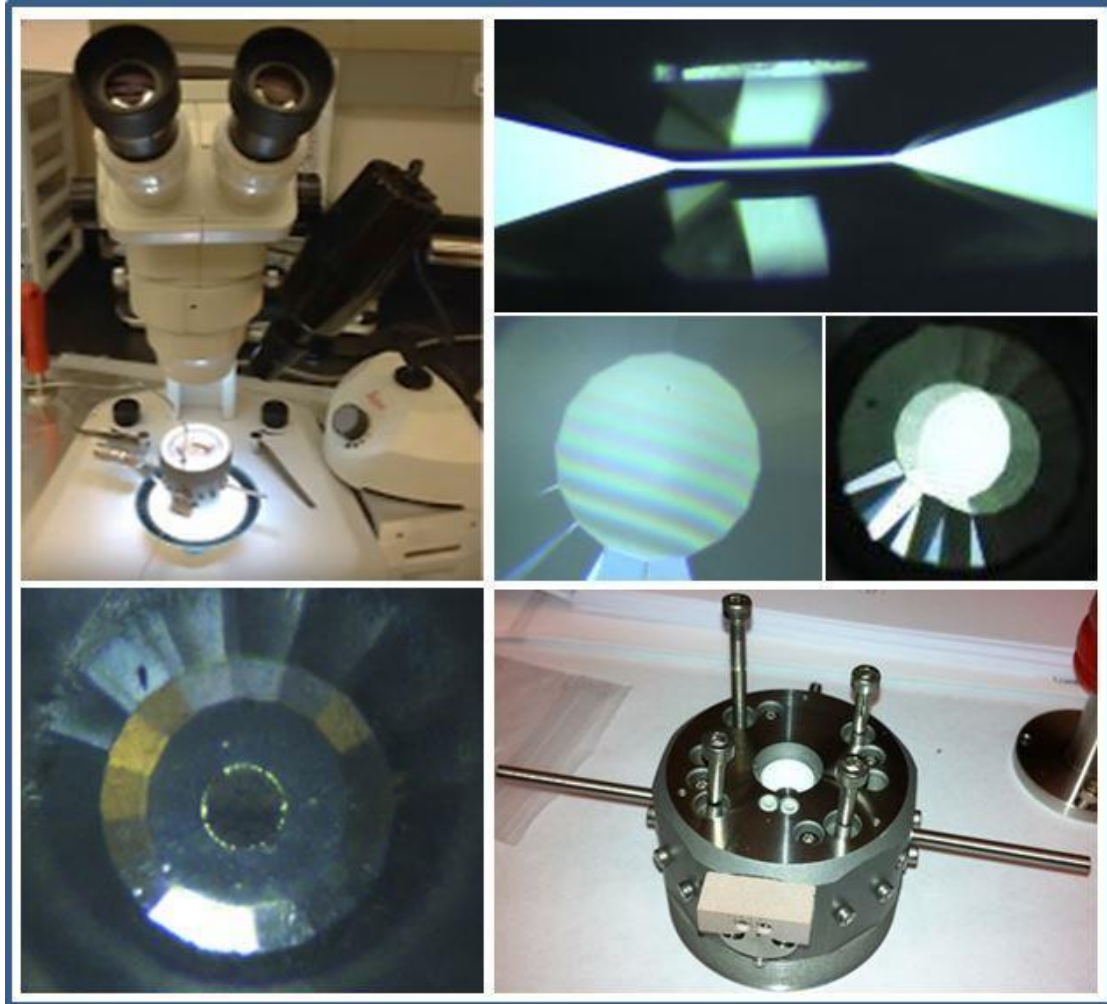


Figure 2.7 | Alignment of the diamond anvils and Loading Samples (Powder) in Gasket Hole (Sample Chamber) under the Microscope

A metallic gasket with a hole at its center is used as a sample chamber between the anvils. Before drilling the hole, the gasket must be preindented between the diamond anvils inside the DAC. Then the hole is drilled at the center of the indentation. The size of the indentation depends on the experiment and the range of desired pressure. A larger one is suitable to achieve higher pressures, and a thinner one is preferred to reach higher temperatures.

2.2.4 Drilling Small Hole at Center of the Metallic Gasket

To create symmetric holes at the center of the gasket, which served as the sample chamber a Micro Electric Discharge Machining (EDM) system from Hylozoic Products was utilized. Since the holes could be in the range of $\sim 200\ \mu\text{m}$, the drilling should be done under the microscope. In this work, we used inconel or stainless steel gasket for the high-pressure experiments. The EDM system was used in combination with an optical zoom microscope (Figure 2.9) to find the center of the indentation accurately. EDM uses electrical discharges to melt the gasket to make the hole.

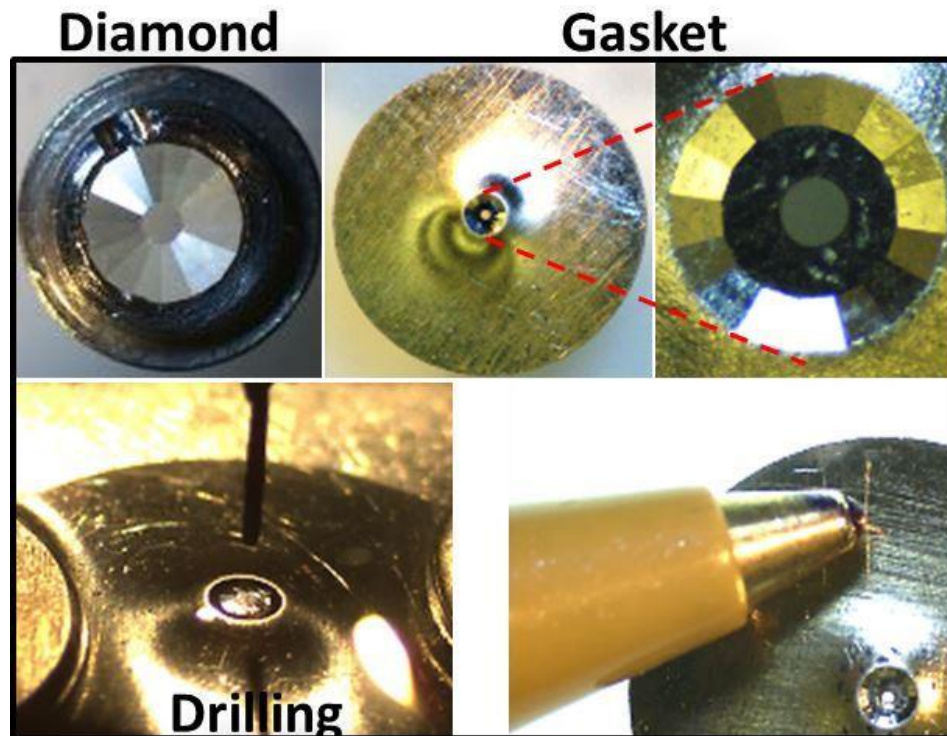


Figure 2.8| Small Hole at the Center of the Metallic Gasket as a Sample Chamber.



Figure 2.9 | The Micro EDM System and Optical Zoom Microscope.

2.2.5 Loading of the Sample into the Gasket Hole

At this stage, the sample chamber is ready to be loaded. The sample should fill about a half of the gasket hole, and it should not be in touch with the gasket if hydrostaticity is important. A typical volume range of the sample is about 50 to 100 μm^3 . In the case of powdered samples, further grinding is done using diamond anvils or tungsten carbide cubes. Then the sample can be transferred to the chamber using a needle tip in μm range. This process can be done inside a glovebox to avoid sample contamination [121].

2.2.6 Pressure Transmitting Medium

The sample must be surrounded with a pressure-transmitting medium (PTM) for hydrostatic pressure. A suitable PTM should have a simple crystal structure. Moreover, it must be chemically inert, highly compressible and very soft. Noble gasses like helium, neon, and argon are among the mediums that can be used as a PTM. Choice of the right

PTM depends on the experiment parameters. For instance, Helium (He) is employed in studies of the equation of states and Alkali halides like sodium chloride (NaCl) and potassium bromide (KBr) are mostly applied to experiments that involve melting as they feature a high melting point. It is extremely important for the PTM to have a high hydrostatic limit. Otherwise, it can be contributed to the phase transition of the sample, which is not desired and may cause wrong conclusions. It is more straightforward to use a liquid or solid PTM rather than a gaseous one as using gas as the PTM is involved in a difficult gas loading procedure [122-125].

2.2.7 Heating Techniques

There are several methods for increasing the temperature inside a DAC, laser heating, internal resistive heating and using external furnace are typical DAC heating methods. In the case of laser heating method a laser with long wavelength i.e. IR or near IR lasers (e.g. CO₂ and Nd:YAG) is used to increase the sample absorption and generate high temperature up to 7000 °C. However, in the case of the resistive heater, either an external or an internal heater can be utilized to reach up to 1000 °C.

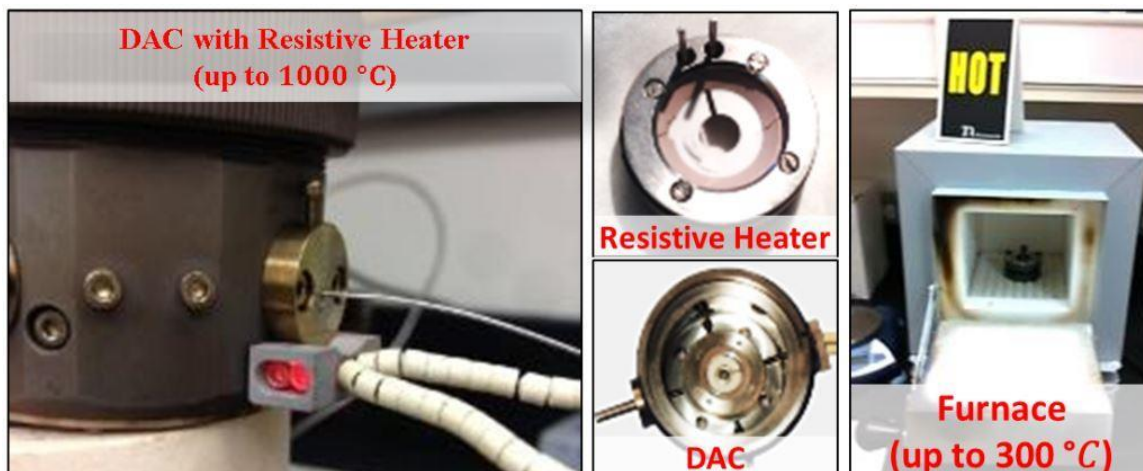


Figure 2.10 | Internal Resistive Heater DAC System and the External Furnace that we used for temperature below 300 °C.

At Conn Center we use the Diacell HeliosDAC which is a membrane driven DAC that uses an internal resistive heater for generating temperatures up to 1000 °C. A reducing gas mixture (2 % H₂ + 98 % Ar) should flow through the DAC to prevent oxidation of the cell components.



Figure 2.11 | Compact resistive heater (80 W), heater components, and DC power supply.



Figure 2.12 | Burned heater components due to excess of current into the metal resistor.

Traditionally resistive heating experiments used wires wrapped around the gasket or backing plates, through which a current is passed to generate heat. The DAC itself can become quite hot during the heating process, which can be resulted in oxidation of the cell body. The membrane drive allows us to make pressure adjustments without disturbing the cell during in situ measurement.

2.2.8 Pressure Measurement in the DAC

XRD of a material with known equation of state and fluorescence spectroscopy of ruby are two main methods of pressure measurement inside the DAC. Nowadays, R2 line shift in Ruby PL is the most popular technique for measuring high pressures in DAC studies. Among the tested material, ruby has shown the most promising results. Ruby's luminescence had been vastly investigated in the fifties and sixties. The energy levels were calculated as a function of pressure. The two peaks in Figure 2.13 represent the energy levels of Cr in Ruby. They increase linearly with raising the pressure [126-129].

Over the several decades, different scientist groups have offered various calibrations for the ruby scale [128,130-132]. Following calibration of ruby PL against the pressure was calculated by Syassen [130]:

$$P = 1870 \eta [1 + 5.9 \eta]$$

$$\eta = \frac{\lambda}{\lambda_0} - 1$$

Where P is the pressure, λ and λ_0 are the wavelengths of the R1 line of ruby PL peak at the pressure P, and the ambient pressure respectively.

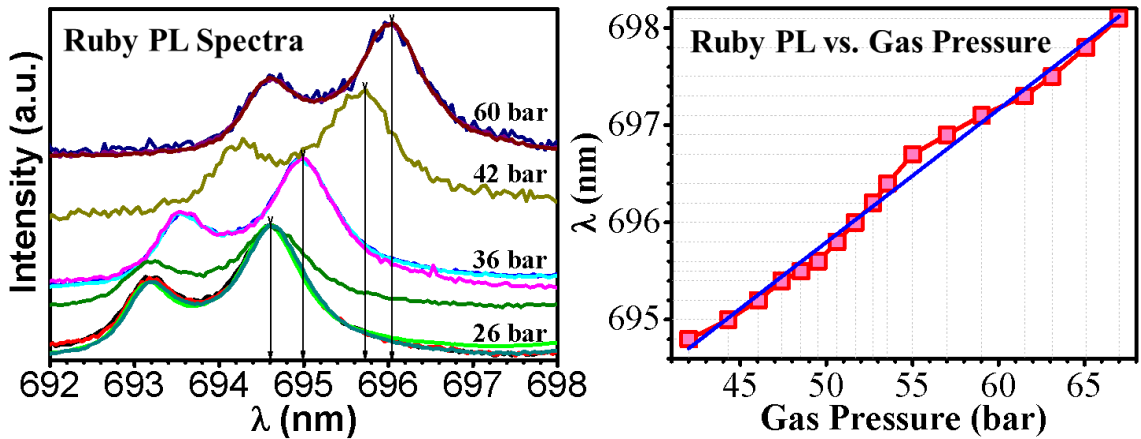


Figure 2.13 | Right: Ruby Photoluminescence Spectrum undergo a Red-Shift by Increasing the Pressure. Right: The gas pressure in the membrane of the DAC can be calibrated to be a scale of the sample pressure.

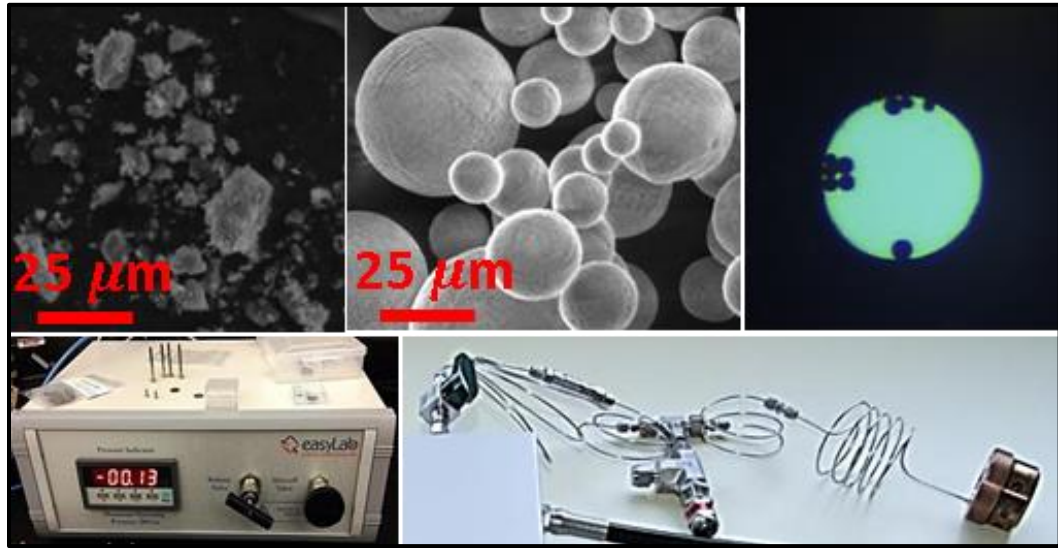


Figure 2.14 | Top Row: SEM Images of Two different Ruby Chips and Photograph of Ruby Chips inside Gasket Hole. Bottom Row: The Gas Controller and Gas Membrane along with the DAC.

2.3 Characterization Equipment

Various material characterization methods have been used in the presented work in this thesis. These techniques include Raman spectroscopy, Photoluminescence spectroscopy, UV/Vis/NIR absorption, X-ray photoelectron spectroscopy (XPS), X-ray diffraction (XRD), Transmission Electron Microscopy (TEM), Scanning Electron Microscopy (SEM), and Atomic force microscopy (AFM).

2.3.1 Spectroscopy

In general, spectroscopy involves obtaining information from the interaction of electromagnetic radiation with a physical system. Other modes of spectroscopy that do not require radiation like force spectroscopy, which can be performed using an atomic force microscope, are not as widely referred as spectroscopy.

Different spectroscopy methods deal with various interactions between a sample and electromagnetic waves. For instance, Raman spectroscopy studies the photons scattered from the sample and vibrational modes of molecules. Also, various wavelengths can provide information about a range of atomic and molecular transitions presented in the following table:

Table 2.1 | The Wavelength Ranges and Sources of the Radiation.

Source of radiation	Radiation type
nucleus	γ -rays
core-level electrons	X-rays
valence electrons	Ultraviolet (UV)
valence electrons	Visible (Vis)
molecular vibrations	Infrared (IR)
molecular rotations; electron spin	Microwave
nuclear spin	Radio waves

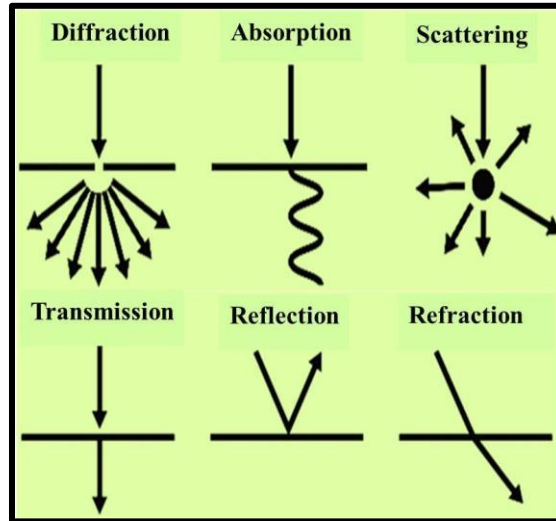


Figure 2.15 | The sketch shows different forms of energy exchange between a photon and the Sample.

2.3.2 Raman Spectroscopy

Raman spectroscopy involves illuminating a sample with laser beam and collecting the scattered light. Raman spectrometer detects the Raman shifts in the sample. Raman shift is the change in the wavenumber of the emitted photon with respect to wavenumber of the laser source. Each material has a specific Raman shift. Therefore, detecting the shift provides essential information for identifying a sample.

C.V. Raman was awarded the Noble prize in 1930 for discovering the Raman Effect that got more popular after the discovery of lasers in the sixties. When a laser beam irradiates a sample, most of the photons scatter elastically while a small percentage undergoes inelastic scattering.

Studying the energy of inelastic scattered photons is the subject of Raman spectroscopy.

Elastic scattering or Rayleigh scattering refers to the case where the emitted and scattered photons have equal wavelength/frequency.

In Raman spectroscopy, an incident photon creates an electron-hole pair. Either the hole or the electron emits or absorbs a phonon. Then they recombine and create a photon. Finally, the system restores the ground state with an additional phonon. If the energy of the absorbed photon is larger/smaller than that of the scattered one, the process is called stokes/anti-stokes. The Stokes processes can be observed only at low temperatures.

2.3.2.1 Raman Applications in Material Science

In material science, Raman scattering is mostly used to identify crystalline or polycrystalline insulators. In addition, some amorphous materials can be recognized by their specific bands (instead of peaks) like quartz. Raman spectroscopy is a powerful method for analyzing layered materials (even if they are metallic). In many cases, it can be utilized to determine the number of layers.

In the case of heavily doped semiconductors, Raman spectrum can be used to obtain electronic density of states. Raman scattering has also been used to study the growth of quantum dots in polar and non-polar planes of crystal structures.

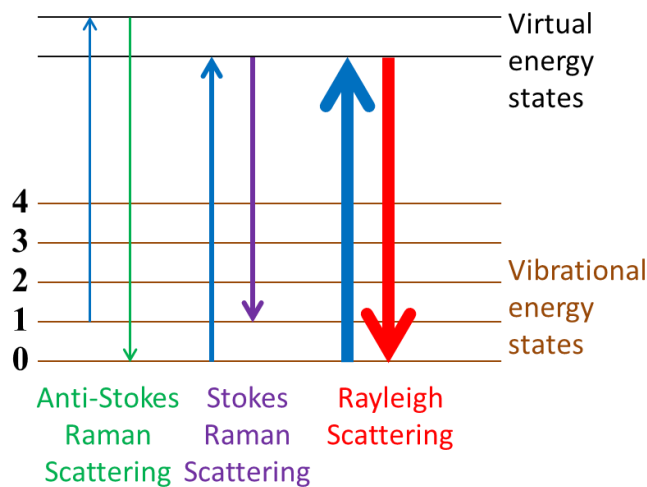


Figure 2.16 | Raman spectra energy states diagram.

2.3.3 Photoluminescence Spectroscopy

In photoluminescence (PL) spectroscopy, a laser beam is shined on the sample. The incident photons excite the electrons to higher energy levels. The photo-excitation of electrons is followed by a spontaneous emission.

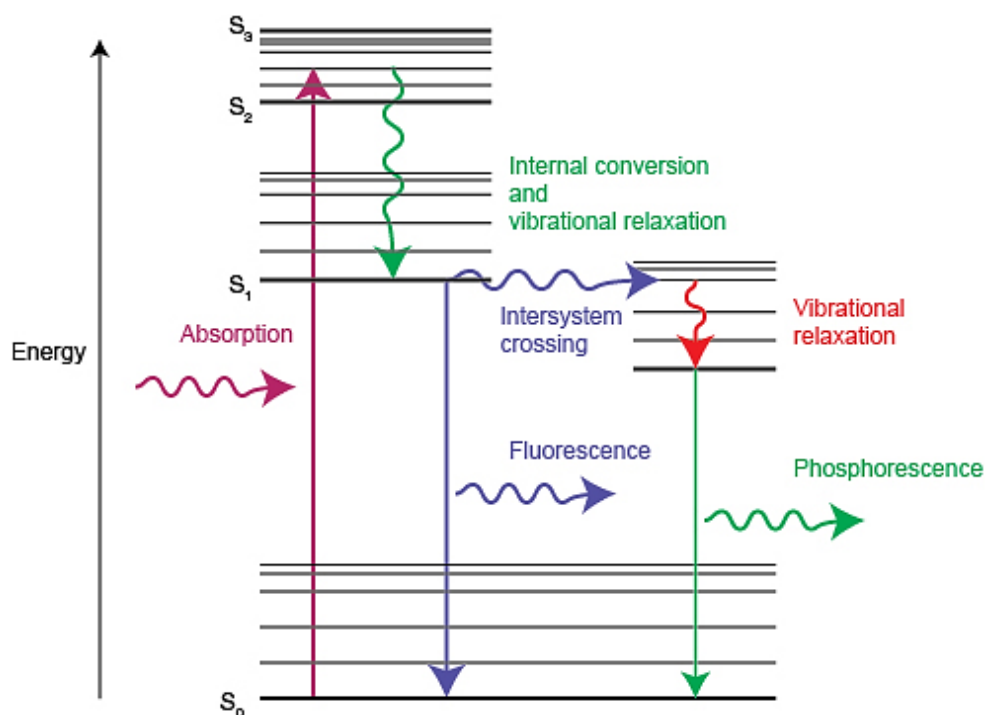


Figure 2.17 | Photoluminescence energy states diagram.

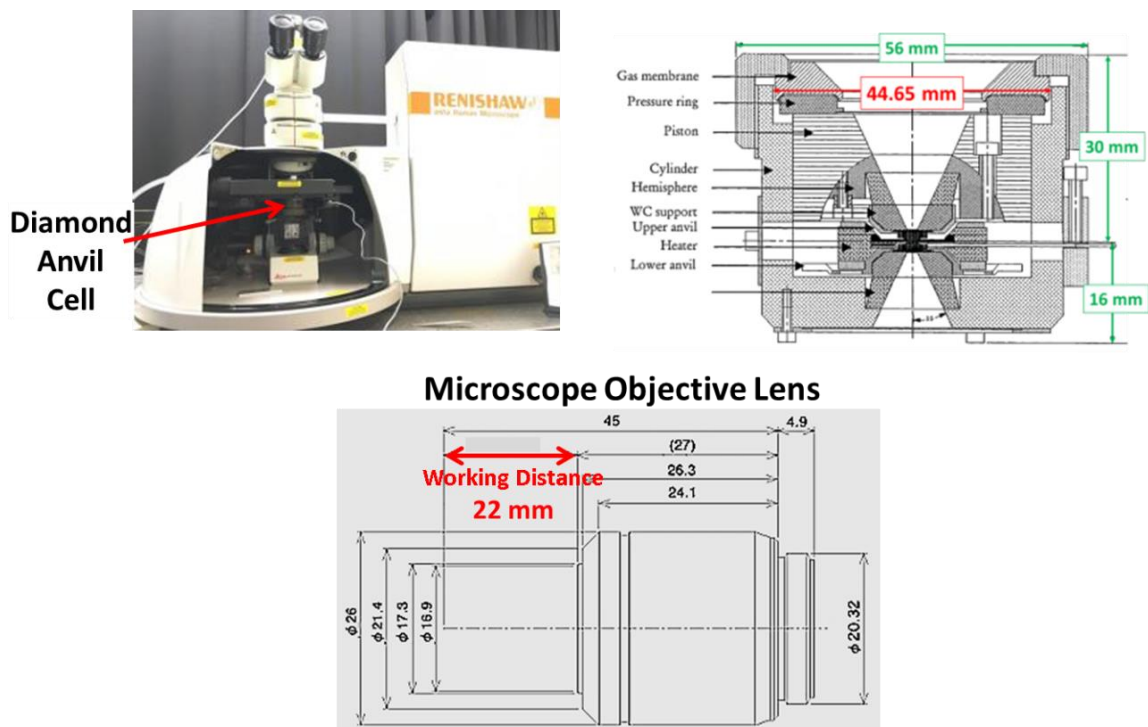


Figure 2.18| Our modified Raman and PL system for in situ high-pressure measurements.

2.3.4 UV/Vis/NIR Absorption

The energy of a molecule is composed of the energy of the electrons, vibrational energy of its atoms or rotational energy of the molecule itself. Since the electronic energy states are widely spaced, a high-energy beam is required to excite the molecule from one level to another. The complex substances have closer energy states and can absorb photons in near ultraviolet or visible region. The spacing between vibrational energy states is closer than electronic states and corresponding absorption happens in infrared region. Usually, the absorption peak obtained with spectrometer is a broad spectrum and includes all the three electrical, vibrational and rotational energy transitions.

The UV-VIS spectrometer provides the absorbance wavelength of a sample. Then the energy of the compound is given by $E = hc/\lambda$ where E = energy, h = Planck's constant,

c = speed of light, and λ = wavelength. In addition, if either of extinction-coefficient or molar-absorptivity is known, one can calculate the other one by applying the Beer's law

$$A = \epsilon bc$$

Where A is the measured absorbance, ϵ is the molar extinction coefficient and b is the path length, and c = concentration.

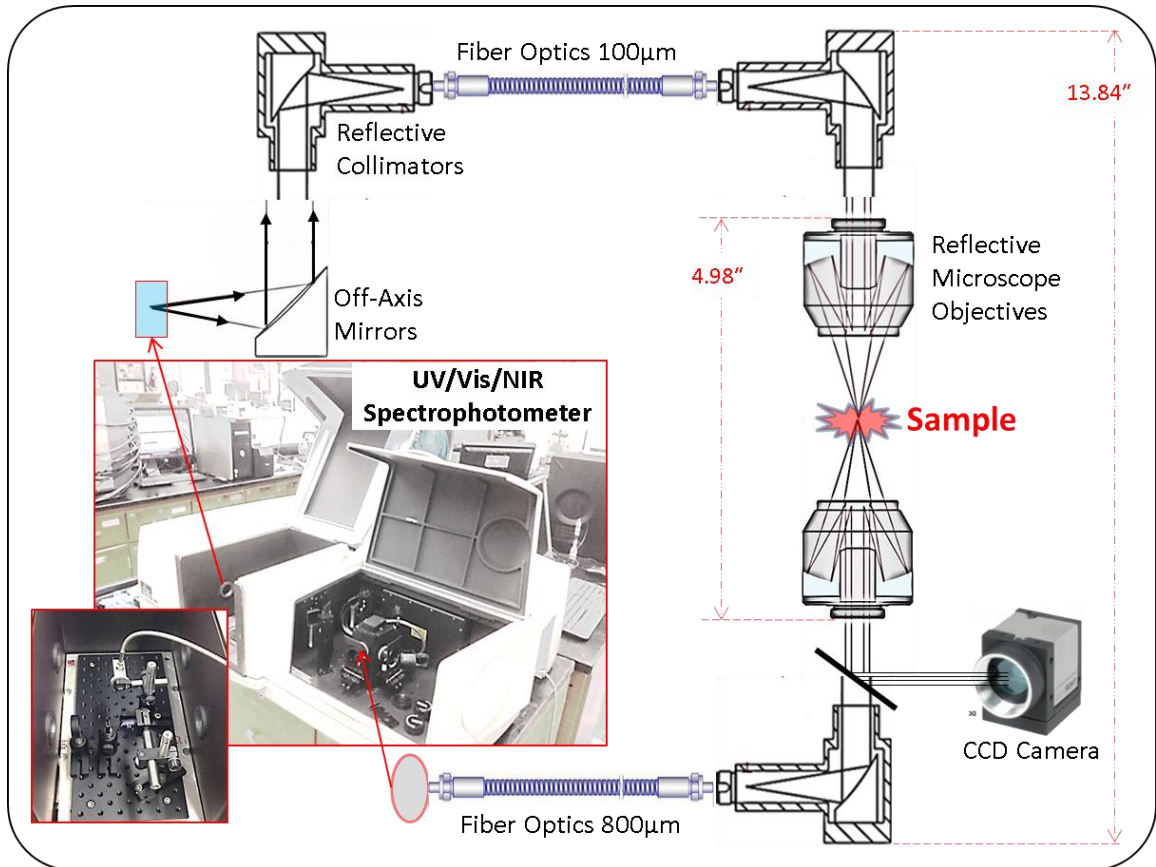


Figure 2.19 | Our developed optical setup for in situ high-pressure UV/Vis spectroscopy.

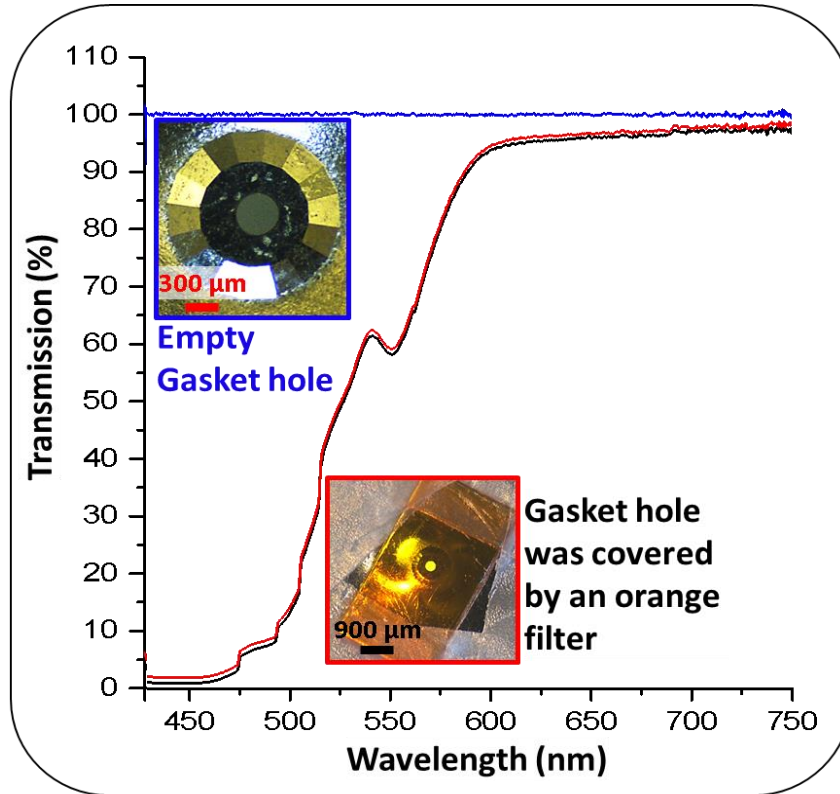


Figure 2.20| Testing Optical Setup for In Situ High-Pressure UV/Vis Spectroscopy.

Transmission Absorption Spectra of a Gasket Hole (200 μm in diameter) Covered by Orange Filter.

2.3.5 Powder X-ray diffraction (XRD)

XRD is a valuable method for identifying unknown crystalline material. It also provides information on unit cell dimension. Since the x-rays wavelength is comparable to the size of atoms, they provide a useful tool to study the structural arrangement of atoms and molecules in a crystal. When X-rays illuminate a crystalline sample, arrays of atoms reflect the x-ray waves. The reflected waves may interfere in a constructive or destructive manner. In case of constructive interference, Bragg's law is used to calculate the spacing "d" between diffracting planes.

$$n \lambda = 2d \sin\theta$$

Where n is an integer, λ is the X-ray wavelength, and θ represents the scattering angle. If the wavelength of reflected X-rays did not change, the scattering is called elastic. Elastic scattering provides information on electron distribution. In contrast, in the inelastic scattering, some of the energy is transferred from X-ray photons to the electrons. The inelastic process can be used to probe the excitations of a sample.

The X-ray diffractometer consist of X-ray generator, sample holder and X-ray detector. X-ray is mostly generated in laboratories using X-ray tubes. In a cathode ray tube, a filament is heated to generate electrons. Then applying a high voltage accelerates the electrons toward the sample. A goniometer rotates the sample under the incident X-ray at an angle θ while, the detector rotates at 2θ . Sometimes, the crystal structure of the sample can be improved through annealing before performing XRD. The typical data obtained with XRD consist of a plot that shows X-ray intensity versus the angle 2θ ranging from 5° to 70° .

2.3.6 X-ray Photoelectron Spectroscopy (XPS)

X-ray Photoelectron Spectroscopy (XPS), is a powerful surface analysis technique. In this method, X-ray beams illuminate the sample leading to ionization and consequently emission of inner shell electrons. The kinetic energy of emitted electrons is measured at a distance of 1-10 nm from the sample. Since each element has a specific binding energy corresponding to each atomic orbital, the data can be used to probe the electronic state and composition of the sample surface. XPS spectrum demonstrates the rate of electron emission at each kinetic energy. Each peak indicates the presence of a particular element and the peak intensity is proportional to the element concentration in the probed region.

Since the energy of incident beam ($h\nu$) is known, the binding energy (BE) can be calculated using the following equation:

$$KE = h\nu - BE - \Phi$$

Where KE is the measured kinetic energy and Φ represents the work function of emitted electrons. The binding energy can be altered depending on the local environment of atoms and the oxidation state. For instance, the binding energy is larger for the atoms with greater positive oxidation state. Thus, XPS can be employed to distinguish various oxidation states and chemical surroundings.

2.3.7 Scanning Electron Microscopy (SEM)

Scanning electron microscope is a tremendously beneficial tool for studying the surface of a sample as it overcomes the resolution limit of the optical microscope. SEM uses a focused beam of electrons to scan the sample. The electrons are produced using an electron gun at the top of SEM column. A filament is heated to a temperature of 2000-2700 K that leads to the thermionic emission of electrons. A series of electromagnetic lenses are used to focus the electron beam on the sample. The interaction between the sample and the electron beam results in elastic and inelastic scatterings. The most common SEM mode to image the surface topography works by detecting inelastically scattered electrons called secondary electrons. Secondary electrons are low energy particles emitted by the atoms located near the sample surface.

The other common mode is imaging by backscattered electrons. They are scattered elastically from nuclei without losing energy. This method has a greater penetration depth and is less sensitive to the sample surface comparing with secondary electrons. However, this mode provides useful information about the atomic mass of the nuclei.

Another possible form of emission from targeted sample is the radiation of high-energy X-ray photons. This method is referred as energy dispersive analysis of X-ray (EDAX) and is used to probe the elemental composition of a sample.

2.3.8 Transmission electron microscope (TEM)

TEM also uses an electron beam to image a sample. Similar to SEM, an electron gun is used as the beam source. Then, the electromagnetic lenses focus the beam on the sample. A portion of the electrons transmits through the sample while the others undergo scattering. TEM detects the transmitted electrons using a fluorescent screen to form the image. Thicker parts of the sample or regions with higher atomic density appear darker due to electron absorption, while the thinner parts appear brighter. In this mode, an aperture can be used to block the scattered electrons. The transmission intensity depends on the electron transparency and thickness of the sample. This signifies the importance of sample preparation in TEM imaging. The sample thickness should be below 100 nm, which limits the choice of samples.

In the case of crystalline samples, electrons scatter according to Bragg's law and construct a diffraction pattern. The diffraction intensity depends on the orientation of atomic planes with respect to the electron beam. Detecting the elastically scattered electrons through the electromagnetic lenses results in a pattern composed of spots. Each spot represents a specific atomic plane. This method provides information on the phase, atomic arrangements, and planes orientation.

2.3.9 Atomic Force Microscope (AFM)

Atomic force microscopy is a method to study the topography of the sample by detecting the forces between the sample and AFM tip. The tip is attached to a shiny cantilever. The forces between sample and the tip result in bending of the cantilever. The backside of the cantilever is illuminated by a laser beam. The reflection from the cantilever is detected with a photo-diode. Small displacement or bending of the cantilever moves the beam on the photodiode. The image is formed according to the movement of the beam. Most AFM operate in two different modes; tapping mode and contact mode.

In tapping mode, a voltage is applied to the cantilever causing it to oscillate at its resonance frequency. Forces applied by the sample affect the frequency. In this mode, the image is created by detecting the frequency variations. The software also provides images formed by detecting the amplitude and phase of the cantilever oscillations. The phase image demonstrates the changes in sample material. AFM in contact mode operates by moving the sample under the tip so that the forces between these two remain constant. The movement of the sample or the tip is controlled with a piezo-electric ceramic attached to the AFM scanner.

AFM is a precise method for measuring the thickness and particle size at the surface. The AFM tip can be replaced with a magnetic tip to image the magnetic properties of the sample.

2.4 Synthesis Method

2.4.1 Rhombohedral α -AgGaO₂

These synthesis experiments were conducted using “Diacell HeliosDAC” diamond anvil cell (DAC) (Almax EasyLab Inc.). The high-pressure cell was equipped with an internal resistive heater with capability to heat up the sample to the temperatures of up to 1000 °C. To measure the temperature a thermocouple (K-type) was used which placed close to the diamond culet and sample chamber. Diamond anvils with 820 μm flat culets were used in the cell and samples were loaded into a 250- μm hole of Inconel gasket. To calibrate the pressure, we utilized the R1-luminescence line shift of ruby crystal under the pressure. A mixture of hydrogen (2%) and argon (98%) gas was used to avoid cell oxidation during the heating process. The experiment duration for each synthesis process was two hours. Synthesis of α -AgGaO₂ was possible at temperatures from 480 °C to 620 °C and pressures between 1.5 and 10 GPa. Twenty samples including several control samples were prepared. The precursors were Ag₂O and Ga₂O₃ powders mixed at various weight ratios. Some of the control samples were prepared using pure Ag₂O or Ga₂O₃ powders. The influence of high-pressure only and high temperature only on mixture of Ag₂O and Ga₂O₃ powder was monitored during control experiments. All the samples were characterized using different techniques including Raman spectroscopy with red laser (633 nm) and Renishaw inVia Raman/PL microscope, scanning electron microscopy (SEM), transmission electron microscopy (TEM), selected area electron diffraction (SAED) and energy dispersive X-ray spectroscopy (EDX). TEM samples were prepared by dispersing powders on dedicated 3.05 mm-diameter, 300 mesh copper grid-supported amorphous lacey carbon films. In our synthesis experiments of α -

AgGaO₂, mixtures of the following two commercially available oxide powders were used as the precursors:

- A. Silver (I) Oxide (Ag₂O), 99.99% (metals basis) from Alfa Aesar (CAS: 20667-12-3) and
- B. Gallium (III) oxide (Ga₂O₃), 99.99% (trace metal basis) from Acros Organics (CAS: 12024-21-4).

The precursors were loaded into a diamond anvil cell (DAC) where high-pressure and high-temperature conditions were produced. We carried out several experiments with the temperatures between 200 °C and 600 °C and pressures between 1 GPa and 10 GPa. The DAC used for these experiments consisted of two diamonds with 0.82 mm culets. The gasket was made of 0.3 mm-thick Inconel alloy foil and a 0.25 mm-diameter hole served as the high-pressure reaction chamber. The loading of precursor samples into the DAC was performed under a stereo microscope with magnification power of 180 X. Experimental conditions and parameters of 20 samples prepared for this work, including 7 control samples are listed in Table S1 below.

Table 2.2 | List of samples prepared for this work

sample #	Precursor			Temperature (°C)	Pressure (GPa)	Time (hrs)	α -AgGaO ₂ Raman peaks
	Ga ₂ O ₃	AgO ₂	molar ratio				
1	+	-	-	~ 25	~ 0	-	×
2	-	+	-	~ 25	~ 0	-	×
3	+	-	-	600	~ 0	2	×
4	-	+	-	600	~ 0	2	×
5	+	+	1:2	600	~ 0	2	×
6	+	-	-	600	10	2	×
7	-	+	-	600	10	2	×
8	+	+	1:1	600	10	2	✓
9	+	+	3:1	600	10	2	✓
10	+	+	1:3	600	10	2	✓
11	+	+	1:2	600	10	2	✓
12	+	+	2:1	600	10	2	✓
13	+	+	1:1	480	10	2	✓
14	+	+	3:1	480	10	2	✓
15	+	+	1:1	320	10	2	×
16	+	+	1:1	600	6	2	✓
17	+	+	1:1	600	3	2	✓
18	+	+	1:1	600	1.5	2	✓
19	+	+	1:1	200	1.5	2	×
20	+	+	1:1	400	1.5	2	×

All mixed samples that were subjected to the pressure above 1.5 GPa and a temperature above 400 °C show 4 Raman peaks characteristic of α -AgGaO₂ in the region 300 cm⁻¹ to 700 cm⁻¹. However, the signal was most intense for the samples synthesized under higher temperature and mixed in the 1:1 ratio. TEM analysis indicated that these samples had a relatively uniform phase. The only other Raman peaks were attributed to silver oxide or gallium oxide initial phases; and were present because of non-stoichiometric mixture due

to a very small volume of samples for DAC experiments. This non-stoichiometric effect was also revealed in SEM and TEM study. In addition to crystallites of α -AgGaO₂, we also observed un-reacted grains of Ag₂O or Ga₂O₃.

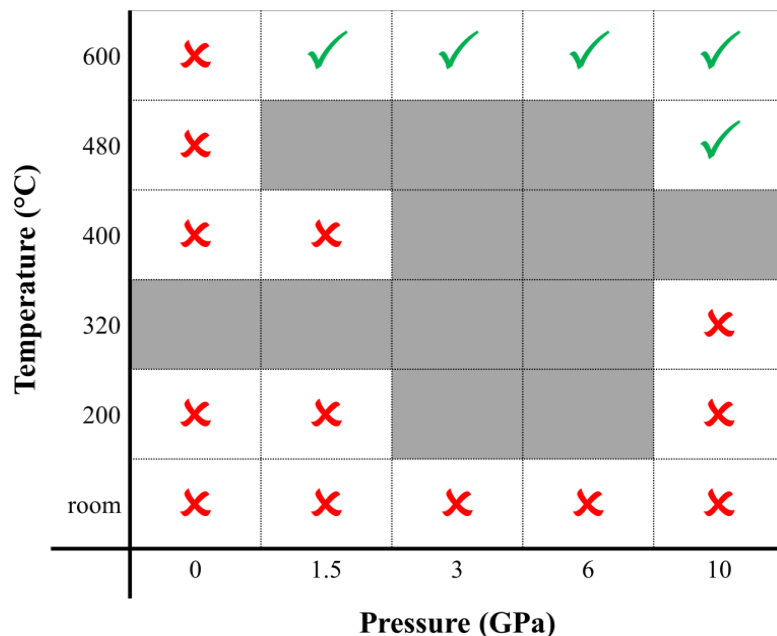


Figure 2.21 | Temperature-Pressure diagram representing conditions used in our DAC-based α -AgGaO₂ synthesis experiments. Each square represents one experiment and its specific conditions. Green check mark denotes formation of rhombohedral α -AgGaO₂. Red crosses show experiments, which did not produce rhombohedral α -AgGaO₂.

2.4.2 Synthesis Three-Dimensional (3D) Graphene Foam

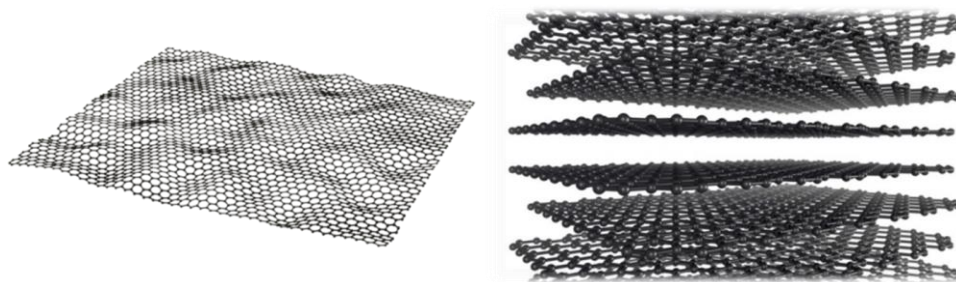


Figure 2.22 | Schematic image of single graphene sheet and graphite layers.

In this work three-dimensional graphene was synthesized by pyrolysis of organic precursor, citric acid ($C_6H_8O_7$). Commercial Ni foams (Marketch International, Inc., Port Townsend, USA), 346 g/m^2 in surface density, 1.6 mm in thickness and $>99.9\%$ purity were used to catalyze the graphene growth. Firstly, the nickel foams were washed and sonicating with ethanol and acetone for 10 min, respectively. Then they were immersed in a 5M HCl acid solution for about 20 min to remove the oxide layer on their surface, and finally rinsed several times with deionized water before dipping to the concentrated citric acid solution. The nickel foams covered with citric acid were dried at $70\text{ }^\circ\text{C}$ in an oven for about 6 hours. Secondly, the nickel foams transferred to the tube furnace for annealing at $1000\text{ }^\circ\text{C}$ in the presence of Ar and H_2 for 10 min.

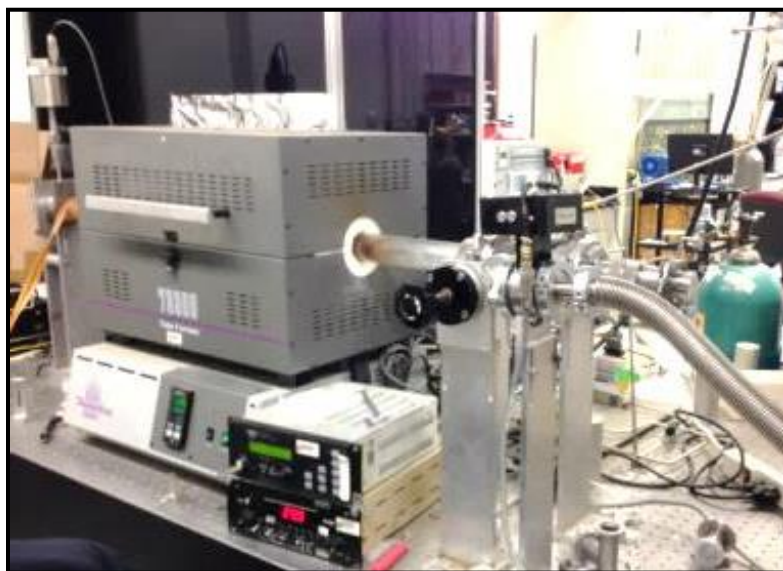


Figure 2.23 | Chemical Vapor Deposition System setup. It was used for both CVD and the developed pyrolysis methods.

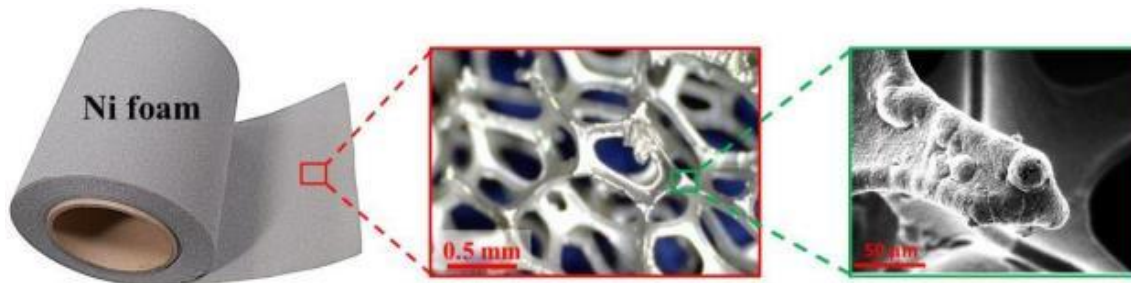


Figure 2.24 | Optical and scanning electron microscopy (SEM) images of nickel foam.

Ni Foam etched by H ₂ SO ₄				Ni Foam etched by HCl			
5M		6M		20 min		30 min	
Low Con. Citric Acid	High Con. Citric Acid	Low Con. Citric Acid	High Con. Citric Acid	Low Con. Citric Acid	High Con. Citric Acid	Low Con. Citric Acid	High Con. Citric Acid
500 °C	500 °C	500 °C	500 °C	500 °C	500 °C	500 °C	500 °C
650 °C	650 °C	650 °C	650 °C	650 °C	650 °C	650 °C	650 °C
800 °C	800 °C	800 °C	800 °C	800 °C	800 °C	800 °C	800 °C
1000 °C	1000 °C	1000 °C	1000 °C	1000 °C	1000 °C	1000 °C	1000 °C

Figure 2.25 | Photograph of three-dimensional graphene foams fabricated at 500, 650, 800, and 1000 °C temperature and with different pre-treatment of nickel surface.



Figure 2.26 | Nickel foam (center), three-dimensional graphene before (left) and after (right) etching the nickel template.

The flow rates the gases ($H_2:Ar$) were 20:13 sccm, respectively. After 10 min of annealing, the sample was cooled by rate of ~ 10 °C/min. Nitrogen doped graphene samples were synthesized the same method by adding nitrogen-containing organic materials to the solution of citric acid. In this work caffeine ($C_8H_{10}N_4O_2$), urea (CH_4N_2O) and acetaminophen ($C_8H_9NO_2$) were used with citric acid solution as the source of carbon and nitrogen.

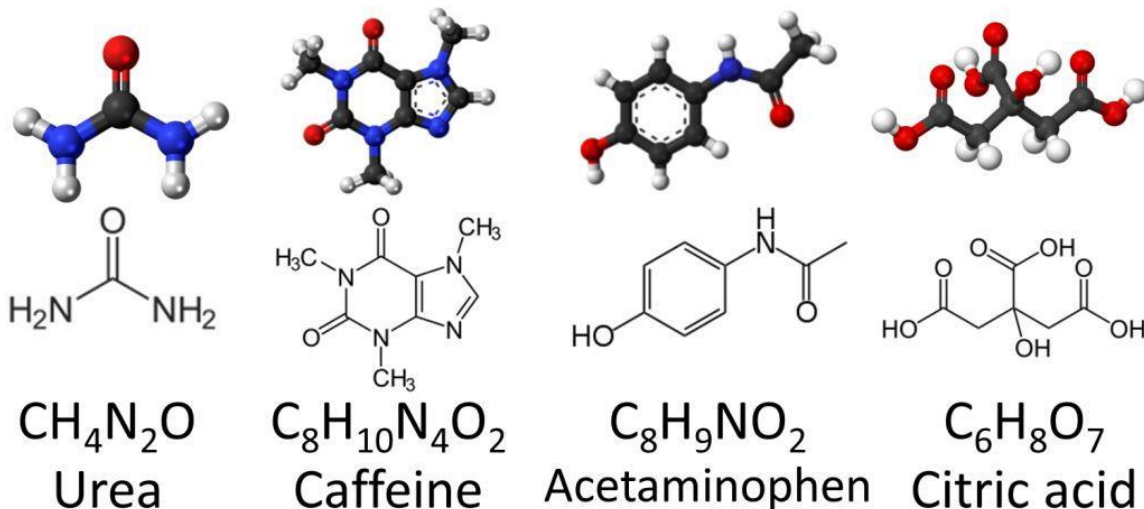


Figure 2.27 | Molecular structure and chemical formula of organic precursors used for graphene growth.

All solutions were made to be saturated with equal weight portions of the organic precursors. Raman spectroscopy data were collected using red laser and Renishaw inVia

Raman/PL spectrometer. The samples were analyzed with a HeNe laser excitation of 633 nm, using a 50X objective. Surface morphology characterization of the samples was examined using a scanning electron microscope.

2.4.3 Synthesis of Phosphorene

Few-layer black phosphorus or phosphorene can be produced by exfoliating the bulk black phosphorus. Due to the high cost of the black phosphorus, we decided to prepare this precursor. In this work, we prepared bulk black phosphorus using short way transport reaction based on the research work by Köpf et al. [133]. The research group leads by Dr. Nilges have been developed this synthesis method through series of improvements that have been published [133-135]. In this method, tin(IV) iodide (SnI_4), tin (Sb), and red phosphorus are used as the precursors to synthesis the black phosphorus. Precursors annealed at ~ 600 °C in high vacuum environment. For this purpose we used Pyrex glass tube with one open end and filled it with 10 mg of tin(IV) iodide, 20 mg of tin, and 400 mg of red phosphorus. Then, using the vacuum system shown in Figure 2.28 the Pyrex tube was evacuated to $\sim 10^{-6}$ Torr. To reach such a high vacuum ($\sim 10^{-6}$ Torr) we used a combination of two vacuum pumps, an oil diffusion pump and a mechanical (rotary vane) pump. The diffusion pump typically cannot start working from atmospheric pressure and need a backing (roughing) pump.

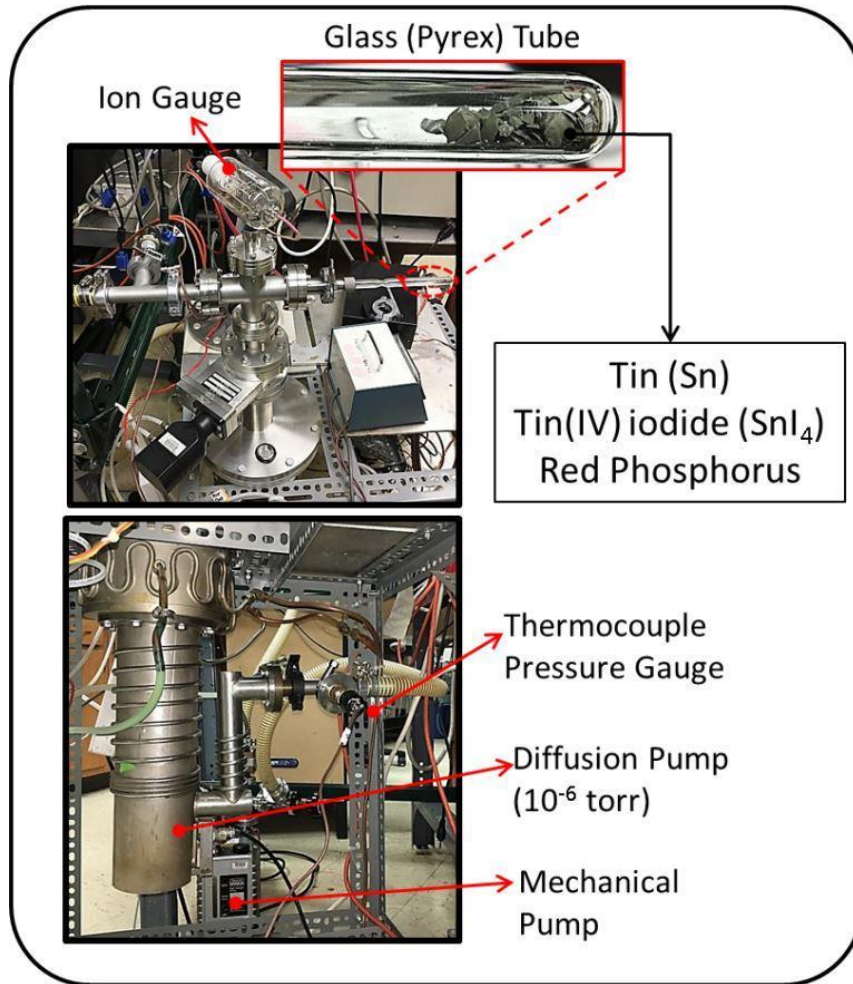


Figure 2.28 | Vacuum system for synthesis of black phosphorus by short way transport reaction methods.

Using an oxyacetylene torch the Pyrex tube was sealed and transferred to the furnace for the annealing process. The sealed Pyrex tube was placed in the furnace in a way that there was a temperature gradient (~ 40 °C) between the two ends of the tube. This temperature gradient is necessary for the conversion process of red phosphorus to black phosphorus. The choice of the Pyrex glass compare to the quartz has some advantageous such as easier sealing process but the Pyrex critical point is close to the annealing

temperature of the precursors ($\sim 600\text{ }^{\circ}\text{C}$) which caused some difficulties in annealing process.

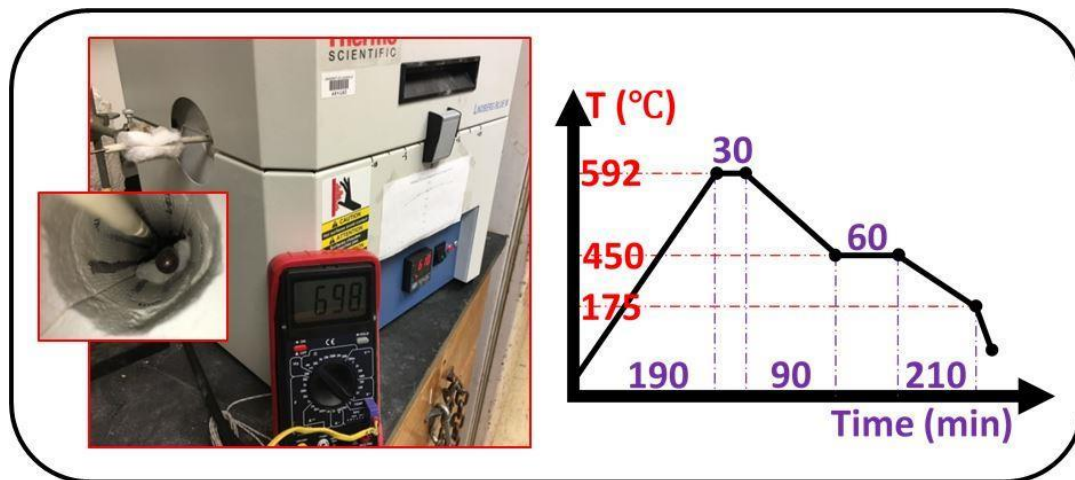


Figure 2.29 | The tube furnace and the temperature profile that was used to synthesis black phosphorus.

During the annealing process, first, the temperature was increased from room temperature to $\sim 600\text{ }^{\circ}\text{C}$ in 190 minutes and the sample was kept in that temperature for 30 minutes. Then the temperature was decrease to $\sim 450\text{ }^{\circ}\text{C}$ in 90 minutes. The samples were held at $450\text{ }^{\circ}\text{C}$ for 60 minutes. Finally, the sample was gradually cooled down to the room temperature. At the end of the annealing process inside the Pyrex tube black phosphorus crystal was formed. To avoid degradation of the sample we did not expose the sample to open air instead, we removed the black phosphorus from the tube inside the Argon glove box.

The synthesized bulk black phosphorus was used to prepare few-layer black phosphorus through liquid phase exfoliated (LPE) method. In this work dimethylformamide (DMF) with chemical formula, $\text{C}_3\text{H}_7\text{NO}$, was used as the solvent in the process. Sample crystal was suspended in the solvent and was sonicated for 2 hours. After 2 hours sonication the

resulted samples were contained 1-5 layers. However, shorter time of sonication resulted to the samples with significantly more layers. In the next step the samples was placed in a centrifuge with 10,000 rpm for half an hour. During this step the temperature was maintained at about room temperature to avoid any side reaction. The centrifugation separated the phosphorene based on the number of layers in other words phosphorene samples with less number of layers were concentrated at top of the vial container and phosphorene with higher number of layers concentrated at bottom of the container.



Figure 2.30 | Pyrex tubes before sealing and evacuated glass (Pyrex) tube after annealing at 600 °C.

CHAPTER 3: RESULTS AND DISCUSSION

3.1 Rhombohedral α -AgGaO₂

In this work [72], Raman spectroscopy was performed for all prepared samples. A representative set of acquired Raman spectra is shown in Figure 3.1. All the mixed Ag₂O-Ga₂O₃ powder samples that were annealed under high pressure in the DAC feature a group of peaks between 350 cm⁻¹ and 700 cm⁻¹. Intriguingly, none of the control samples demonstrated these peaks (Figure 3.2 and 3.3). This suggested the synthesis of a new phase under the high-pressure and temperature conditions.

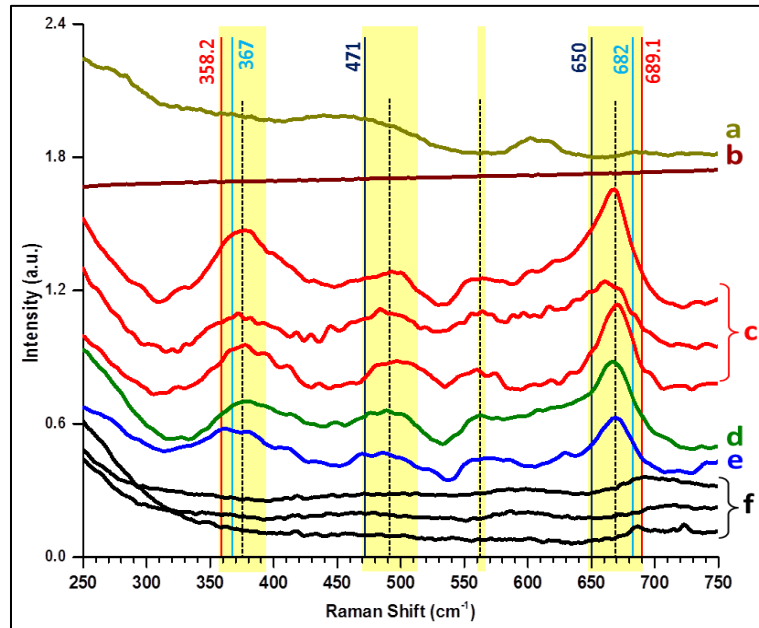


Figure 3.1 | Representative Raman spectra of various samples: (a) Ag₂O (T = 600 °C, P = 10 GPa), (b) Ga₂O₃ (T = 600 °C, P = 10 GPa), (c) Mixed powder of Ag₂O + Ga₂O₃ (1:1,

T = 600 °C, P = 10 GPa), (d) Mixed powder of Ag₂O + Ga₂O₃ (3:1, T = 600 °C, P = 10 GPa), (e) Mixed powder of Ag₂O + Ga₂O₃ (1:1, T = 480 °C, P = 10 GPa), (f) Mixed powder of Ag₂O + Ga₂O₃ (1:2, T = 600 °C, P = ambient). Vertical red lines represent the location of our theoretically calculated Raman modes. Vertical light blue lines show the positions of Raman modes calculated by Kumar and Gupta [136]. Vertical dark blue lines show the location of Raman peaks measured by Nagarajan and Tomar [80].

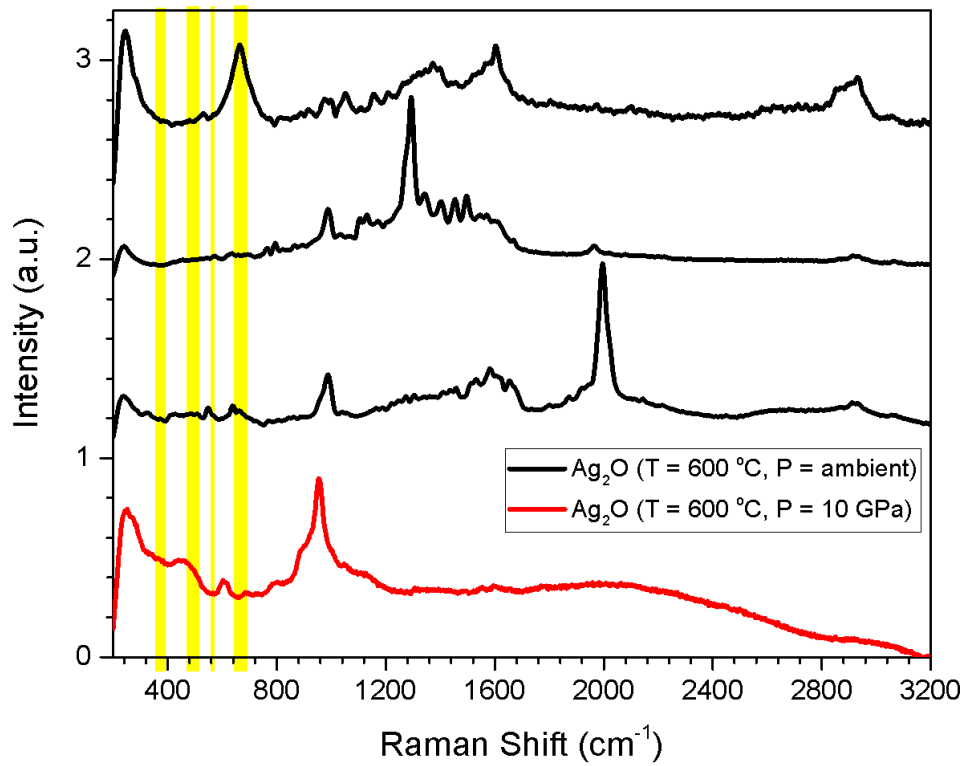


Figure 3.2 | Raman spectra of pure silver (I) oxide before (top three curves) and after (bottom curve) DAC experiment. Before applying high pressure, Ag₂O is unstable under the illumination of 633 nm laser during Raman measurements. Hence, several shown spectra, measured from the same area at different times differ from each other (top three curves). However, after the high-pressure experiment, Ag₂O is stable, and its spectrum

(bottom curve) does not change under laser illumination. The spectral regions shaded in yellow indicate the location of four peaks characteristic of rhombohedral α -AgGaO₂.

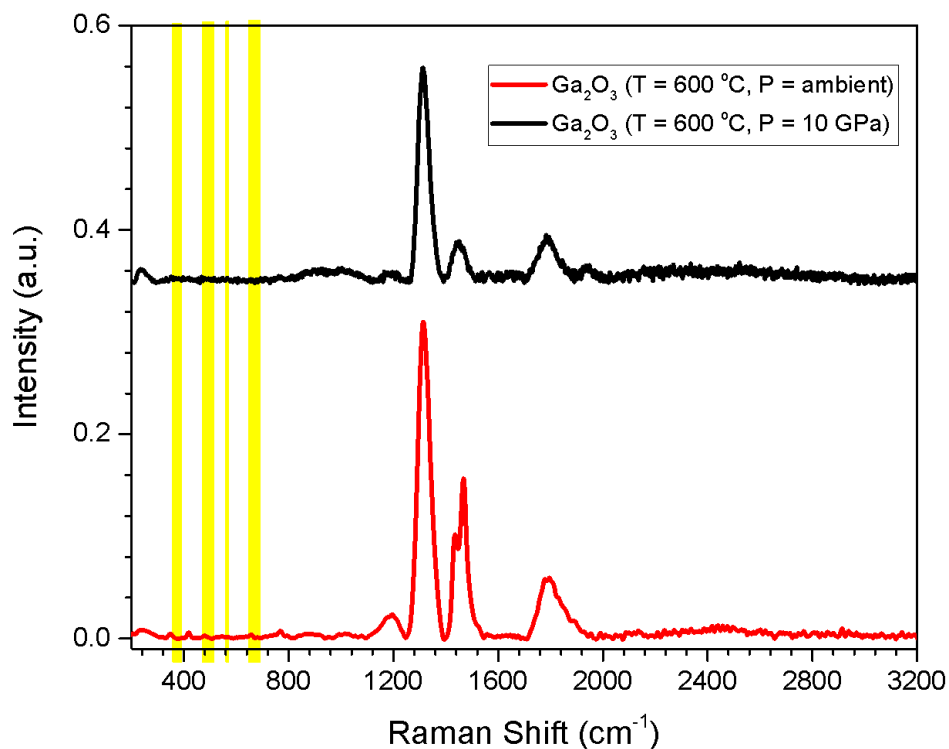


Figure 3.3 | Gallium (III) oxide before (top curve) and after (bottom curve) applying high pressure. The spectral regions shaded in yellow indicate the location of four peaks characteristic of rhombohedral α -AgGaO₂.

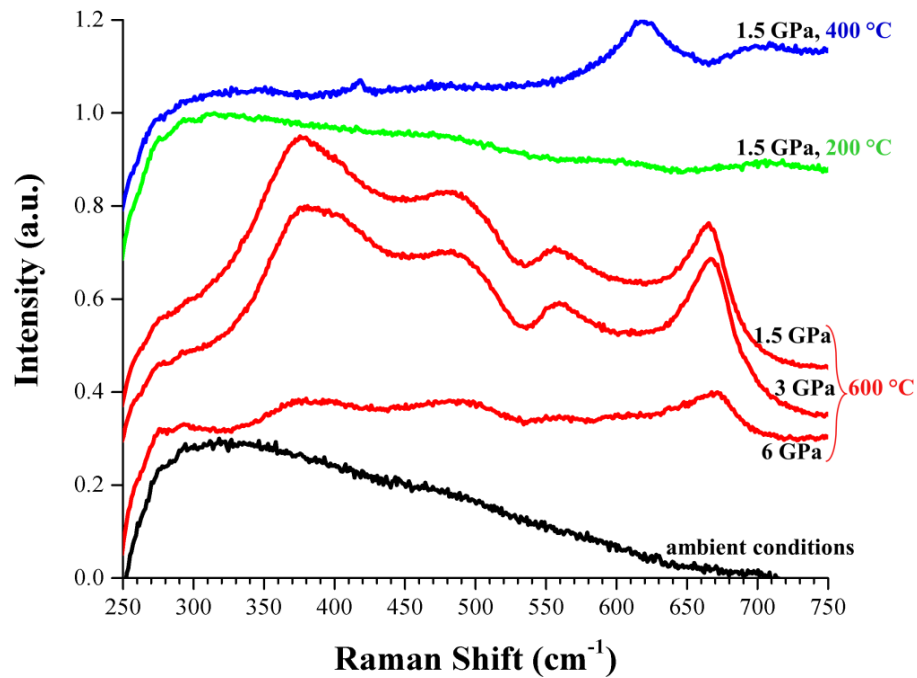


Figure 3.4 | Representative Raman spectra of a mixed powder of $\text{Ag}_2\text{O} + \text{Ga}_2\text{O}_3$ with a molar ratio of 1:1 in different pressure and temperature conditions. Characteristic Raman spectrum of rhombohedral $\alpha\text{-AgGaO}_2$ is only present in red spectra.

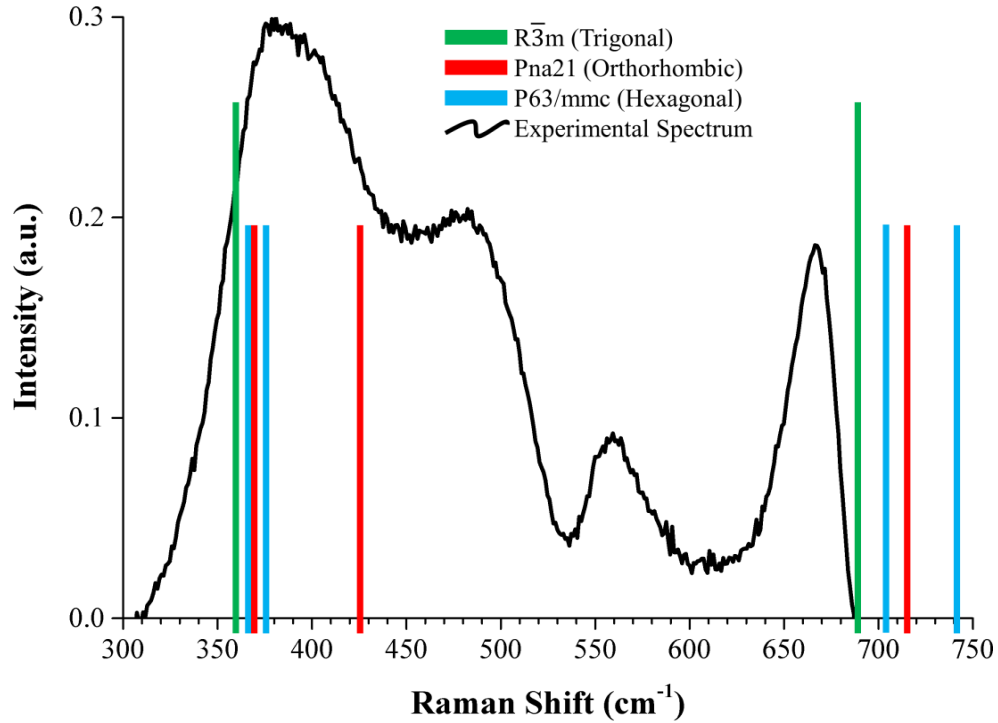
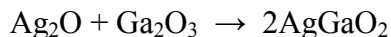


Figure 3.5 | The experimental Raman spectrum of DAC-synthesized AgGaO_2 and calculated frequencies of Raman modes for the three known structures of AgGaO_2 . (There is a five percent uncertainty due to temperature effects.)

To study the structure and morphology of the new phase, we used electron microscopy. SEM results showed relatively uniform nanocrystals in scale of 100-200 nm (Figure 3.6 a). The nanocrystals exhibited surface faceting, which pointed to a highly crystalline structure. This was confirmed by TEM, which again revealed faceted nanocrystals in the same size range (Figure 3.6 b-e). EDX analysis (Figure 3.6) showed that the nanocrystals composed of Ag, Ga and O with the atomic ratio of 1:1:2, respectively. This confirmed that AgGaO_2 was synthesized during high-pressure annealing procedure. We also collected EDX elemental maps from the synthesized material using a 1 nm nanoprobe. The maps provided elemental distributions of Ag, Ga, and O that coincided with the

shape of the crystallite (Figure 3.6 f). Therefore, the data strongly supports the following solid-state direct reaction:



There are three known structures of AgGaO_2 : rhombohedral α - AgGaO_2 , hexagonal α - AgGaO_2 , and orthorhombic β - AgGaO_2 [137]. The most straightforward method to differentiate between them is X-ray diffraction (XRD). However, due to the minuscule amount of available material obtained from the DAC synthesis (c.a. 3 μg in the case of our cell), XRD measurements would require a very intense X-ray source such as synchrotron radiation. Therefore, to identify which phase was formed, we conducted a detailed electron diffraction study instead. For this, electron diffraction ring patterns were acquired from different areas of the TEM grid containing groups of nanocrystals. Because the nanocrystals were very sparsely dispersed on the grid and the groups consisted of only few dozens of nanocrystals, the individual ring patterns were very spotty (Figure 3.9 a). Therefore, the analysis could be significantly hampered by the data quality. However, averaging all our data improved the ring pattern quality greatly (Fig. 3b). We also calculated the rotational average using DiffTools software [138]. The intensity profile was analyzed with Bruker DIFFRAC.SUITE™ software package. First, we considered all the possible crystallographic phases for the combination of gallium, Silver and oxygen. Then we looked through the ICDD PDF2 database to find the best match for the diffraction pattern. The lattice parameters of the best-matching structure, were tuned through the DIFFRAC.EVA software. To fit the the experimental pattern we used the rhombohedral delafossite crystal structure with the lattice parameters $a = 2.99 \text{ \AA}$ and $c = 18.43 \text{ \AA}$ and the the $R\bar{3}m$ space group. These parameters matched perfectly with

the crystal structure of rhombohedral α -AgGaO₂ which belongs to the delafossite type compounds family with the general form of A^IB^{III}O₂. The structure consists of alternating “A” layers of two-dimensional closed-packed “A⁺” ions in the dumbbell O—A⁺—O coordination and slightly distorted edge-shared BO⁻⁶ octahedral layers perpendicular to the c axis [81,82].

We also analyzed the electron diffraction pattern using the pattern matching method and FullProf software suite [139]. The crystal structure model was chosen based on the rhombohedral space group $R\bar{3}m$ (Figure 3.9 d). The solid-line in Figure 3.9 d is obtained by calculating for the X-ray case. Thus, it cannot be directly compared with the experimental result. A similar study of the other two recognized AgGaO₂ structures (with P63/mmc (194) and (c) Pna21 (33) space groups) showed a poor agreement (Figure 3.8). For a hexagonal structure, the refined lattice parameters are $a = 2.996(10)$ Å and $c = 18.986(124)$ Å. These values are in great agreement with the lattice parameters associated to rhombohedral α -AgGaO₂.

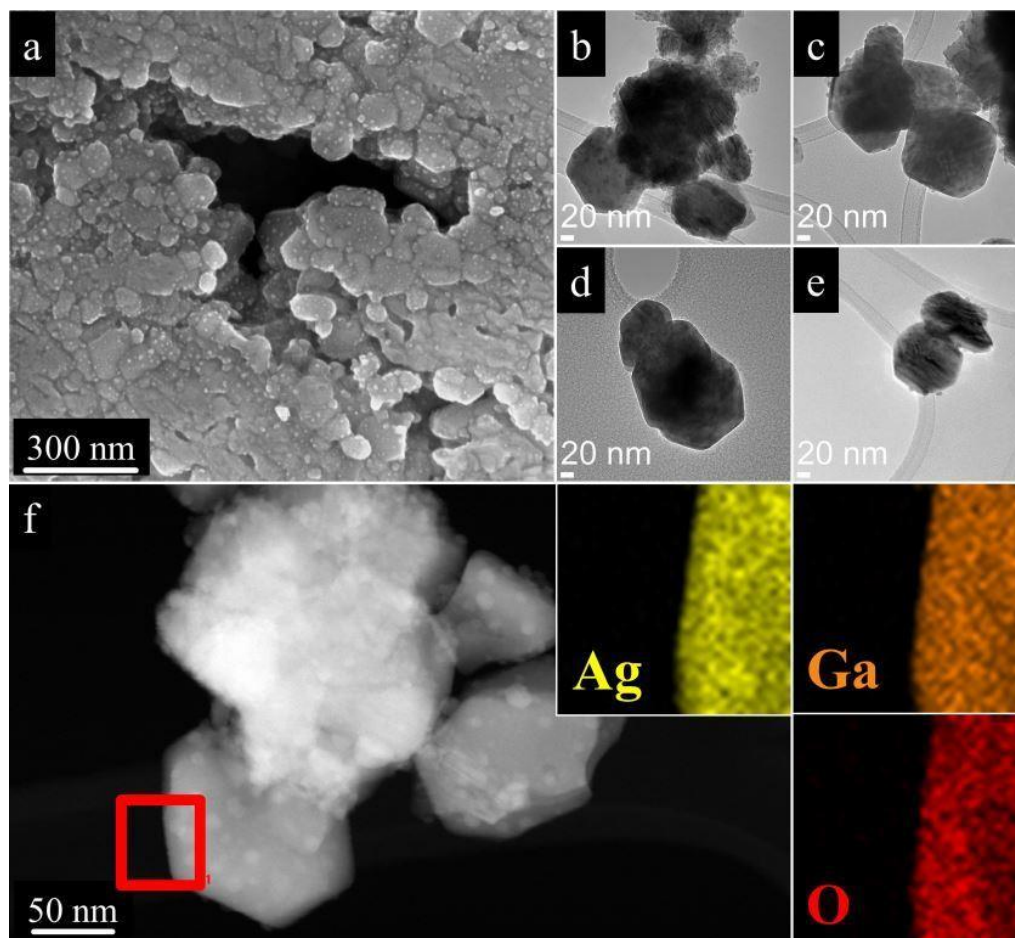


Figure 3.6 | Electron microscopy characterization of AgGaO_2 nanocrystals synthesized during high-temperature DAC experiments: (a) SEM and (b-e) TEM images showing the size and morphology of the nanocrystals. (f) EDX-based elemental mapping was confirming the uniformity and perfect overlap of elemental distributions of Ag, Ga, and O (insets).

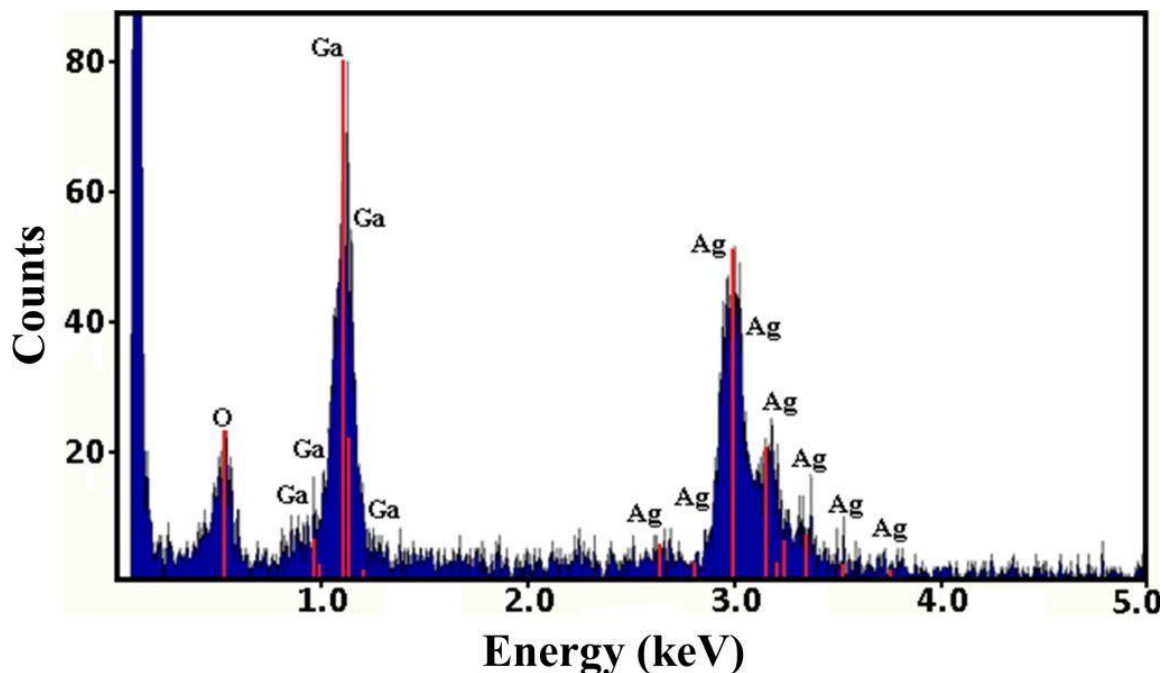


Figure 3.7 | An EDX spectrum from a typical α -AgGaO₂ crystallite synthesized at high pressure.

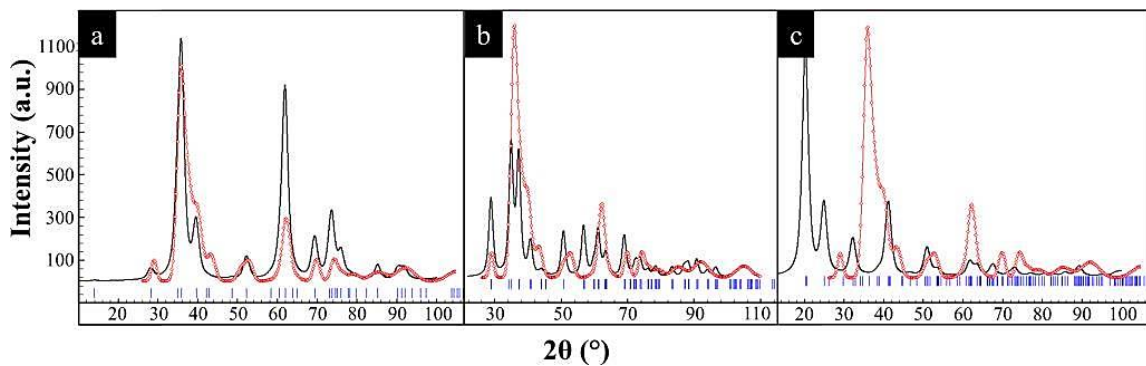


Figure 3.8 | Results of the FullProf-based pattern matching analysis (black curves) of the radial intensity distribution (red curve) of the averaged SAED pattern of the DAC-synthesized AgGaO₂ for crystal structure models of AgGaO₂ with (a) R $\bar{3}$ m (166), (b) P63/mmc (194) and (c) Pna21 (33) space groups. It can be seen that the best fit was obtained for the R $\bar{3}$ m (166) space group.

The crystal structure was further confirmed using single-crystal electron diffraction from individual AgGaO_2 crystallites. Two examples of typical single crystal SAED patterns and associated HRTEM images are demonstrated in Figure 3.10. The d-spacing values obtained from these methods were about 2.49 Å and 2.26 Å respectively which matched well with the d-values of the most intense reflections of the α - AgGaO_2 with the rhombohedral $R\bar{3}m$ crystal structure.

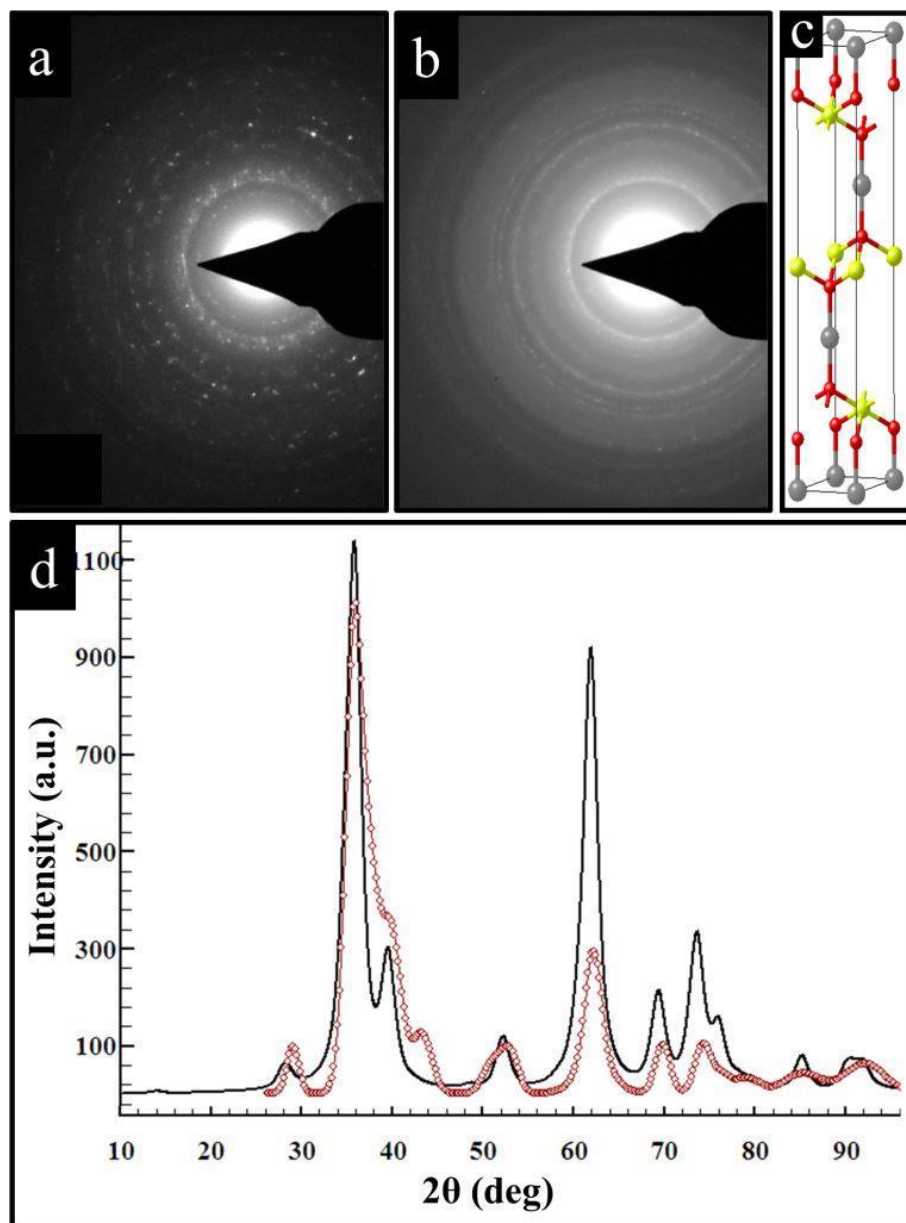


Figure 3.9 | (a) A SAED ring pattern acquired from a typical cluster of a few AgGaO₂ crystallites. (b) The SAED pattern obtained after averaging the data from about 40 separate clusters. (c) The optimized crystal structure of α -AgGaO₂ using our DFT method (see text). (d) Experimental intensity profile obtained after rotational averaging of the pattern shown in b (red curve) and diffraction pattern calculated using the pattern matching mode of the FullProf software suite (black curve).

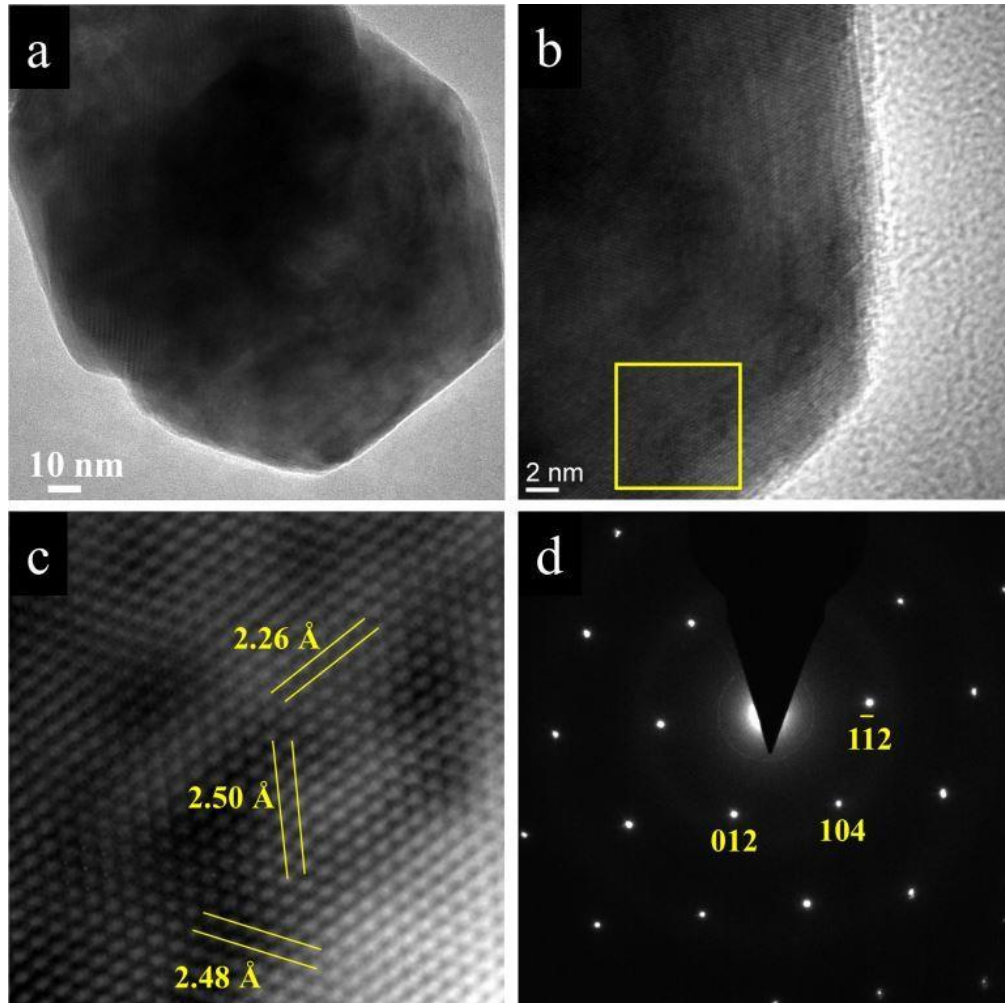


Figure 3.10 | TEM-based single crystal study of individual α -AgGaO₂ crystallite: (a) and (b) low-magnification and high-resolution TEM images; (c) Filtered HRTEM image of the area marked using yellow frame in b; (d) corresponding $[42\bar{1}]$ zone axis SAED pattern measured from this crystallite.

Table 3.1 | Crystallographic Parameters Obtained for the DFT-Optimized α -AgGaO₂.

Cell lattice parameter a	2.87428 (Å)
Cell lattice parameter b	2.87428 (Å)
Cell lattice parameter c	18.28372 (Å)
Cell angle alpha	90.00 (°)
Cell angle beta	90.00 (°)
Cell angle gamma	120.00 (°)
Cell volume	130.81 (Å ³)
Cell formula units Z	3
Space group	R $\bar{3}m$
Volume	130.814 (Å ³)
Moiety formula	AgGaO ₂
D _{x,g} cm ⁻³	7.982
Z	3
Mu (mm ⁻¹)	26.201
F000	282.0
F000'	280.11

Theoretical analysis of vibrational modes was performed to explain the Raman peaks².

For the theoretical study of rhombohedral AgGaO₂ systems of R $\bar{3}m$ symmetry, we used first-principles density functional theory (DFT) in the generalized gradient approximation (GGA) and the Perdew-Burke-Ernzerhof (PBE) [27] form augmented by including

² Performed by Dr. Madhu Menon (Center for Computational Sciences at the University of Kentucky)

Hubbard- U corrections (GGA + U formalism) [140] based on Dudarev's approach [141] as implemented in the Vienna *ab initio* simulation package (VASP) [142]. The U values used for Ga and O were $U_{d,Ga} = 6.5$ eV and $U_{d,O} = 14.0$ eV, respectively. The projected augmented wave (PAW) potential [141] is used to describe the core electrons. After testing for convergence, we settled for a $5 \times 5 \times 5$ Γ -centered pack for \mathbf{k} -vectors sampling. We found that the adequate kinetic energy cutoff for reaching a total energy convergence of 1 meV, was 550 eV. To accelerate the electronic convergence, a Gaussian smearing of 0.05 eV was used. It was acceptable to optimize the atomic positions to proceed without symmetry constraints till the force experienced by each atom is less than 5 meV/Å. The improved structure led to the lattice parameters listed in Table 3.1. For calculating the phonon modes of rhombohedral α -AgGaO₂, the VASP code was used. The calculated vibrational modes are at 79.88, 9.04, 295.54, 358.51, 549.01 (infra-red active modes), 358.21 and 689.14 cm⁻¹(Raman-active modes).

We also calculated the vibrational modes in hexagonal orthorhombic β -AgGaO₂ and α -AgGaO₂ structures (Figure 3.5). The result for the rhombohedral α -AgGaO₂ structure was greatly matching the Raman data. In particular, the two strongest Raman peaks matched with the calculated Raman vibrational modes (Table 3.2). The calculated vibrational modes for the other structures did not match with the experimental data. This further confirms the identified phase. While the *ab initio* calculations did not predict the two weaker peaks in our Raman spectra, they could be noted in the previously reported data for rhombohedral α -AgGaO₂ made by other techniques [80].

To understand the other two Raman modes in our data, we examined all the potential vibrational and stretching or bending modes associated with oxygen and silver bonds in

the AgGaO_2 structure. The two Raman peaks are in excellent agreement with the stretching/bending modes of Ag—O bond [143]. Due to the distortions of atom clusters through the recovery from high-temperature and high-pressure, the peaks are stronger in our samples. This could be the reason for the decreased symmetry, enhancement of weak Raman modes and relaxation of selection rules.

Our experimental and theoretical data is consistent with the DFT calculations reported by Kumar and Gupta [136]. They compared their theoretical results with experimental Raman data published by Nagarajan and Tomar [80]. They suggested potential misassignment of E_g mode near 471 cm^{-1} . However, according to our results the stretching/bending mode of Ag—O bond is responsible for appearing this peak and it does related to E_g mode.

Employing our DFT method, we were able to estimate the band gap energy of α - AgGaO_2 . Previously reported theoretical studies for this phase have only used the standard DFT. This would underestimate the band gap energy. Subsequently, the band gap values are not mentioned in all the previous reports except the one by Maruyama et al. [77]. Even the energy gap estimated by Maruyama et al. is only 0.73 eV. In contrast, our calculations resulted in a band gap of 1.83 eV for this compound. This is much closer to the reported experimental value of 2.38 eV [77,137,144].

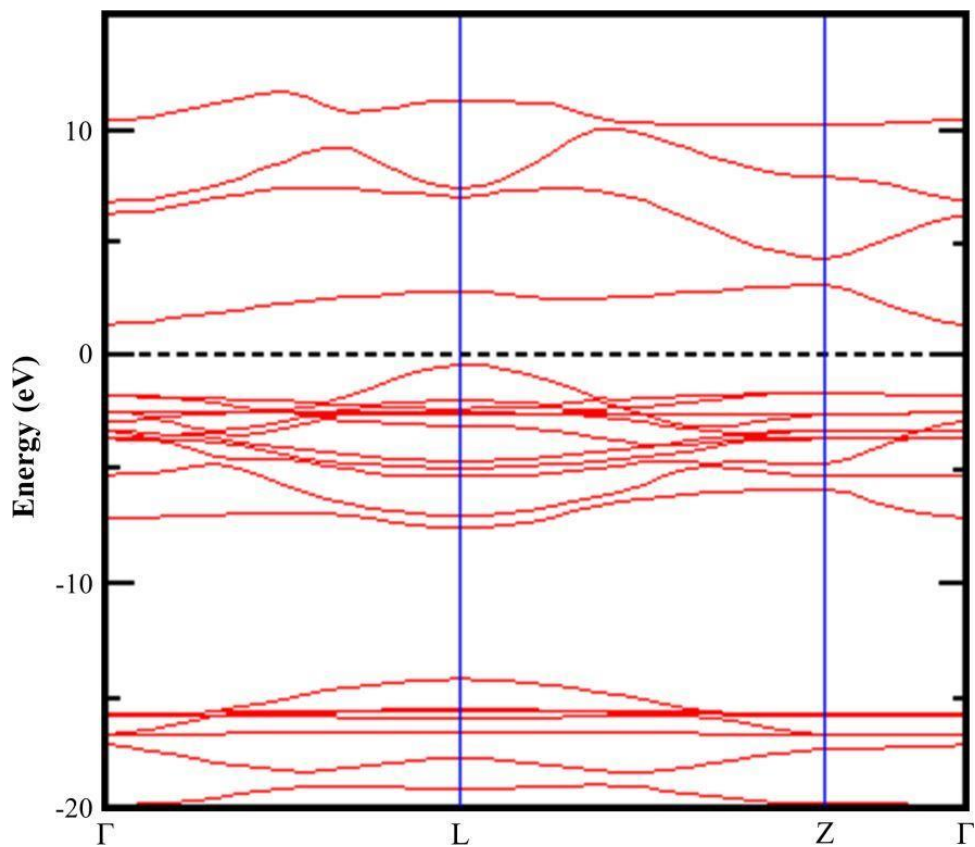


Figure 3.11 | The calculated electronic energy band structure of α -AgGaO₂

Table 3.2 | Experimental and calculated Raman modes.

Raman Mode (cm ⁻¹)	Theor. Calculation		Exp. Result	
	Kumar & Gupta [136]	This work	Nagarajan & Tomar [80]	This work
E _g	367	358.2	-	375
Ag—O	-	-	471	485
Ag—O	-	-	-	560
A _{1g}	682	689.1	650	670

3.2 Three-Dimensional (3D) Graphene Architecture

We developed a nickel (Ni) foam assisted pyrolysis method as a compelling approach to achieve larger grains for enhanced growth quality and to control the morphology of 3D graphene networks. Ni foam with large grain boundaries is a suitable template for 3D graphene growth due to its surface smoothness, porosity, and grain size. However, it is well known that controlling the number of graphene layers is very challenging via nickel assisted growth methods.

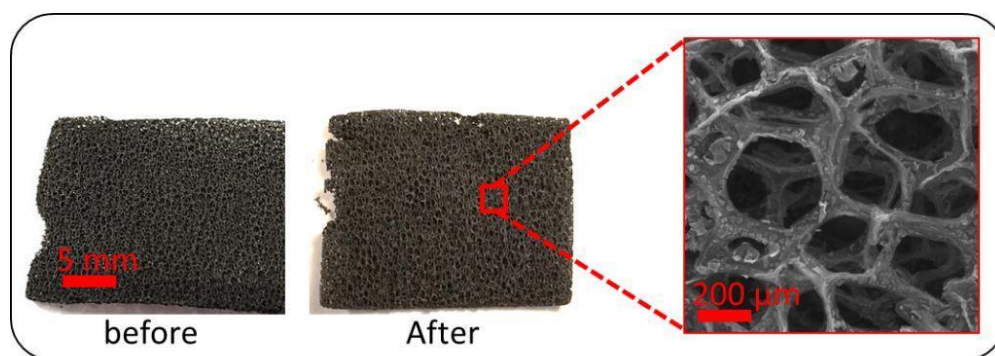


Figure 3.12 | A SEM Image of 3D Graphene After Etching Ni Foam with HCl 5M (Right) and Photographs of 3D graphene Samples Before and After Etching Ni foam (right).

Raman spectroscopy, both transmission and scanning types of electron microscopy, electron energy loss spectroscopy (EELS), and X-ray photoelectron spectroscopy (XPS) were utilized for a thorough characterization of the 3D graphene samples.

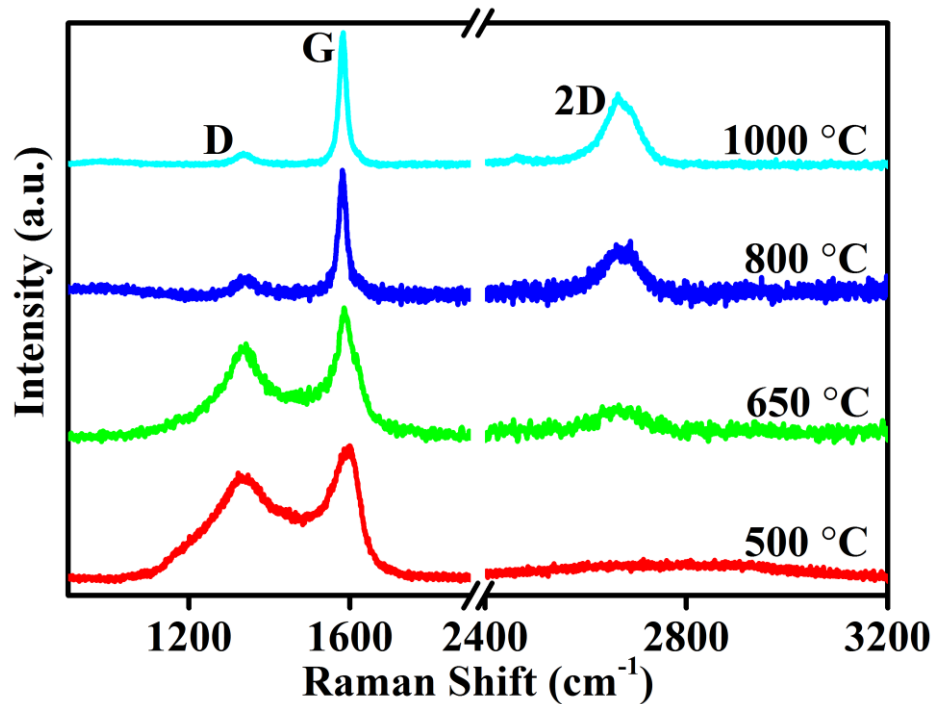


Figure 3.13 | A representative averages of obtained Raman spectra from 3D graphene foam grown at different temperatures.

Raman spectroscopy measurements were conducted for all 3D graphene samples prepared at various temperatures (500, 650, 800, and 1000 °C) to analyze the structural quality. A representative set of obtained spectra is presented in Figure 3.13. It can be seen that all samples have three prominent Raman peaks at $\sim 1,350\text{ cm}^{-1}$ (D band), $\sim 1,580\text{ cm}^{-1}$ (G band), and $\sim 2,700\text{ cm}^{-1}$ (2D band) which are characteristic to graphene Raman-active vibrational modes. It is well established that the D band, G band, and 2D band originate from defects, the in-plane vibration of sp^2 -hybridized carbon atoms, and second-order double resonant Raman, respectively [145-147]. The defects can be caused by vacancies, dislocations, edges, and cracks in graphene crystal structure. It is expected for 3D graphene samples to have more defect than a flat sheet of graphene and consequently more intense D bands. This is due to the substrate (Ni foam) surface with

many curvatures and edges, in contrast to conventional foil substrates. It is well known that Raman spectroscopy can reveal significant information about quality and number of graphene layers. Based on the Raman data of our samples (Figure 3.13), the intensity ratio of D and G bands (I_D/I_G) decreased by increasing the temperature and reached to the lowest value at 1000 °C. This trend is an indication of higher crystallinity structure with lower defect concentration. Moreover, the ratio of the intensity of 2D bands and G bands (I_{2D}/I_G) rose significantly by increasing the temperature and reached its highest values at 1000 °C. Trends in both intensity ratios indicated that the 3D graphene grown at a higher temperature has better overall structural quality, and less number of layers. The highest 3D graphene was achieved at around 1000 °C. From the Raman analysis of the graphene foam samples, the I_{2D}/I_G ratio showed a characteristic of few-layered graphene coatings. This was also verified by high-resolution TEM image of the graphene coating. In addition, the low-intensity Raman D bands ($\sim 1350\text{ cm}^{-1}$) of samples grown at 1000 °C in Figure 3.13 revealed a low defect density in the 3D graphene structure.

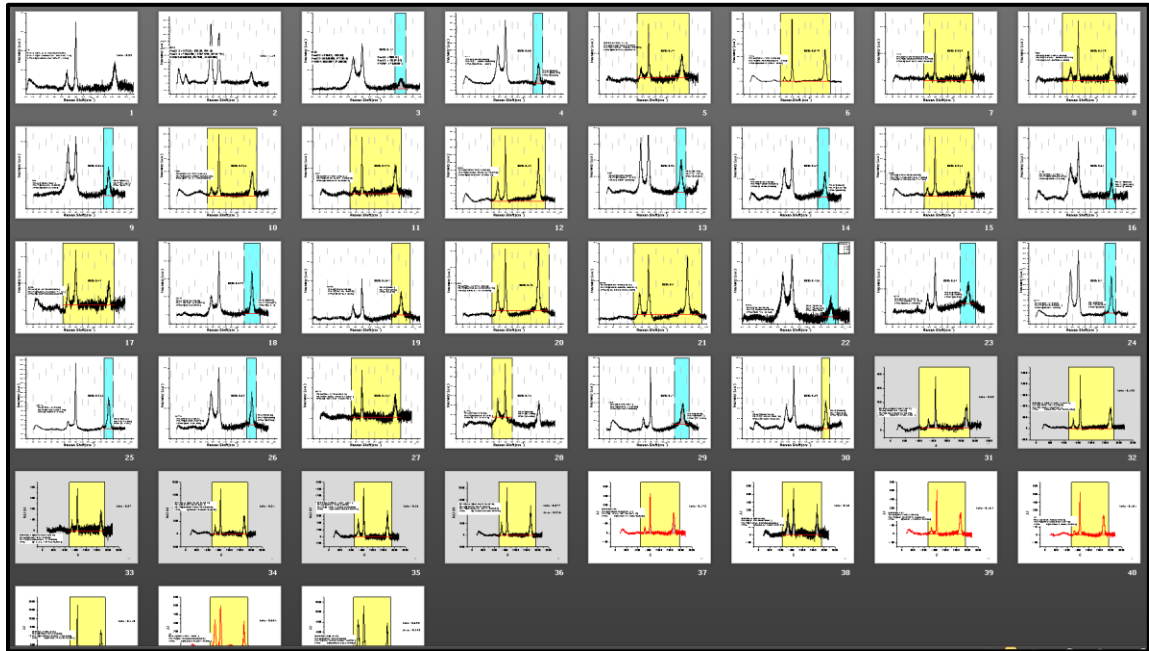
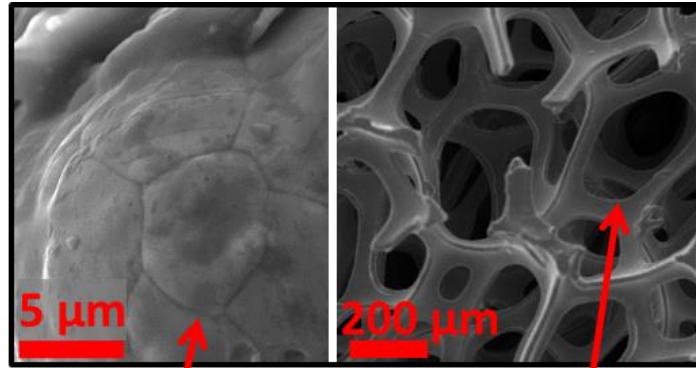


Figure 3.14 | Deconvolution of 3D graphene Raman peaks with a Lorentzian function to find FWHM, positions, and area under the peaks for statistical analysis.

	A	B	C	D	E	F	G	H	I	J	K	L	M	N	O	P	Q	R
1	T			X _D	X _G	X _{2D}	I _D	I _G	I _{2D}	FWHM _D	FWHM _G	FWHM _{2D}	I _D /I _G	I _{2D} /I _G	I _{2D} /I _D	W _D /W _G	W _{2D} /W _G	W _{2D} /W _D
2	650	6.24	1322.39	1588.36	2641.90	1708.32	1425.74	337.01	68.05	68.70	104.54	1.19	0.24	0.20	0.99	1.52	1.54	
3	650	10.38	1339.08	1583.03	2663.81	345.65	477.80	120.97	66.08	37.95	176.96	0.72	0.25	0.35	1.74	4.66	2.68	
4	650	18.64	1329.81	1582.14	2660.17	373.84	437.03	212.48	58.55	54.75	80.30	0.86	0.49	0.57	1.07	1.47	1.37	
5	650	22.81	1327.96	1568.79	2647.02	679.25	714.84	414.09	49.79	59.86	78.25	0.95	0.58	0.61	0.83	1.31	1.57	
6	650	30.108	1324.25	1584.80	2667.46	498.82	677.30	255.01	69.04	48.04	85.49	0.74	0.38	0.51	1.44	1.78	1.24	
7	800	3.13	1346.48	1580.36	2676.92	201.75	702.44	290.41	57.50	26.01	91.42	0.28	0.41	1.44	2.21	3.51	1.59	
8	800	7.29	1340.93	1582.14	2672.55	281.22	1403.01	596.68	60.48	25.96	101.42	0.20	0.43	2.12	2.33	3.91	1.68	
9	800	11.41	1332.59	1580.36	2663.81	1144.53	1889.77	635.31	62.96	44.65	77.65	0.60	0.34	0.56	1.41	1.74	1.23	
10	800	11.42	1345.55	1581.25	2676.92	101.97	419.75	198.13	52.25	26.42	96.51	0.24	0.47	1.94	1.98	3.65	1.85	
11	800	15.56	1329.81	1579.47	2670.37	101.94	443.96	181.21	78.45	25.96	84.69	0.23	0.41	1.78	3.02	3.26	1.08	
12	800	19.68	1324.25	1579.47	2664.54	155.62	999.31	398.64	90.14	24.11	98.38	0.16	0.40	2.56	3.74	4.08	1.09	
13	800	22.85	1331.67	1581.25	2666.73	311.23	575.66	264.61	74.80	37.86	82.62	0.54	0.46	0.85	1.98	2.18	1.10	
14	800	23.86	1349.25	1580.36	2676.92	147.40	959.47	401.30	71.74	25.54	110.41	0.15	0.42	2.72	2.81	4.32	1.54	
15	800	27.98	1324.25	1577.69	2669.64	98.25	223.08	111.44	54.63	30.33	87.36	0.44	0.50	1.13	1.80	2.88	1.60	
16	800	31.110	1334.45	1579.47	2669.64	162.38	472.49	271.66	57.95	29.77	83.76	0.34	0.57	1.67	1.95	2.81	1.45	
17	1000	12.44	1336.30	1584.80	2662.36	494.57	1253.77	552.67	61.85	28.68	75.01	0.39	0.44	1.12	2.16	2.62	1.21	
18	1000	12.45	1330.74	1579.47	2661.63	790.49	9986.95	5144.01	50.82	21.09	74.57	0.08	0.52	6.51	2.41	3.54	1.47	
19	1000	12.47	1340.93	1578.58	2672.55	61.86	381.93	218.49	105.19	21.46	86.16	0.16	0.57	3.53	4.90	4.01	0.82	
20	1000	20.71	1313.10	1579.47	2664.54	62.97	432.27	230.53	60.39	20.84	88.83	0.15	0.53	3.66	2.90	4.26	1.47	
21	1000	20.75	1329.81	1579.47	2662.36	531.73	1690.06	1128.90	68.21	27.91	69.02	0.31	0.67	2.12	2.44	2.47	1.01	
22	1000	24.88	1334.45	1582.14	2666.73	356.05	567.31	202.71	78.98	34.00	94.08	0.62	0.36	0.57	2.32	2.77	1.19	
23	1000	28.102	1331.67	1581.25	2663.09	219.65	705.86	490.38	58.84	25.98	68.46	0.31	0.69	2.23	2.26	2.64	1.16	
24	1000	28.103	1325.18	1580.36	2669.64	156.14	425.27	291.79	60.73	24.86	70.00	0.37	0.69	1.87	2.44	2.82	1.15	
25	1000	28.104	1334.45	1579.47	2661.63	383.17	824.73	829.84	45.77	34.44	50.38	0.46	1.01	2.17	1.33	1.46	1.10	
26	1000	28.105	1327.96	1578.58	2664.54	275.60	678.97	666.73	46.64	31.00	54.22	0.40	0.98	2.42	1.50	1.75	1.16	
27	1000	32.111	1321.46	1577.69	2653.60	1775.16	2530.64	1537.68	62.76	45.62	53.03	0.70	0.61	0.87	1.38	1.16	0.84	
28	1000	32.113	1334.45	1578.58	2664.54	381.19	2862.14	1401.15	46.98	21.74	74.01	0.13	0.49	3.68	2.16	3.40	1.58	
29	1000	32.116	1327.03	1579.47	2657.98	370.15	606.02	363.80	65.70	38.40	59.91	0.61	0.60	0.98	1.71	1.56	0.91	
30	1000	32.117	1334.45	1576.80	2675.46	121.05	479.18	245.98	21.65	23.14	87.00	0.25	0.51	2.03	0.94	3.76	4.02	
31	1000	32	1335.37	1577.69	2674.74	74.17	429.91	226.47	57.76	24.17	83.05	0.17	0.53	3.05	2.39	3.44	1.44	
32	1000	32	1314.03	1585.69	2659.44	291.52	576.93	383.83	83.78	40.58	52.81	0.50	0.67	1.32	2.06	1.30	0.63	
33	1000	32	1326.10	1579.47	2681.28	83.30	509.90	253.66	65.72	22.99	77.07	0.16	0.50	3.05	2.86	3.35	1.17	
34	1000	32	1331.67	1580.36	2673.28	53.97	533.77	245.21	92.19	24.58	87.09	0.10	0.46	4.54	3.75	3.54	0.94	
35	1000	32	1336.30	1579.47	2666.73	310.95	2818.89	1360.81	59.43	21.54	78.16	0.11	0.48	4.38	2.76	3.63	1.32	
36	1000	32	1326.10	1582.14	2659.44	336.47	505.61	328.80	76.61	50.50	57.29	0.67	0.65	0.98	1.52	1.13	0.75	
37	1000	32	1329.81	1581.25	2655.06	1618.11	2317.78	1436.99	68.56	54.25	51.97	0.70	0.62	0.89	1.26	0.96	0.76	
38	1000	32N	1332.53	1579.41	2684.86	84.88	385.57	186.84	57.23	21.23	76.81	0.22	0.48	2.20	2.70	3.62	1.34	
39	1000	32N	1328.82	1581.19	2682.68	477.89	2401.55	976.94	38.72	19.72	85.45	0.20	0.41	2.04	1.96	4.33	2.21	
40	1000	32N	1322.33	1579.41	2668.13	108.06	398.76	182.36	43.46	19.11	83.93	0.27	0.46	1.69	2.27	4.39	1.93	
41	1000	32N	1327.89	1581.19	2667.41	376.96	1752.54	723.56	35.36	20.83	72.03	0.21	0.41	1.92	1.70	3.46	2.04	
42	1000	32N	1329.75	1578.52	2659.39	524.79	1433.55	735.56	64.95	25.78	67.08	0.36	0.51	1.40	2.52	2.60	1.03	
43	1000	32N	1332.53	1581.19	2663.03	561.28	2024.36	1265.55	43.08	23.78	59.19	0.28	0.63	2.25	1.81	2.49	1.37	

Figure 3.15 | Raman spectral parameters of synthesized 3D graphene samples at different temperatures.



Lattice Grain Domain
(curvatures and
defects)

50-300 μm
Pore Size

Figure 3.16 | SEM images Show Morphology of a Ni Foam.

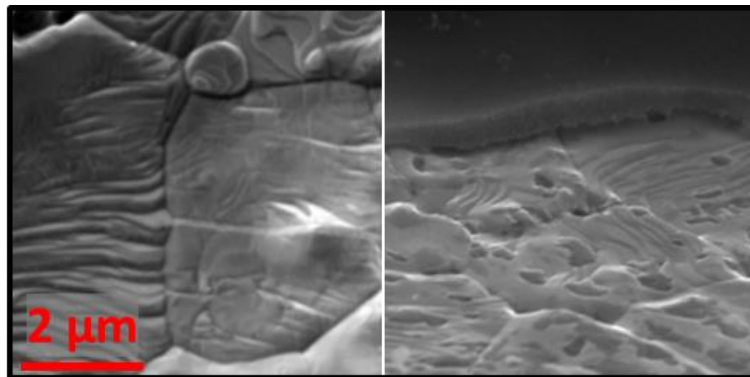


Figure 3.17 | After the Growth, Graphene Coat Has a Morphology Similar to the Morphology of the Substrate (Ni Foam).

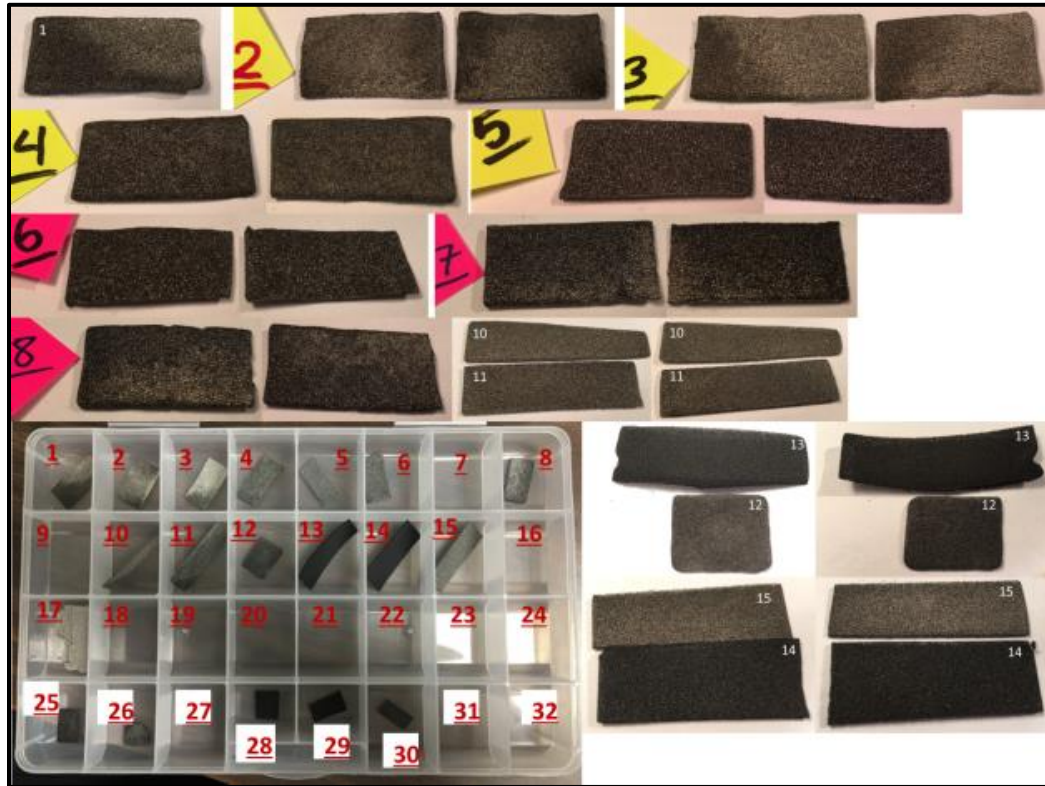


Figure 3.18 | Photograph of as-prepared 3D graphene foams synthesized under different growth conditions.

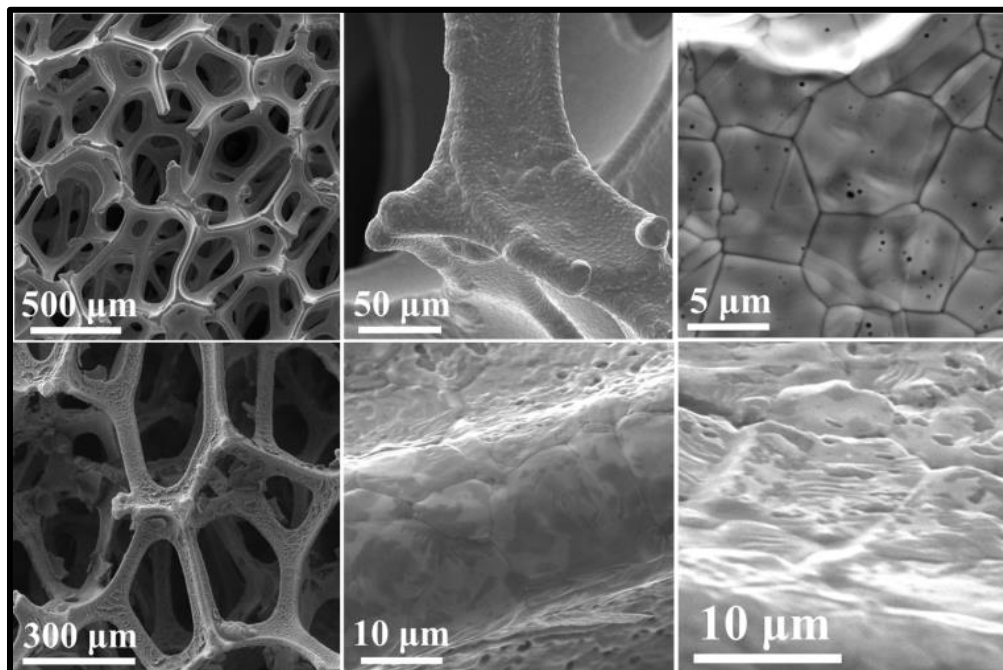


Figure 3.19 | Scanning Electron Microscopy (SEM) imaging of Ni foam before (top row) and after (bottom row) the graphene growth.

SEM images reveal (Figure 3.19 and 3.16) that the Nickel foam had a porous interconnected 3D network with a pore size of ~ 200 to ~ 300 μm in diameter. The TEM images further revealed that both nitrogen-doped and pure 3D graphene samples are consist of multilayer graphene. Figure 3.20 is a low-resolution TEM image of a graphene sheet with folded areas and indicated the growth of multi-layered graphene without the amorphous carbon. Furthermore, High-Resolution Transmission Electron Microscopy (HRTEM) revealed that graphene sheets containing 5–30 layers.

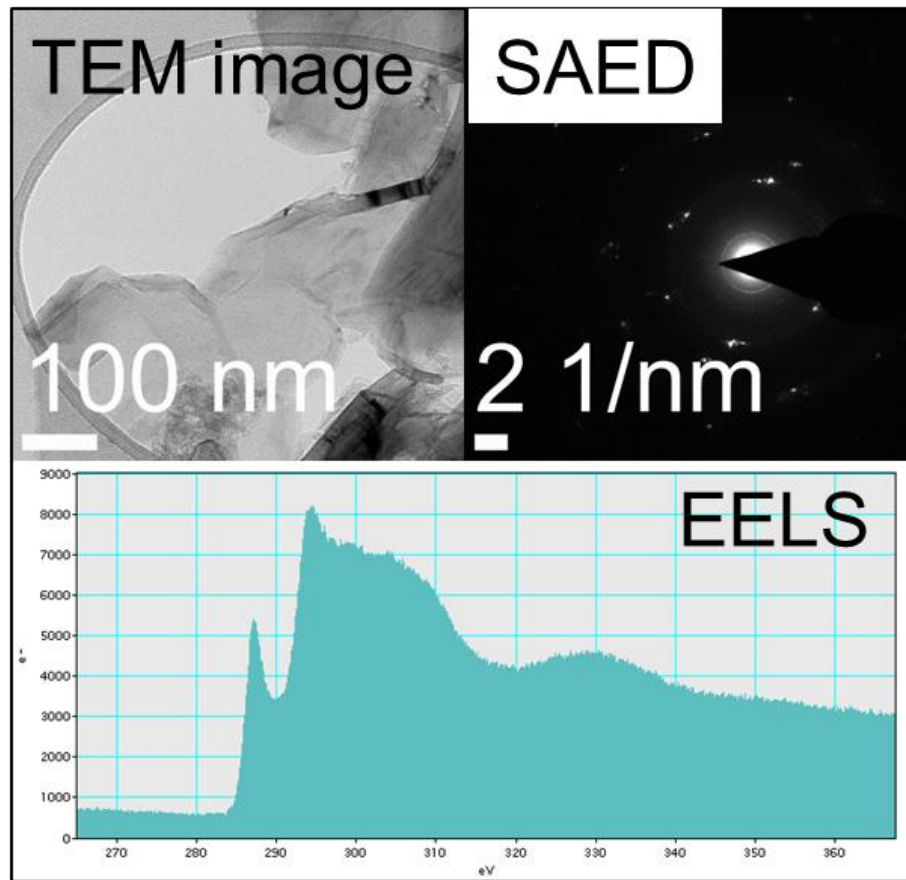


Figure 3.20 | a, Transmission Electron Microscopy (TEM) image, b, Selected Area Electron Diffraction (SAED) pattern, and c, Electron Energy Loss Spectroscopy (EELS) of pure 3D graphene foam prepared by pyrolysis of Citric Acid as the carbon source.

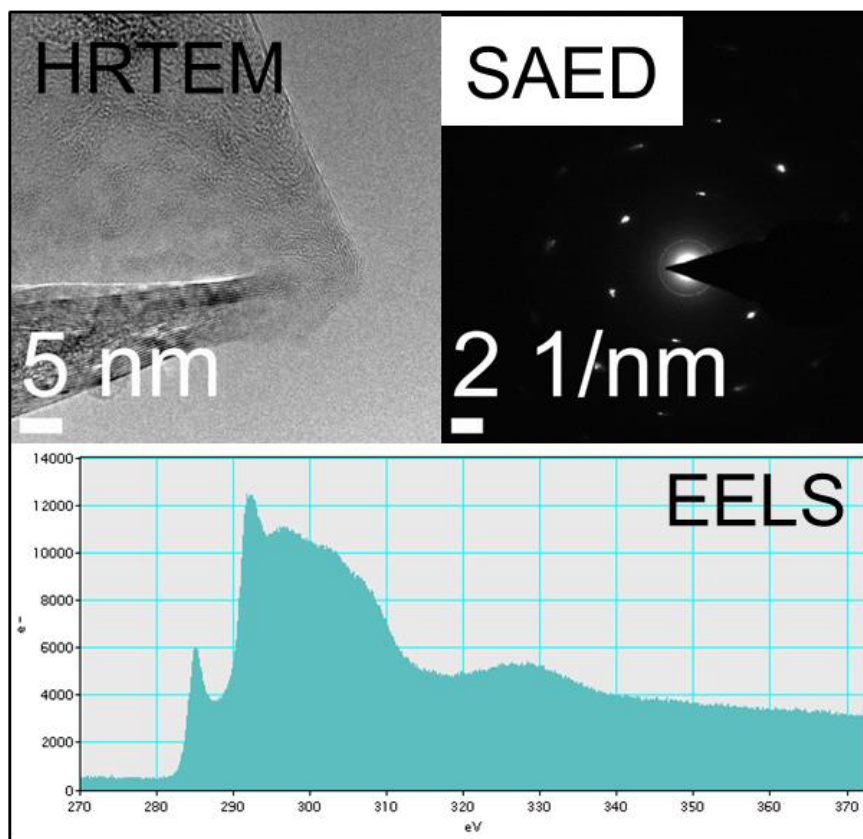


Figure 3.21 | a, Transmission Electron Microscopy (TEM) image, b, Selected Area Electron Diffraction (SAED) pattern, and c, Electron Energy Loss Spectroscopy (EELS) of Nitrogen-doped 3D graphene foam prepared by caffeine as the carbon source.

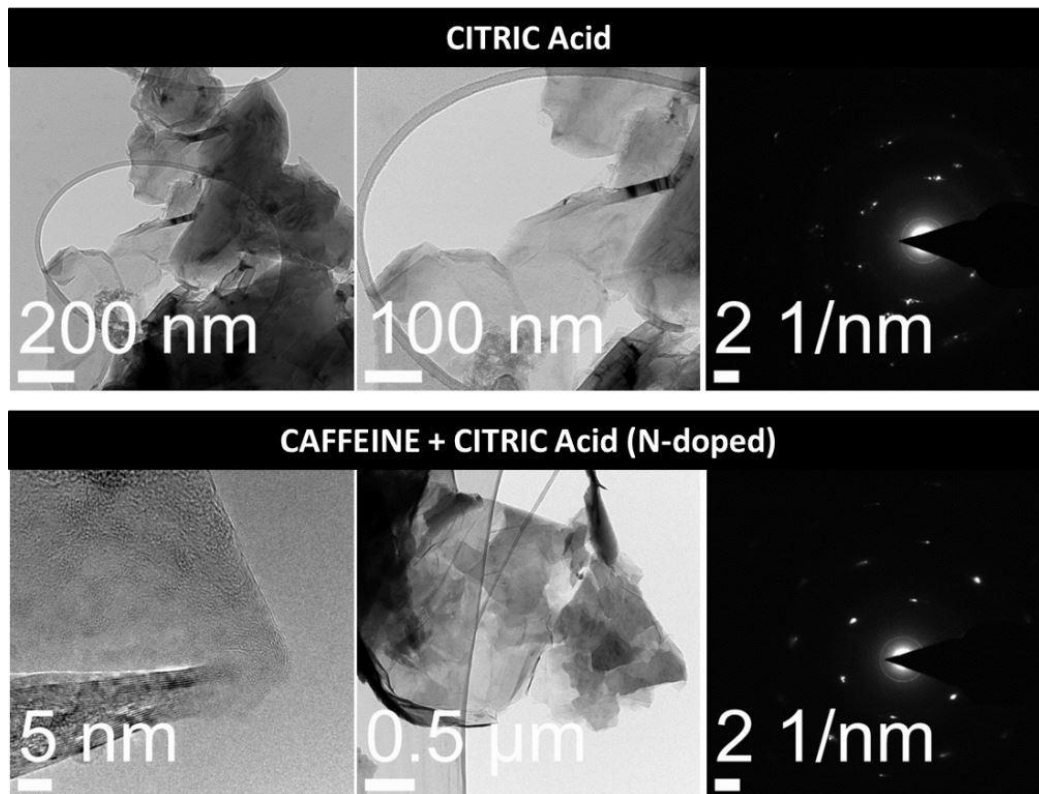


Figure 3.22 | TEM Analysis of Top: Pure 3D Graphene (precursor: Citric Acid) and Bottom: In Situ Nitrogen doped 3D Graphene (precursor: Citric Acid + Caffeine)

Furthermore, SAED pattern of the 3D graphene foam indicated the presence of nickel nanoparticles on top of the graphene layers, which resulted in the formation of nanocages on the surface of the graphene structure.

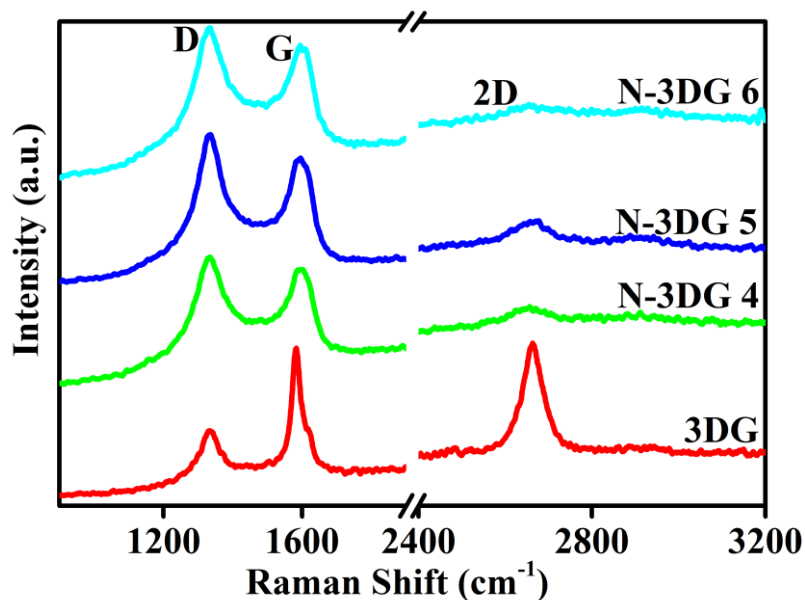


Figure 3.23 | Raman spectroscopy of nitrogen-doped 3D graphene foam (three upper spectra) and Raman spectrum of pure 3D graphene foam (red) all grown at 1000 °C.

Chemical compositions of the nitrogen-doped 3D graphene foams were investigated by X-ray Photoelectron Spectroscopy (XPS). Figures 3.25 and 3.26 are high-resolution XPS spectra for the sample synthesized at 1000 °C with urea and citric acid as the sources of carbon and nitrogen.

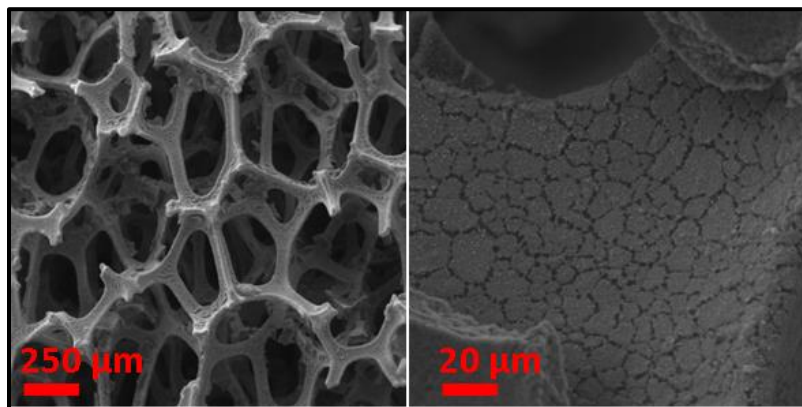


Figure 3.24 | SEM Images of a Nitrogen Doped Sample

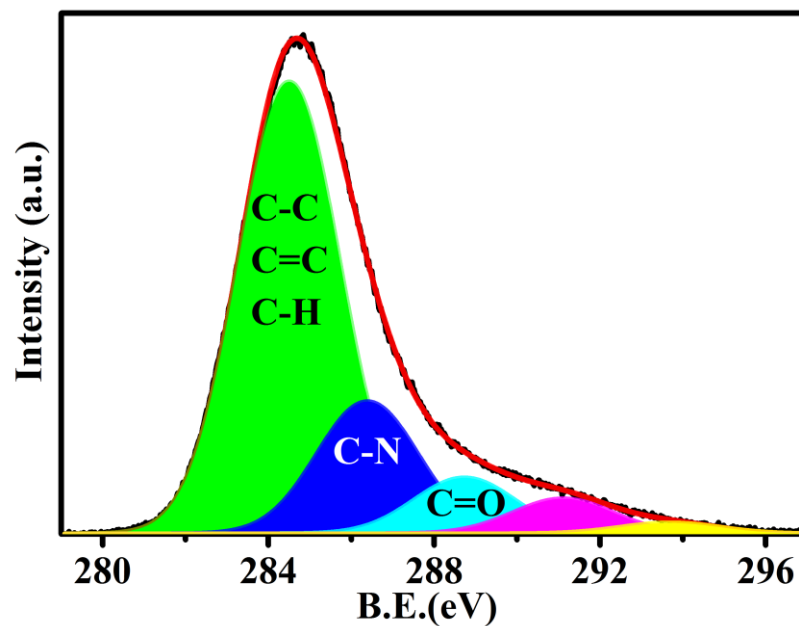


Figure 3.25 | Deconvoluted high-resolution C (1s) X-ray photoelectron spectroscopy (XPS) spectra of Nitrogen-doped 3D graphene foam using Urea as the carbon source.

A detailed analysis of XPS spectra [148,149] revealed the existence of some oxygen-containing functional groups in addition to the nitrogen on the 3D graphene foam surface. Moreover, deconvolutions of the spectra indicate components related to bound hydroxide groups (OH^-).

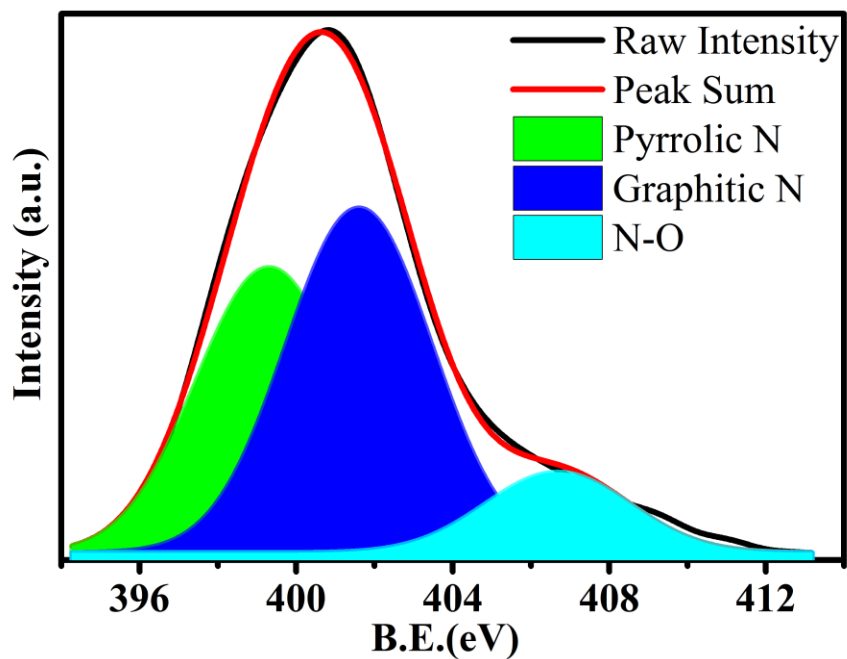


Figure 3.26 | Deconvoluted high-resolution N (1s) X-ray photoelectron spectroscopy (XPS) spectra of Nitrogen-doped 3D graphene foam prepared by Urea as the carbon source.

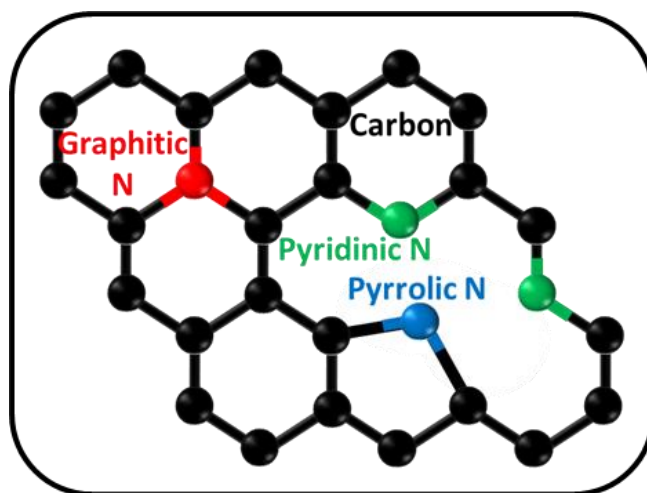


Figure 3.27 | nitrogen-bonding configurations in the nitrogen-doped carbon

The peak analysis of deconvoluted XPS curves indicated that about 3% nitrogen is incorporated into the graphene surface. Furthermore, electrochemical catalytic activity

testing³ to reduce CO₂ showed a significant increase in catalytic activity of Ni-doped carbon when 3D graphene network is used as the core-shell (CO₂ reduction to CO). Figure 3.28 shows a comparison of the catalytic activity of Nickel foam; three-dimensional graphene network on nickel foam, Carbon doped with Nitrogen (polyaniline) with core-shell of 3D graphene, and silver film. In the electrochemical testing Ag/AgCl (3.0 M KCl) was used as the reference electrode, Pt mesh as counter electrode and the sample as the working electrode. Moreover, the electrolyte was CO₂-saturated 0.1 M KHCO₃ and the CO₂ reduction products were measured by gas chromatography.

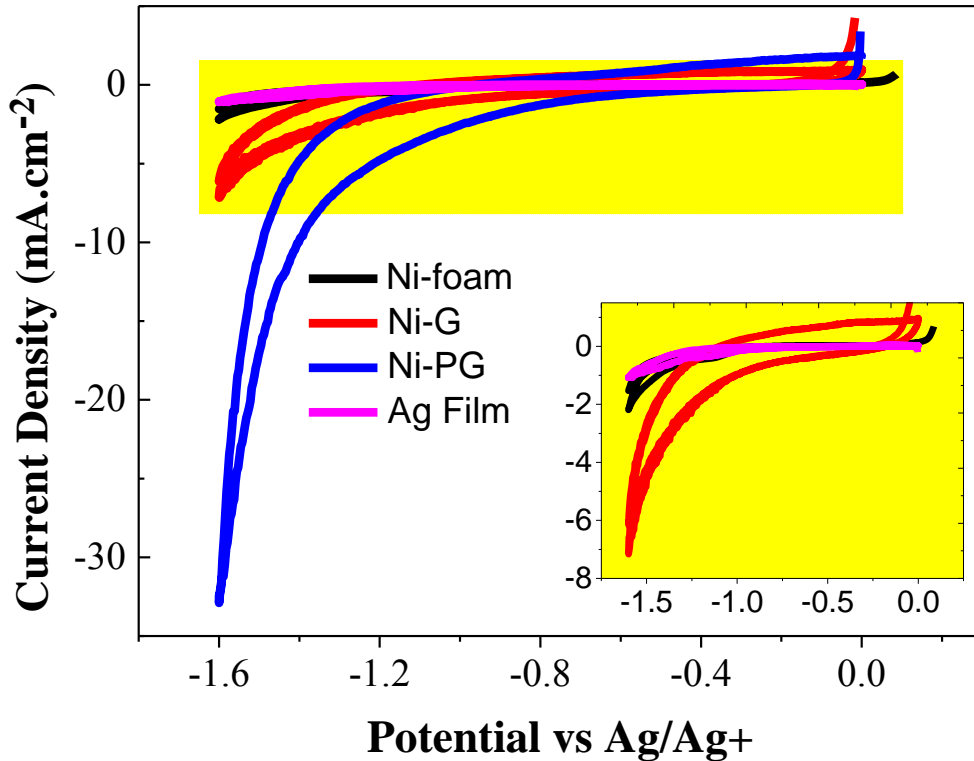


Figure 3.28 | Catalytic activity of Nickel foam, Three-dimensional graphene network on nickel foam (Ni-G), Carbon doped with Nitrogen (polyaniline) with core-shell of 3D graphene (Ni-PG), and Silver film (Ag Film).

³ Performed by Dr. Bijandra Kumar (Conn Center for Renewable Energy Research)

3.3 Phosphorene

The high-pressure evolution of Raman frequency of phosphorene (few-layer black phosphorus) from ambient pressure to ~14 GPa was collected at room temperature. High pressure was generated by a gas membrane driven “diamond anvil cell” (Diacell® HeliosDAC Almax easyLab) equipped with 800 μm culet diamonds. Inconel gasket with 10 mm in diameter and 0.20 mm thickness were pre-indented down to 0.05 mm. Micro Electrical discharge machining (EDM) (Hylozoic Products) was used for drilling a small hole (0.3 mm in diameter) for sample loading.

In-situ high-pressure Raman measurements were conducted at room temperature using the diamond anvil. Each sample was excited with He-Ne (633 nm) red laser in a 180° backscattering geometry using a Leica microscope with a 50X Nikon objective lens (T Plan EPI SLWD, Working Distance = 22 mm). Renishaw inVia spectrometer with a 1800 lines per millimeter grating, and equipped with a CCD detector, was used for Raman spectroscopy. The Raman spectra were collected at various pressures during compression and decompression.

Ruby fluorescence R2-line shifts were used for pressure calibration. This method is known to have an error of $\pm 5\%$. The ruby fluorescence was measured with same Renishaw spectrometer and He-Cd (442 nm) blue laser (IK series, Kimmon Koha Co.) during compression and decompression.

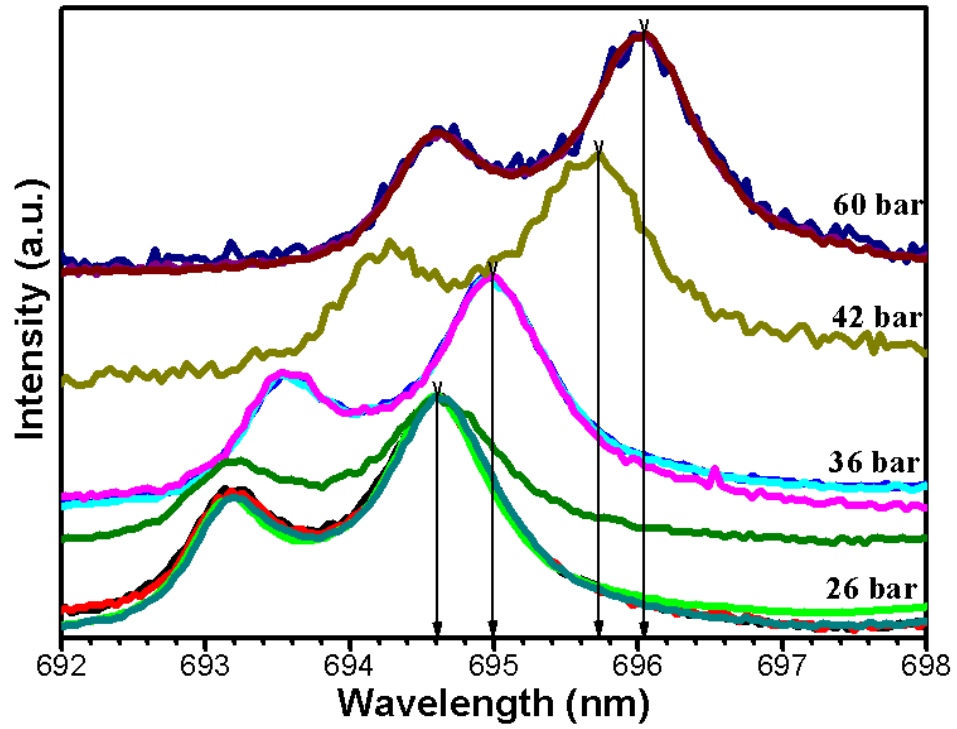


Figure 3.29 | Ruby fluorescence spectra at different gas membrane pressures (measured by gas controller unit). These pressures correspond to the actual pressures inside the DAC.

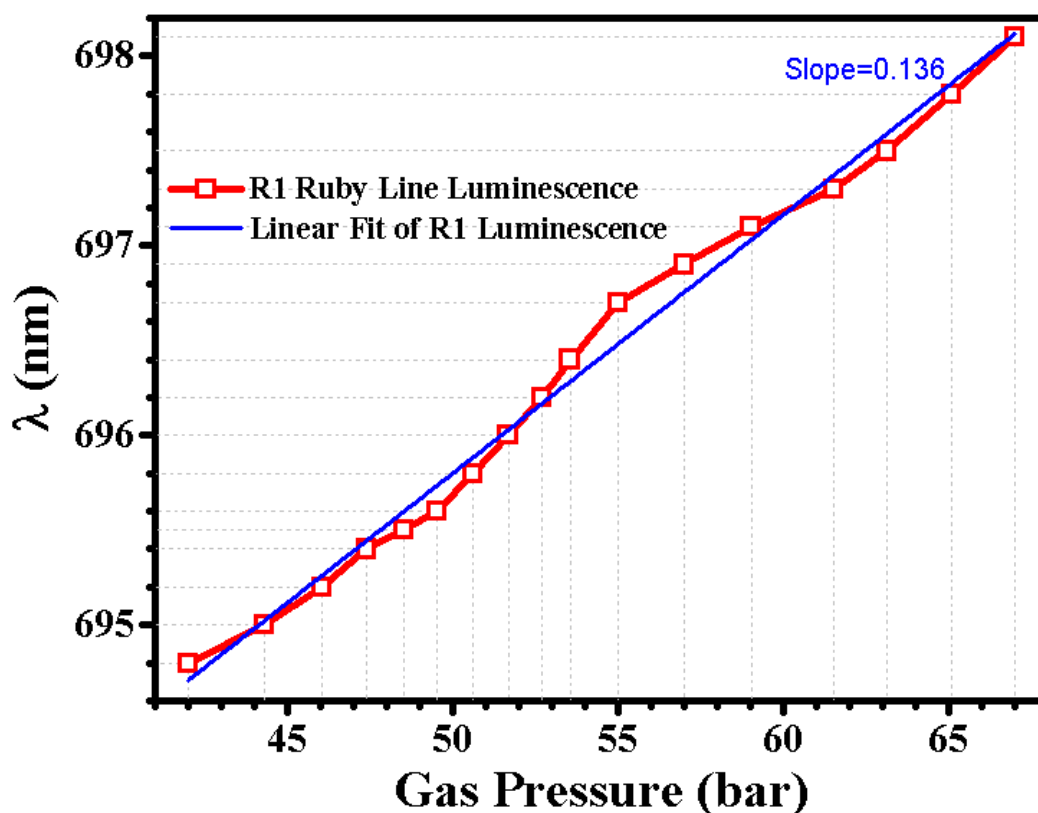


Figure 3.30 | The ruby fluorescence R2 line peak position as a function of pressure inside the gas membrane (measured by gas controller unit).

The pressure of gas membrane (which drive the piston of the cell) was calibrated against the pressure inside the DAC. For each high-pressure experiment, small pieces of phosphorene samples were loaded into the gasket hole under an optical microscope (AmScope Trinocular Stereo Zoom) with long working distance objective lenses. It was visually ensured that the phosphorene samples were floating in the middle of the hole and were not in contact with the gasket or the diamond. We tested two solutions Methanol:Ethanol:DI-water (16:4:1) and Dimethylformamide (DMF) separately as the hydrostatic pressure media. The transparency of diamonds to the broad range of electromagnetic waves allows us to perform a series of *in-situ* high-pressure

measurement including precise pressure calibration from ruby photoluminescence R2 line, and Raman spectroscopy that resulted in the observation of phase transition in multilayered BP at high pressures.

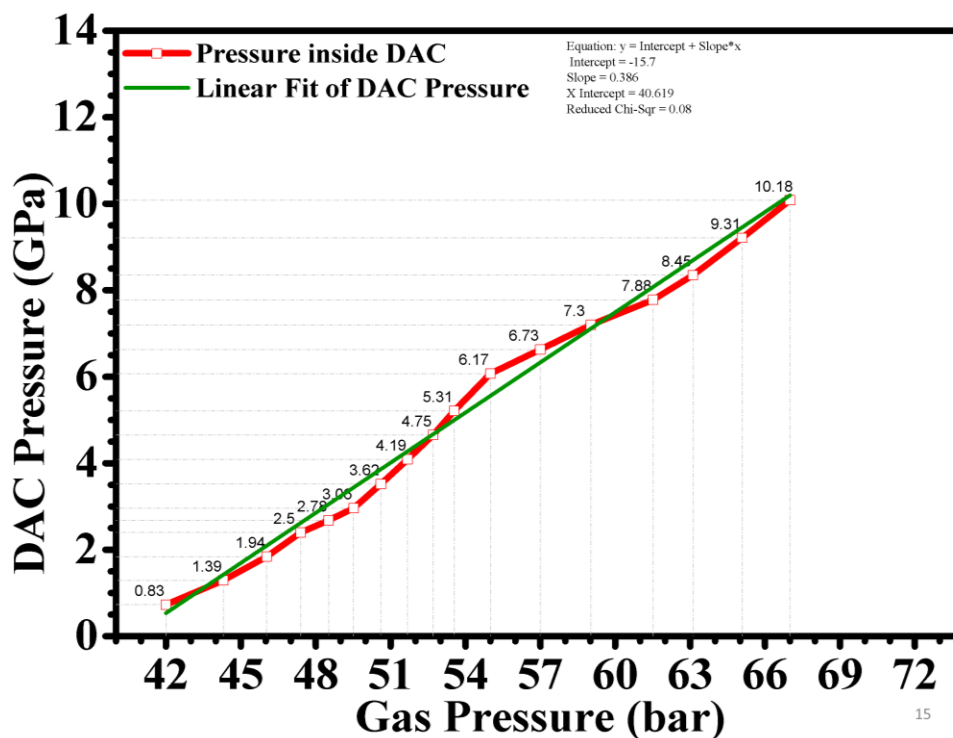


Figure 3.31 | Pressure inside the diamond anvil cell as a function of gas membrane pressure.

The Raman spectra at ambient pressure of few layer black phosphorus samples are shown in Figure 3.32. The prominent Raman spectrum peaks at 360 cm^{-1} , 440 cm^{-1} , and 468 cm^{-1} which were assigned to the A_g^1 (out-of-plane), B_{2g} (in-plane along the zigzag direction), and A_g^2 (in-plane along the armchair direction) vibrational modes respectively [150-152]. It has been known that both the bulk BP and phosphorene show these three Raman peaks which suggesting that black phosphorus stays crystalline after the exfoliation process [150,153-156].

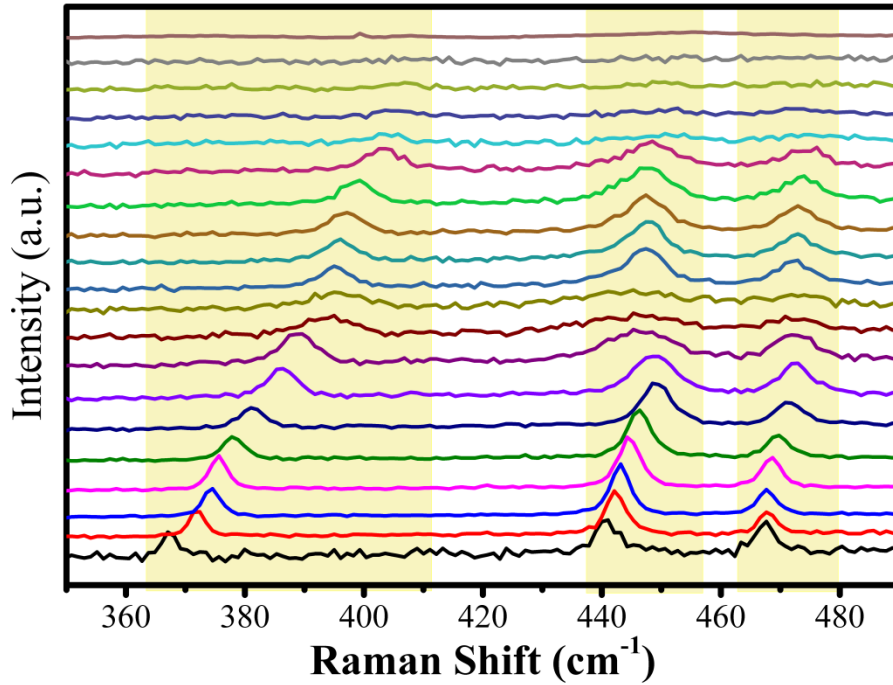


Figure 3.32 | Raman spectra of a few-layer black phosphorus (sample no. 1) under pressure range of 0 GPa (bottom spectrum) to 13.4 GPa (top spectrum) with vertical displacements for clarity.

As shown in Figure 3.32 and Figure 3.33, with the increase in pressure, all phonon modes shift towards higher frequencies (blue shift) with gradually decreasing intensity. The frequencies of Raman modes of a few-layer BP sample as a function of applied hydrostatic pressure are shown in Figure 3.34. The application of pressure was found to modify the vibrational properties of few-layer black phosphorus strongly.

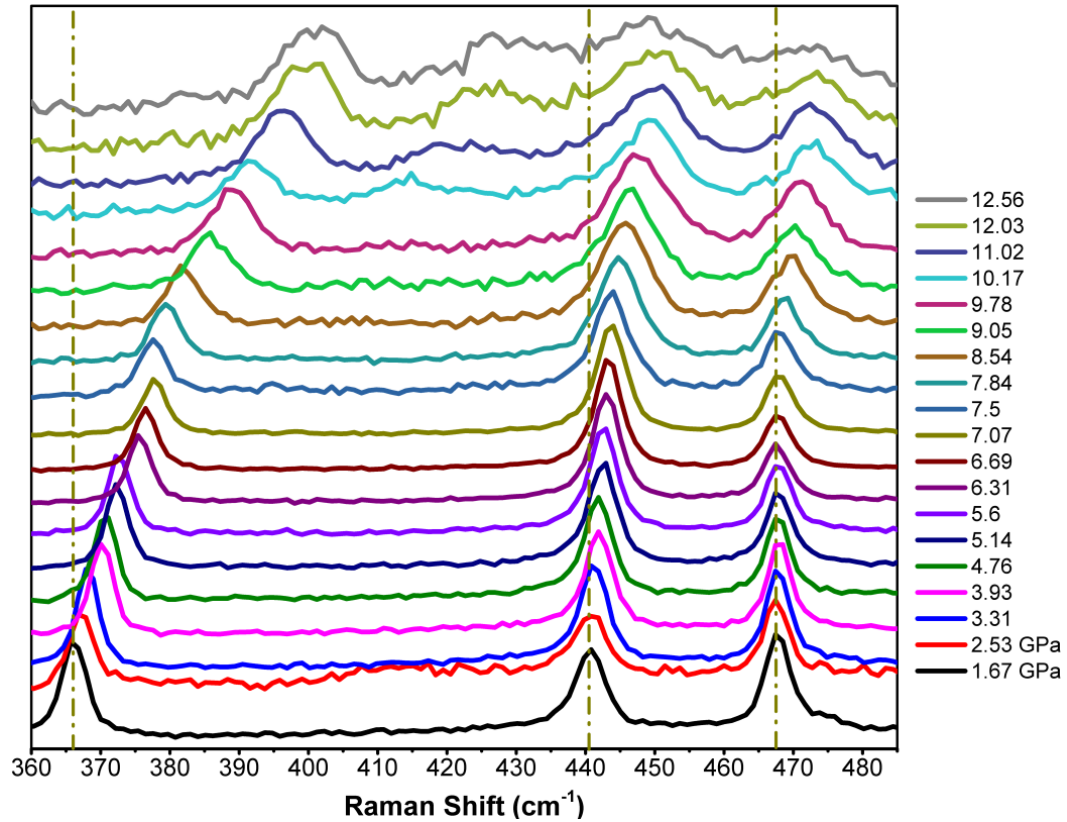


Figure 3.33 | Raman spectra of a few-layer black phosphorus under pressure range of 0 GPa (bottom spectrum) to 12.56 GPa (top spectrum) with vertical displacements for clarity.

The crystal structure of bulk black phosphorus at normal conditions is orthorhombic (*A11*) and belongs to the space group *Cmce* (No. 64) and point group $D_{2h}^{18}(mmm)$ [153,157]. It has been known that the bulk black phosphorus orthorhombic (*A11*) crystal structure exhibits a sequence of transitions under high pressure. First, at ~5.2 GPa black phosphorus transforms from the orthorhombic to the rhombohedral (*A7*) crystal phase with 10% reduction in volume and then with 3.7% volume reduction at ~10 GPa it transforms to the simple-cubic structure [153]. The rhombohedral BP is a semimetal and, simple-cubic BP is a metallic material and shows superconductivity at low temperature

[61-63]. Bulk BP with orthorhombic crystal phase has eight atoms in a unit cell, which half of them (four) are in the primitive unit cell. Therefore, it has 12 vibrational (phonon) modes at the Γ point in the Brillouin zone [157]:

$$\Gamma_{\text{Bulk}} = 2A_g + B_{1g} + B_{2g} + 2B_{3g} + A_{1u} + 2B_{1u} + 2B_{2u} + B_{3u}$$

which consist of five Raman-active (A_g^1 , A_g^2 , B_{1g} , B_{2g} , and B_{3g}), three infrared-active (B_{1u} , B_{2u} , and B_{3u}), one silent (A_u), and three acoustic (A_{1u} , B_{1u} , and B_{2u}) phonon modes.

The rhombohedral (A7) lattice with two atoms per primitive unit cell has three Raman active modes at zone-center, that is, one A_{1g} mode and a two-fold degenerate E_g mode.

According to the classical Placzek approximation [157-160], the Raman intensity of a phonon mode is proportional to $|e_i \cdot \tilde{R} \cdot e_s^T|^2$ where e_i and e_s are the electric polarization vectors of the incident laser and scattered light, respectively, and \tilde{R} is the Raman tensor of the phonon mode. Phonon modes can be observed by Raman spectroscopy only when $|e_i \cdot \tilde{R} \cdot e_s^T|^2$ is not zero. By denoting the zigzag and armchair directions as the x- and z-axis, and the out-of-plane direction as the y-axis, the calculated (via the group theory analysis) Raman tensors \tilde{R} of A_g , B_{1g} , B_{2g} , and B_{3g} modes are [158]:

$$\begin{aligned} \tilde{R}(A_g) &= \begin{pmatrix} a & 0 & 0 \\ 0 & b & 0 \\ 0 & 0 & c \end{pmatrix} & \tilde{R}(B_{1g}) &= \begin{pmatrix} 0 & d & 0 \\ d & 0 & 0 \\ 0 & 0 & 0 \end{pmatrix} \\ \tilde{R}(B_{2g}) &= \begin{pmatrix} 0 & 0 & e \\ 0 & 0 & 0 \\ e & 0 & 0 \end{pmatrix} & \tilde{R}(B_{3g}) &= \begin{pmatrix} 0 & 0 & 0 \\ 0 & 0 & f \\ 0 & f & 0 \end{pmatrix} \end{aligned}$$

Where $a - f$ are non-zero terms while other terms are either zero or negligible due to symmetry. In the typical experimental back-scattering laser geometry (y in and y out for the laser), the electric polarization vectors of the incident and scattered light e_i and e_s are in-plane (the x-z plane) in other words, direction of incident laser beam is perpendicular to the layers plane of BP sample. By setting the polarization angle of the incident (scattered) light as θ (γ) with respect to the x-axis, we have $e_i = (\cos \theta, 0, \sin \theta)$ and $e_s = (\cos \gamma, 0, \sin \gamma)$. For Raman intensity, we have:

$$I \propto |e_i \cdot \tilde{R} \cdot e_s^T|^2$$

By substituting e_i and e_s we have:

$$I \propto \left| (\cos \theta, 0, \sin \theta) \tilde{R} \begin{pmatrix} \cos \gamma \\ 0 \\ \sin \gamma \end{pmatrix} \right|^2$$

By applying the obtained forms of Raman tensor of each mode, we can get the Raman intensities for each mode:

$$I_{A_g} \propto a^2 \left| \cos \theta \cos \gamma + \frac{c}{a} \sin \theta \sin \gamma \right|^2$$

$$I_{B_{2g}} \propto e^2 \sin^2(\theta + \gamma)$$

$$I_{B_{1g}} = I_{B_{3g}} = 0$$

Therefore, B_{1g} and B_{3g} cannot be observed, and only A_g and B_{2g} modes can be observed. Furthermore, the symmetries of N-layer (NL) BP (where N is the number of layers) are slightly different from those of bulk BP. Odd NL BP belongs to space group Pmna (No. 53) and point group $D_{2h}^7(mmm)$; even NL BP belongs to space group Pmca

(No. 57) and point group $D_{2h}^{11}(mmm)$. Although NL systems belong to different space groups from the bulk BP, all of them share the same point group $D_{2h}(mmm)$.

Consequently, the symmetry classification of Raman modes and the forms of their Raman tensors remain unchanged for any thickness [157].

Bulk BP at normal pressure:

Crystal structure	Orthorhombic (A11)
Space group	Cmce (No. 64)
Point group	D_{2h}^{18}
Number of atoms in primitive unit cell	4 atoms
$\Gamma_{\text{Bulk}} = 2A_g + B_{1g} + B_{2g} + 2B_{3g} + A_{1u} + 2B_{1u} + 2B_{2u} + B_{3u}$	
Raman active modes	$2A_g + B_{1g} + B_{2g} + 2B_{3g}$
Infrared (IR) active modes	$B_{1u} + B_{2u}$
Acoustic modes	$B_{1u} + B_{2u} + B_{3u}$
Silent mode	A_{1u}

Few-layer BP at normal pressure:

- a) With (AA or AB stacking, and odd # of layers) or (AA stacking, and even # of layers):

Space group	Pmna (No. 53)
Point group	$D_{2h}^7(mmm)$

$$\Gamma = 2N (A_g + B_{2g} + B_{1u} + B_{3u}) + N (B_{1g} + B_{3g} + A_{1u} + B_{2u})$$

Raman active modes	$2N (A_g + B_{2g}) + N (B_{1g} + B_{3g})$
--------------------	---

Infrared (IR) active modes	$(2N-1) (B_{1u} + B_{3u}) + (2N-1) B_{2u}$
----------------------------	--

Acoustic modes	$B_{1u} + B_{2u} + B_{3u}$
----------------	----------------------------

Silent modes	NA_{1u}
--------------	-----------

b) With AB stacking, and even # of layers:

Space group	Pmca (No. 57)
-------------	---------------

Point group	D_{2h}^{11}
-------------	---------------

$$\Gamma = 2N (A_g + B_{2g} + B_{1u} + B_{3u}) + N (B_{1g} + B_{3g} + A_{1u} + B_{2u})$$

Raman active modes	$2N (A_g + B_{2g}) + N (B_{1g} + B_{3g})$
--------------------	---

Infrared (IR) active modes	$(2N-1) (B_{1u} + B_{3u}) + (2N-1) B_{2u}$
----------------------------	--

Acoustic modes	$B_{1u} + B_{2u} + B_{3u}$
----------------	----------------------------

Silent modes	NA_{1u}
--------------	-----------

Bulk BP at a pressure range of ~4.5 to ~10 GPa:

Crystal structure	Rhombohedral (A7)
-------------------	-------------------

Space group	$R\bar{3}m$ (No. 166)
-------------	-----------------------

Point group	D_{3d}^5
Number of atoms in primitive unit cell	2 atoms
Γ_{Bulk} (Rhombohedral)	$3(A_g + E_g + B_{1u} + B_{2u})$
Raman active modes	$3(A_g + E_g)$
Infrared (IR) active modes	$2(B_{1u} + B_{2u})$
Acoustic modes	$B_{1u} + B_{2u}$
Silent mode	None

Bulk BP at a pressure above 10 GPa:

Crystal structure	Simple cubic
Space group	$Pm\bar{3}m$
Point group	O_h^1
Number of atoms in primitive unit cell	1 atom
Γ_{Bulk} (SC)	Non

It is well known that inducing pressure in phosphorene results in an increase in the Raman shift similar to other layered materials [161-164]. Analyses of the high-pressure Raman spectra reveal three distinct regions (Figures 3.35 - 3.37) of pressure. Up to 6.5 GPa the A_g^1 mode showed a linear increase with a large coefficient of $5.78 \text{ (cm}^{-1}\text{) (GPa)}^{-1}$. The B_{2g} mode initially increases by 3 cm^{-1} and saturates above 2 GPa. The A_g^2 mode does not show any significant pressure dependence. Upon further compression, we observed that the shifts in the Raman modes above ~ 6.5 GPa are unambiguously different than that

of the orthorhombic phase which was interpreted as a phase transition from orthorhombic to rhombohedral crystal structure. At high pressures above 10 GPa, a new phonon modes appear at $\sim 425 \text{ cm}^{-1}$ in the Raman spectra. This change can be associated to occurrence of a phase transition from orthorhombic to simple cubic in few layer black phosphorus. With further increase of the pressure above $\sim 14 \text{ GPa}$, the vibrational Raman modes were found to disappear. These spectral changes under high pressure can be due to non-hydrostatic behavior of DMF at that pressure. Upon decompression, the spectroscopic changes are reversible and the high-pressure phase reverts to the original structure.

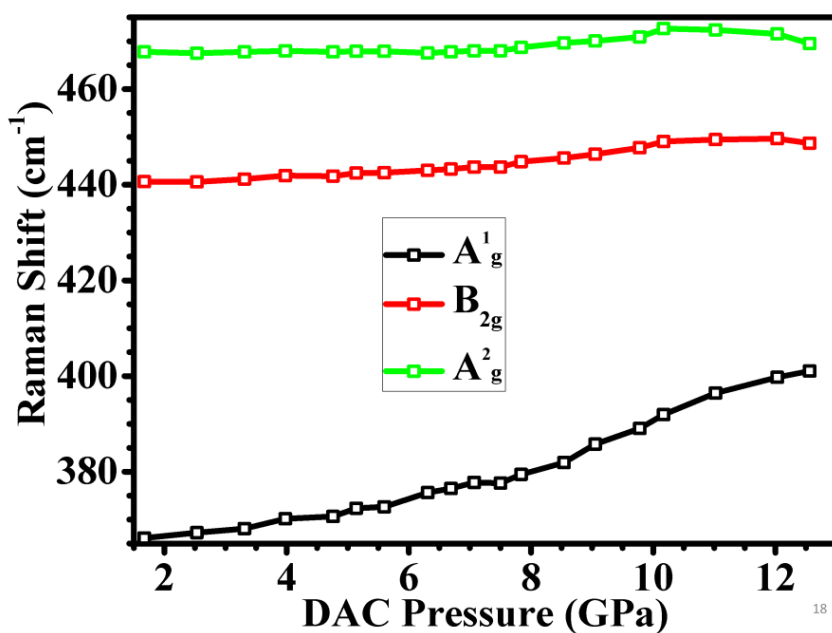


Figure 3.34 | Raman shift of three prominent peaks of phosphorene as a function of pressure.

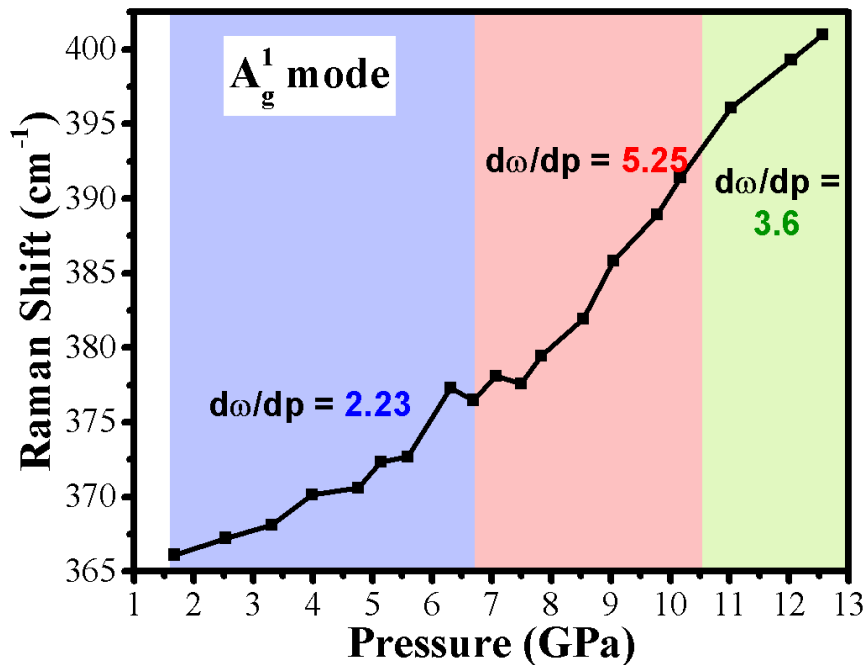


Figure 3.35 | Raman A_{1g} peak position of phosphorene vs. pressure (red) and its linear fit (black)

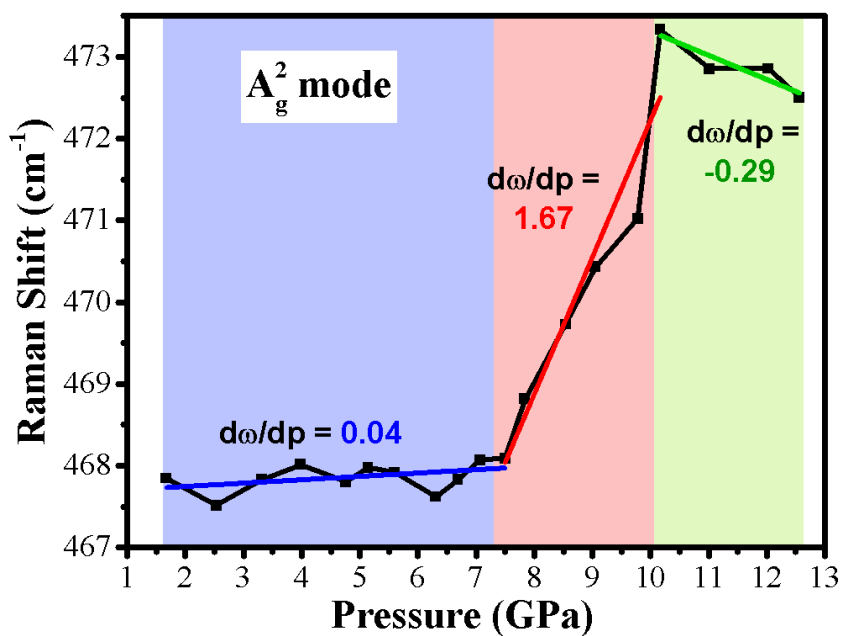


Figure 3.36 | Raman shift of A_{2g} mode of phosphorene vs. pressure (blue) and its linear fit (black)

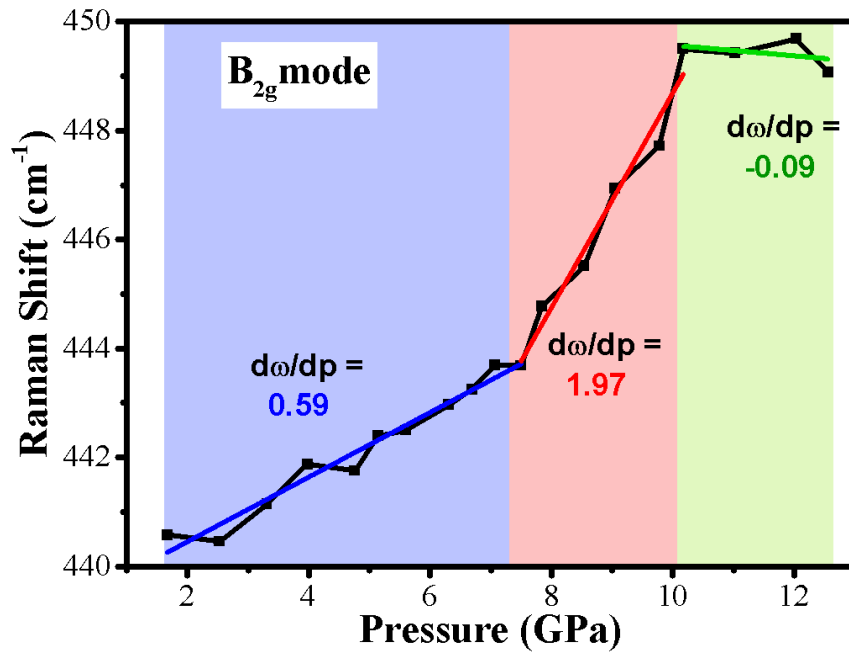


Figure 3.37 | Raman shift of B_{2g} mode of phosphorene vs. pressure (green) and its linear fit (black)

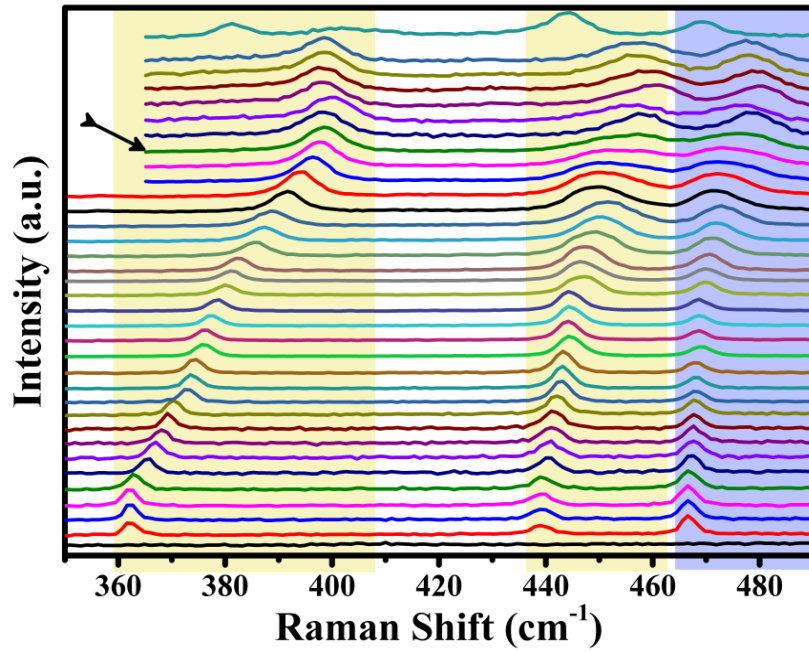


Figure 3.38 | Raman shift of a full pressure cycle of phosphorene from normal pressure (bottom spectrum) to 13 GPa (indicated by the arrow) and returning to ambient pressure (upper one).

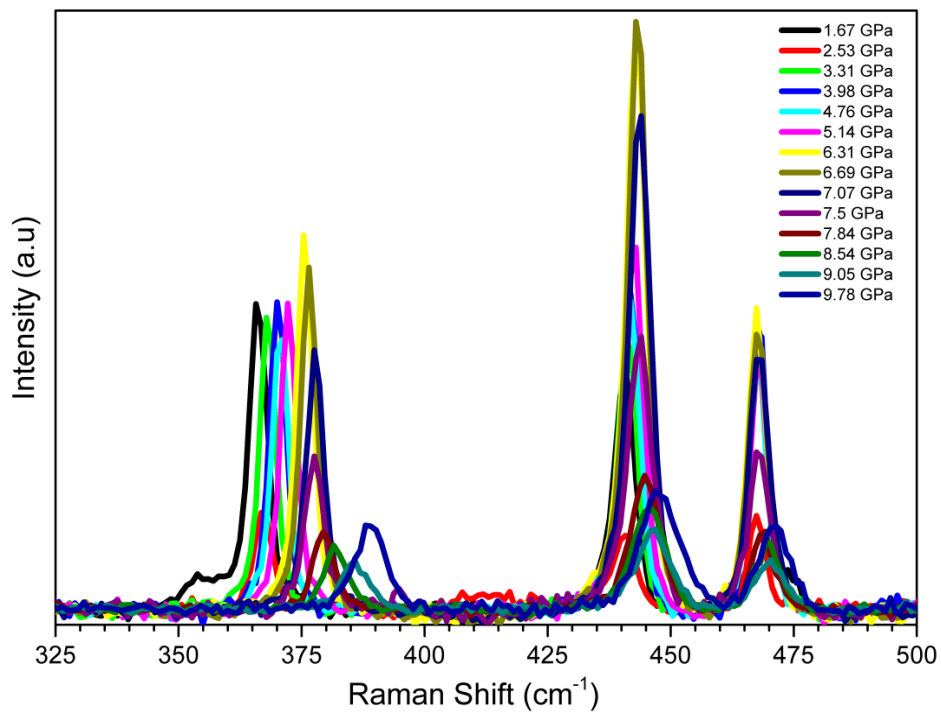


Figure 3.39 | Normalized Raman spectra of phosphorene vs. pressure

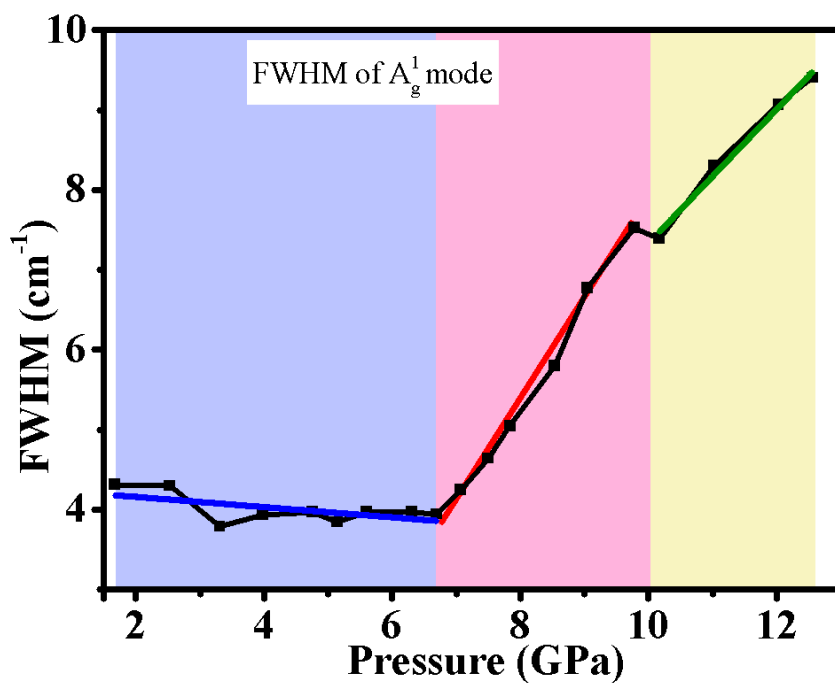


Figure 3.40 | Full-Width Half Maximum (FWHM) of A_{1g} Raman mode as a function of the pressure.

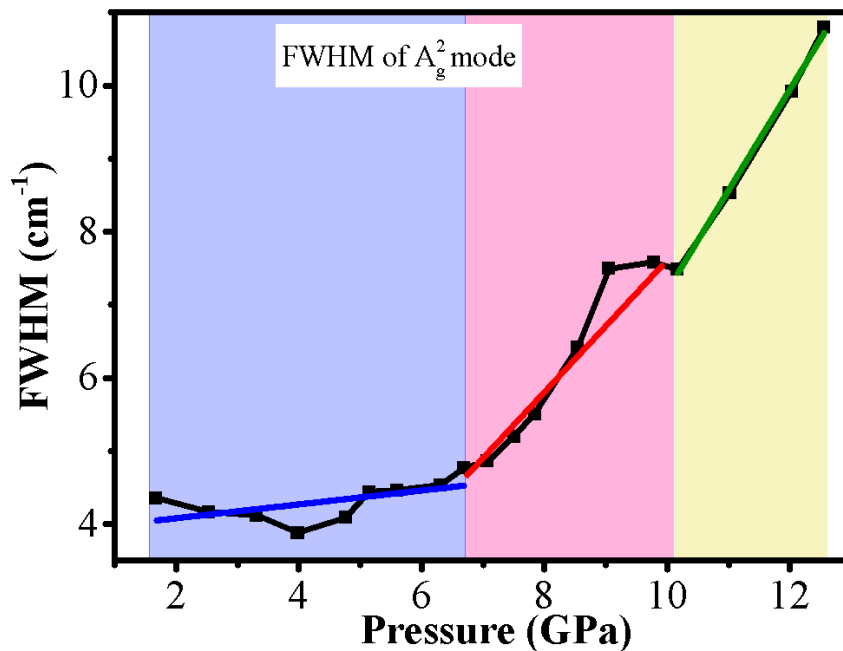


Figure 3.41 | Full-Width Half Maximum (FWHM) of A_{2g} Raman mode as a function of the pressure.

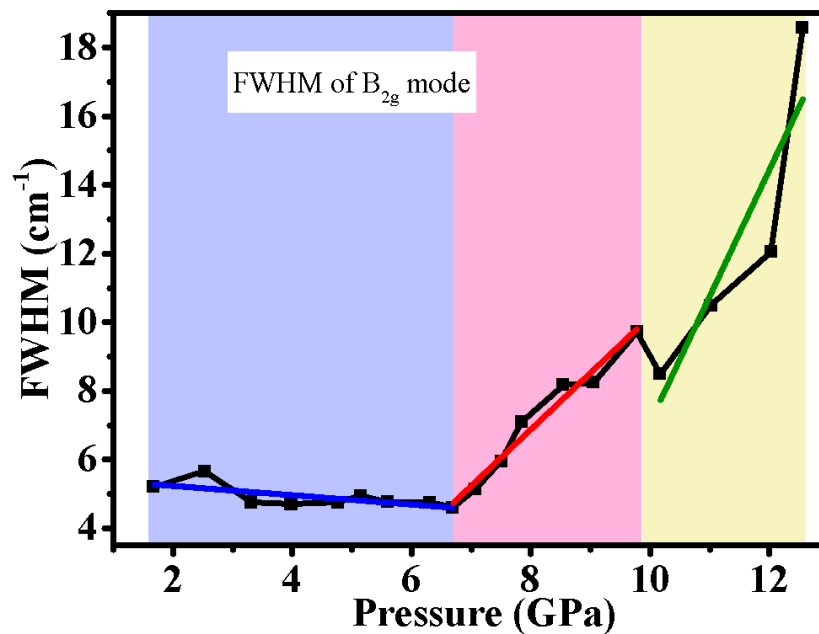


Figure 3.42 | Full-Width Half Maximum (FWHM) of B_{2g} Raman mode as a function of the pressure.

These results emphasize the prominent role of pressure in modifying the vibrational and electronic properties of two-dimensional systems. In conclusion, the group theory analysis along with the experimental Raman measurements indicated the pressure-induced structural phase transitions in few-layer BP. High-pressure Raman results suggest existence of two pressure-induced structural phase transitions in few-layer BP samples, which is drastically different from the transformation sequence of bulk BP.

CHAPTER 4: SUMMARY AND OUTLOOK

The synthesis of materials under high pressure is a vast area of physics, chemistry, and engineering. High-pressure technology is frequently being used in materials science to improve the electronic and atomic structure of materials and tune various materials properties. Besides, it is also being used in solid-state chemistry to modify existing materials and to synthesize non-equilibrium phases or novel compounds. High pressure can severely reduce the inter-atomic volume and result in densification effects or enhancement of the reactivity. One of the advantages of high-pressure approaches in synthesis chemicals is the fact that these are in general cleaner and faster technique than purely chemical routes, which normally leads to the formation of by-products, or results in undesired disorder or phase separation.

Encouraged by advantageous of high-pressure synthesis method, we designed and demonstrated the successful synthesis of α -AgGaO₂ for the first time via solid-state reaction. In this project, high pressure was used to stabilize Ag₂O and to drive a direct synthesis of rhombohedral silver gallium oxide (AgGaO₂) through a solid-state reaction between Ag₂O and Ga₂O₃ powders. The instability of silver oxide under the normal conditions imposes considerable challenges for the preparation of silver-gallium oxide compound. As Ag₂O decomposes in air at a temperature of ~ 300 °C, it is challenging to synthesize AgGaO₂ in a one-step via a conventional solid-state reaction technique in an open system. Synthesis conditions of high temperature and, more importantly, of high

pressure was essential to facilitate the synthesis reaction. A thorough characterization of the synthesized sample was performed, and the rhombohedral crystal phase was identified explicitly. Furthermore, vibrational phonon modes analysis indicates good agreement between theoretical DFT calculations and experimental Raman data. In addition, using the DFT/GGA + U formalism, we found the bandgap of 1.83 eV theoretically, which was much closer to the experimental data, than calculated values has been reported previously.

Phosphorene was synthesized in 2014 for the first time, and since then it has been the focus of numerous research projects. This huge research attraction is due to the exceptional and intriguing properties of phosphorene. Its widely tunable band gap, strong in-plane anisotropy, and high carrier mobility make phosphorene the center of various fundamental studies. Recently, numerous theoretical studies have been conducted to investigate strain engineering to additionally tune the electronic structure of phosphorene and few-layer BP. Although several theoretical studies have predicted an electronic and structural phase transition in few-layer BP, there is not experimental study to indicate the transition.

In order to understand the effect of strain on structural, vibrational and electronic properties of few-layer black phosphorus (BP) and to verify the theoretical study with experimental data we applied high pressure up to ~14 GPa to the samples using diamond anvil cell. , Raman scattering data along with the group theory information was thoroughly investigated. We described and interpreted the evolution of vibrational modes of black phosphorene under high pressure. It was found that by increasing the pressure, all three prominent Raman peaks of orthorhombic few-layer BP underwent a blue shift,

but with different rates. The two B_{2g} and A_g^2 modes showed little pressure dependence. In contrast the A_g^1 modes showed strong pressure dependence. These behavior can be explained by the fact that B_{2g} and A_g^2 modes are related to deformation of the in plane atomic arrangement with strong bonding forces but A_g^1 modes correspond to out of plane weak van der Waals forces which are severely impacted by high pressure. Further Raman data analysis revealed existence of three distinct pressure regions signifying the crystal phase transition of the sample. Full Width Half Maximum (FWHM) of Raman peaks showed only a small decrease within the pressure range of zero to ~6.5 GPa while it increased significantly within the pressure ranges of 6.5 to 10 and 10 to 13.5 GPa, but with different rates.

For years, graphene and its derivatives have been explored intensively and remain in the center of attention in the field of materials science due to its extraordinary properties. Combinations of the tremendously large surface area, elegant electrical and thermal conductivity, superior chemical stability, and extreme mechanical strength make graphene an essential component for fabricating functional materials for a broad range of applications. However, practical limitations such as the difficulty of mass production of high-quality samples render a barrier to extensive implementation of graphene in practical devices. For example, during the processing of graphene into an actual device, the strong π - π interaction between graphene sheets cause the isolated graphene flakes to restack to form graphite-like powders which can substantially reduce the specific surface area and thereby result in inefficient utilization of the graphene layers.

To address these issues and to make full utilization of the high intrinsic surface area of graphene we developed and established a simple, inexpensive, and highly scalable method to grow graphene in the form of a three-dimensional network architecture. The technique is based on pyrolysis of organic materials, and it is almost identical to the conventional chemical vapor deposition (CVD) process except for use of solid organic sources of carbon instead of methane or other gas sources. We found that this method to be simpler, faster and more efficient compared to conventional CVD process.

Furthermore, three-dimensional graphene-based materials offer an easy and versatile platform for functionalization and integration into devices. Accordingly, 3D graphene materials and their derivatives triggered extensive studies for numerous potential applications in energy, electrochemistry, bioelectrochemistry and pollution management. High pore volume and the large surface area along with the intrinsic graphene properties, including high mechanical strength excellent electronic conductivity, and perfect thermal stability are additional advantageous of graphene 3D architectures. Several samples with various conditions before and during the growth were prepared using the pyrolysis (CVD with solid carbon source) method. The conditions variable were included surface treatments of Ni foam using different acids, annealing temperatures, the concentration of organic acids and mass flow rate of hydrogen and argon gasses. Based on post growth characterization, we found that the best quality samples of pure 3D graphene result from using of HCl for Ni surface etching, and the growth temperature of 1000 °C. In the case of nitrogen doped 3D graphene samples, 1:1 weight ratio solution of urea: citric-acid and 1000 °C growth temperature showed the highest nitrogen concentration and uniformity. The statistical analysis of Raman spectra of all samples grown at 1000 °C showed general

uniformity and high crystallinity of multilayered graphitic shells which were also, verified by electron microscopy. The effect of nitrogen doping of 3D graphene samples on their Raman spectra was well correlated with XPS results, i.e. the intensity of Raman D-band and the N (1s) XPS spectra; both were used as an indication of nitrogen concentration in the graphene structures. We also conducted an extensive statistical analysis of Raman data to establish a correlation with the quality of samples including coverage, uniformity, the number of graphitic layers, the crystallinity of the structure and concentration of defects.

The 3D graphene samples were used for electrochemical reduction of CO₂ gas. The electrochemical testing demonstrated a significant increase in catalytic activity when our synthesized 3D graphene foam was used as the core-shell of a layer of nitrogen-doped amorphous carbon. We compared catalytic activity of this combination with a nickel foam, a silver film, and a pure three-dimensional graphene foam (Figure 3.28).

REFERENCES

- 1 Ackland, G. J. High-Pressure Phases of Group Iv and Iii-V Semiconductors. *Reports on Progress in Physics* **64**, 483 (2001).
- 2 Schettino, V. & Bini, R. Constraining Molecules at the Closest Approach: Chemistry at High Pressure. *Chemical Society Reviews* **36**, 869-880, doi:10.1039/B515964B (2007).
- 3 Hemley, R. J. & Ashcroft, N. W. The Revealing Role of Pressure in the Condensed Matter Sciences. *Physics Today* **51**, 26-32, doi:10.1063/1.882374 (1998).
- 4 Jayaraman, A. The Diamond-Anvil High-Pressure Cell. *Scientific American* **250**, 54 - 62, doi:10.1038/scientificamerican0484-54 (1984).
- 5 Liebermann, R. C. Multi-Anvil, High Pressure Apparatus: A Half-Century of Development and Progress. *High Pressure Research* **31**, 493-532, doi:10.1080/08957959.2011.618698 (2011).
- 6 Dmitrii Yu, P. Minerals of the Deep Geospheres. *Physics-Uspekhi* **45**, 439 (2002).
- 7 Kim, M., Dias, R., Ohishi, Y., Matsuoka, T., Chen, J.-Y. & Yoo, C.-S. Pressure-Induced Transformations of Dense Carbonyl Sulfide to Singly Bonded Amorphous Metallic Solid. *Scientific Reports* **6**, 31594, doi:10.1038/srep31594 <https://www.nature.com/articles/srep31594#supplementary-information> (2016).
- 8 Russell, J. H. A Pressing Matter. *Physics World* **19**, 26 (2006).

- 9 McMillan, P. F. Chemistry at High Pressure. *Chemical Society Reviews* **35**, 855-857, doi:10.1039/B610410J (2006).
- 10 Thompson, W. & Hanrahan, S. Characteristics of a Cryogenic Extreme High-Vacuum Chamber. *Journal of Vacuum Science & Technology* **14**, 643-645, doi:doi:http://dx.doi.org/10.1116/1.569168 (1977).
- 11 Dubrovinsky, L., Dubrovinskaia, N., Bykova, E., Bykov, M., Prakapenka, V., Prescher, C., Glazyrin, K., Liermann, H. P., Hanfland, M., Ekholm, M., Feng, Q., Pourovskii, L. V., Katsnelson, M. I., Wills, J. M. & Abrikosov, I. A. The Most Incompressible Metal Osmium at Static Pressures above 750 Gigapascals. *Nature* **525**, 226-229, doi:10.1038/nature14681 (2015).
- 12 George, V. T., Brooks, G. & Humphrey, T. C. Regulation of Cell Cycle and Stress Responses to Hydrostatic Pressure in Fission Yeast. *Molecular Biology of the Cell* **18**, 4168-4179, doi:10.1091/mbc.E06-12-1141 (2007).
- 13 Schettino, V., Bini, R., Ceppatelli, M. & Citroni, M. Activation and Control of Chemical Reactions at Very High Pressure. *Physica Scripta* **78**, 058104, doi:10.1088/0031-8949/78/05/058104 (2008).
- 14 Badding, J. V., Parker, L. J. & Nesting, D. C. High Pressure Synthesis of Metastable Materials. *Journal of Solid State Chemistry* **117**, 229-235, doi:http://dx.doi.org/10.1006/jssc.1995.1268 (1995).
- 15 Bini, R., Ceppatelli, M., Citroni, M. & Schettino, V. From Simple to Complex and Backwards. Chemical Reactions under Very High Pressure. *Chemical Physics* **398**, 262-268, doi:10.1016/j.chemphys.2011.04.021 (2012).

- 16 Hamad R. Jappor1, M. A. A. a. A. M. A.-I. Electronic Structure of Alp under Pressure Using Semiempirical Method. doi:10.2174/1874186X01003010001 (2010).
- 17 Hung, V. V., Masuda-Jindo, K., Hanh, P. T. M. & Hai, N. T. Equation of States and Melting Temperatures of Diamond Cubic and Zinblende Semiconductors: Pressure Dependence. *Journal of Physics: Conference Series* **98**, 032001 (2008).
- 18 Sherman, M. S. Going to Extremes. *Science & Technology Review* **July/August 2004** (2004).
- 19 Yin, M. T. & Cohen, M. L. Theory of Static Structural Properties, Crystal Stability, and Phase Transformations: Application to Si and Ge. *Physical Review B* **26**, 5668-5687 (1982).
- 20 Car, R. & Parrinello, M. Unified Approach for Molecular Dynamics and Density-Functional Theory. *Physical Review Letters* **55**, 2471-2474 (1985).
- 21 Saib, S. & Bouarissa, N. High-Pressure Band Parameters for Gaas: First Principles Calculations. *Solid-State Electronics* **50**, 763-768, doi:http://doi.org/10.1016/j.sse.2006.04.002 (2006).
- 22 Hohenberg, P. & Kohn, W. Inhomogeneous Electron Gas. *Physical Review* **136**, B864-B871 (1964).
- 23 Kohn, W. & Sham, L. J. Self-Consistent Equations Including Exchange and Correlation Effects. *Physical Review* **140**, A1133-A1138 (1965).
- 24 Perdew, J. P. & Zunger, A. Self-Interaction Correction to Density-Functional Approximations for Many-Electron Systems. *Physical Review B* **23**, 5048-5079 (1981).

- 25 Perdew, J. P. & Wang, Y. Accurate and Simple Analytic Representation of the
Electron-Gas Correlation Energy. *Physical Review B* **45**, 13244-13249 (1992).
- 26 Ceperley, D. M. & Alder, B. J. Ground State of the Electron Gas by a Stochastic
Method. *Physical Review Letters* **45**, 566-569 (1980).
- 27 Perdew, J. P., Burke, K. & Ernzerhof, M. Generalized Gradient Approximation
Made Simple. *Physical Review Letters* **77**, 3865-3868 (1996).
- 28 Brazhkin, V. V. High-Pressure Synthesized Materials: Treasures and Hints. *High
Pressure Research* **27**, 333-351, doi:10.1080/08957950701546956 (2007).
- 29 San-Miguel, A. Nanomaterials under High-Pressure. *Chem Soc Rev* **35**, 876-889,
doi:10.1039/b517779k (2006).
- 30 Gérard, D. High Pressure in Solid-State Chemistry. *Journal of Physics:
Condensed Matter* **14**, 11031-11035 (2002).
- 31 "Fritz Haber - Biographical". Nobelprize.Org. Nobel Media Ab 2014.
<[Http://Www.Nobelprize.Org/Nobel_Prizes/Chemistry/Laureates/1918/Haber-
Bio.html](http://www.nobelprize.org/Nobel_Prizes/Chemistry/Laureates/1918/Haber-Bio.html)>.
- 32 "The Nobel Prize in Chemistry 1931". Nobelprize.Org. Nobel Media Ab 2014.
<[Http://Www.Nobelprize.Org/Nobel_Prizes/Chemistry/Laureates/1931/](http://www.nobelprize.org/Nobel_Prizes/Chemistry/Laureates/1931/)>,
<http://www.nobelprize.org/nobel_prizes/chemistry/laureates/1931/> (
- 33 "Percy W. Bridgman - Biographical". Nobelprize.Org. Nobel Media Ab 2014.
<[Http://Www.Nobelprize.Org/Nobel_Prizes/Physics/Laureates/1946/Bridgman-
Bio.html](http://www.nobelprize.org/Nobel_Prizes/Physics/Laureates/1946/Bridgman-Bio.html)>.

- 34 Relaxation of the Structure of Simple Metal Ion Complexes in Aqueous Solutions at up to Supercritical Conditions. *The Journal of Chemical Physics* **118**, 719-727, doi:10.1063/1.1524616 (2002).
- 35 Catalli, K., Shim, S.-H. & Prakapenka, V. Thickness and Clapeyron Slope of the Post-Perovskite Boundary. *Nature* **462**, 782-785, doi:http://www.nature.com/nature/journal/v462/n7274/supinfo/nature08598_S1.html (2009).
- 36 New Developments in Laser-Heated Diamond Anvil Cell with in Situ Synchrotron X-Ray Diffraction at High Pressure Collaborative Access Team. *Review of Scientific Instruments* **86**, 072201, doi:10.1063/1.4926895 (2015).
- 37 Paszkowicz, W. High-Pressure Powder X-Ray Diffraction at the Turn of the Century. *Nuclear Instruments & Methods in Physics Research Section B-Beam Interactions with Materials and Atoms* **198**, 142-182, doi:10.1016/s0168-583x(02)01129-1 (2002).
- 38 Brister, K. X-Ray Diffraction and Adsorption at Extreme Pressures. *Review of Scientific Instruments* **68**, 1629-1647, doi:10.1063/1.1147969 (1997).
- 39 Lange, R. & Balny, C. Uv-Visible Derivative Spectroscopy under High Pressure. *Biochimica Et Biophysica Acta-Protein Structure and Molecular Enzymology* **1595**, 80-93, doi:10.1016/s0167-4838(01)00336-3 (2002).
- 40 Boffa Ballaran, T., Kurnosov, A. & Trots, D. Single-Crystal X-Ray Diffraction at Extreme Conditions: A Review. *High Pressure Research* **33**, 453-465, doi:10.1080/08957959.2013.834052 (2013).

- 41 Ballaran, T. B., Kurnosov, A. & Trots, D. Single-Crystal X-Ray Diffraction at Extreme Conditions: A Review. *High Pressure Research* **33**, 453-465, doi:10.1080/08957959.2013.834052 (2013).
- 42 Li, M., Gao, C.-X., Ma, Y.-Z., He, C.-Y., Hao, A.-M., Zhang, D.-M., Li, Y.-C., Liu, J. & Wang, D.-J. Resistivity Measurement of Molten Olivine in a Laser-Heated Diamond Anvil Cell. *Chinese Physics Letters* **24**, 1010 (2007).
- 43 New Diamond Anvil Cell System for in Situ Resistance Measurement under Extreme Conditions. *Review of Scientific Instruments* **77**, 123902, doi:10.1063/1.2400669 (2006).
- 44 Yang, J., Liu, C.-L. & Gao, C.-X. In Situ Electrical Resistance and Activation Energy of Solid C 60 under High Pressure. *Chinese Physics B* **22**, 096202 (2013).
- 45 Ménez, B., Bureau, H., Cauzid, J., Malavergne, V., Somogyi, A., Simionovici, A., Munoz, M., Avoscan, L., Rommevaux-Jestin, C. & Gouget, B. in *Modern Research and Educational Topics in Microscopy* (ed J. Díaz A. Méndez-Vilas) 976 à 988 (Formatex, 2007).
- 46 Torchio, R., Mathon, O. & Pascarelli, S. Xas and XmcD Spectroscopies to Study Matter at High Pressure: Probing the Correlation between Structure and Magnetism in the 3d Metals. *Coordination Chemistry Reviews* **277**, 80-94, doi:10.1016/j.ccr.2014.02.024 (2014).
- 47 Liu, A. & Song, Y. In Situ High-Pressure and Low-Temperature Study of Ammonia Borane by Raman Spectroscopy. *The Journal of Physical Chemistry C* **116**, 2123-2131, doi:10.1021/jp205962g (2012).

- 48 Tiwari, A., Butler, I. S. & Kozinski, J. A. A Brief Overview of the Effect of High Pressures on the Vibrational Spectra of Biomaterials. *Applied Spectroscopy Reviews* **44**, 552-567, doi:10.1080/05704920903178421 (2009).
- 49 Goncharov, A. F. & Struzhkin, V. V. Raman Spectroscopy of Metals, High-Temperature Superconductors and Related Materials under High Pressure. *Journal of Raman Spectroscopy* **34**, 532-548, doi:10.1002/jrs.1030 (2003).
- 50 Edwards, G. M. & Butler, I. S. Pressure-Tuning Spectroscopy of Inorganic Compounds: A Summary of the Past 15 Years. *Coordination Chemistry Reviews* **199**, 1-53 (2000).
- 51 Lowitzer, S., Winkler, B. & Tucker, M. Thermoelastic Behavior of Graphite from in Situ High-Pressure High-Temperature Neutron Diffraction. *Physical Review B* **73**, 214115 (2006).
- 52 Nasu, S. High Pressure Mössbauer Spectroscopy Using a Diamond Anvil Cell. *Hyperfine Interactions* **90**, 59-75, doi:10.1007/BF02069118 (1994).
- 53 ⁵⁷Fe Mössbauer Spectroscopy in a Diamond-Anvil Cell at Variable High Pressures and Cryogenic Temperatures. *Review of Scientific Instruments* **65**, 3787-3792, doi:10.1063/1.1144508 (1994).
- 54 In Situ Impedance Measurements in Diamond Anvil Cell under High Pressure. *Review of Scientific Instruments* **81**, 013904, doi:10.1063/1.3282444 (2010).
- 55 In Situ Hall Effect Measurement on Diamond Anvil Cell under High Pressure. *Review of Scientific Instruments* **81**, 115101, doi:10.1063/1.3501384 (2010).

- 56 Shimizu, H., Imaeda, H., Kume, T. & Sasaki, S. High-Pressure Elastic Properties of Liquid and Solid Neon to $0.3 \text{ ex} \text{ GPa}$. *Physical Review B* **71**, 014108 (2005).
- 57 Shimizu, H. High-Pressure in Situ Brillouin Spectroscopy in a Diamond-Anvil Cell. *High Pressure Research* **24**, 491-498, doi:10.1080/08957950412331331772 (2004).
- 58 Hu, Y., Kazemian, H., Rohani, S., Huang, Y. & Song, Y. In Situ High Pressure Study of Zif-8 by Ftir Spectroscopy. *Chemical Communications* **47**, 12694-12696, doi:10.1039/C1CC15525C (2011).
- 59 Wang, Z. P., Tang, X. D. & Ding, Z. J. Raman and Photoluminescence Spectroscopy Study of Benzoic Acid at High Pressures. *Journal of Physics and Chemistry of Solids* **66**, 895-901, doi:https://doi.org/10.1016/j.jpcs.2004.10.013 (2005).
- 60 Spain, I. L. Semiconductors at High Pressure: New Physics with the Diamond-Anvil Cell. *Contemporary Physics* **28**, 523-546, doi:10.1080/00107518708213742 (1987).
- 61 Guoyin, S. & Ho Kwang, M. High-Pressure Studies with X-Rays Using Diamond Anvil Cells. *Reports on Progress in Physics* **80**, 016101 (2017).
- 62 Bi, W., Zhao, J., Lin, J.-F., Jia, Q., Hu, M. Y., Jin, C., Ferry, R., Yang, W., Struzhkin, V. & Alp, E. E. Nuclear Resonant Inelastic X-Ray Scattering at High Pressure and Low Temperature. *Journal of Synchrotron Radiation* **22**, 760-765, doi:10.1107/S1600577515003586 (2015).

- 63 Jacobsen, S. D., Spetzler, H., Reichmann, H. J. & Smyth, J. R. Shear Waves in the Diamond-Anvil Cell Reveal Pressure-Induced Instability in (Mg,Fe)O. *Proceedings of the National Academy of Sciences of the United States of America* **101**, 5867-5871, doi:10.1073/pnas.0401564101 (2004).
- 64 Bassett, W. A., Reichmann, H.-J., Angel, R. J., Spetzler, H. & Smyth, J. R. New Diamond Anvil Cells for Gigahertz Ultrasonic Interferometry and X-Ray Diffraction. *American Mineralogist* **85**, 283-287 (2000).
- 65 Pressure-Enhanced Crystallization Kinetics of Amorphous Si and Ge: Implications for Point-Defect Mechanisms. *Journal of Applied Physics* **70**, 5323-5345, doi:10.1063/1.350243 (1991).
- 66 Schettino, V., Bini, R., Ceppatelli, M., Ciabini, L. & Citroni, M. in *Advances in Chemical Physics, Vol 131* Vol. 131 *Advances in Chemical Physics* (ed S. A. Rice) 105-242 (2005).
- 67 Schettino, V. & Bini, R. Molecules under Extreme Conditions: Chemical Reactions at High Pressure. *Physical Chemistry Chemical Physics* **5**, 1951-1965, doi:10.1039/b301381b (2003).
- 68 Hemley, R. J. Effects of High Pressure on Molecules. *Annual Review of Physical Chemistry* **51**, 763-800 (2000).
- 69 Sleight, A. W. New Ternary Oxides of Mercury with the Pyrochlore Structure. *Inorganic Chemistry* **7**, 1704-1708, doi:10.1021/ic50067a003 (1968).
- 70 Knyrim, J. S., Friedrichs, J., Neumair, S., Roessner, F., Floredo, Y., Jakob, S., Johrendt, D., Glaum, R. & Huppertz, H. High-Pressure Syntheses and Characterization of the Transition Metal Borates Beta-Mb₄O₇ (M = Mn²⁺, Ni²⁺,

- Cu²⁺). *Solid State Sciences* **10**, 168-176,
doi:10.1016/j.solidstatesciences.2007.09.004 (2008).
- 71 Fujinaka, H., Kinomura, N., Miyamota, Y., Kume, S. & Koizumi, M. in *7th Internat. AIRAPT Confer. High Pres. Sci. Techn.* 1st edn 556-557 (Pergamon Press, 1980).
- 72 Akhtar, M., Menon, M., Sunkara, M., Sumanasekera, G., Durygin, A. & Jasinski, J. B. High-Pressure Synthesis of Rhombohedral A-Ag₂O₂ Via Direct Solid State Reaction. *Journal of Alloys and Compounds* **641**, 87-92,
doi:10.1016/j.jallcom.2015.04.051 (2015).
- 73 L'Vov, B. V. Kinetics and Mechanism of Thermal Decomposition of Silver Oxide. *Thermochimica Acta* **333**, 13-19, doi:http://dx.doi.org/10.1016/S0040-6031(99)00085-4 (1999).
- 74 Herley, P. J. & Prout, E. G. The Thermal Decomposition of Silver Oxide. *Journal of the American Chemical Society* **82**, 1540-1543, doi:10.1021/ja01492a006 (1960).
- 75 Benton, A. F. & Drake, L. C. Kinetics of Reaction and Adsorption in the System Silver-Oxygen. *Journal of the American Chemical Society* **56**, 255-263,
doi:10.1021/ja01317a001 (1934).
- 76 Gallardo, O. A. D., Moiraghi, R., Macchione, M. A., Godoy, J. A., Perez, M. A., Coronado, E. A. & Macagno, V. A. Silver Oxide Particles/Silver Nanoparticles Interconversion: Susceptibility of Forward/Backward Reactions to the Chemical Environment at Room Temperature. *Royal Society of Chemistry Advances* **2**, 2923-2929, doi:10.1039/C2RA01044E (2012).

- 77 Maruyama, Y., Irie, H. & Hashimoto, K. Visible Light Sensitive Photocatalyst, Delafossite Structured Alpha-AggaO₂. *J. Phys. Chem. B* **110**, 23274-23278, doi:10.1021/jp063406s (2006).
- 78 Shahriari, D. Y., Erdman, N., Haug, U. T. M., Zarzyczny, M. C., Marks, L. D. & Poeppelmeier, K. R. Direct Synthesis of AgInO₂. *Journal of Physics and Chemistry of Solids* **64**, 1437-1441, doi:http://dx.doi.org/10.1016/S0022-3697(03)00115-X (2003).
- 79 SHANNON, R. D., ROGERS, D. B. & PREWITT, C. T. Chemistry of Noble Metal Oxides. I. Syntheses and Properties of ABO₂ Delafossite Compounds. *Inorganic Chemistry* **10**, 713-718 (1971).
- 80 Nagarajan, R. & Tomar, N. Ultrasound Assisted Ambient Temperature Synthesis of Ternary Oxide AgMO₂ (M=Fe, Ga). *Journal of Solid State Chemistry* **182**, 1283-1290, doi:10.1016/j.jssc.2009.01.043 (2009).
- 81 Sheets, W. C., Stamper, E. S., Bertoni, M. I., Sasaki, M., Marks, T. J., Mason, T. O. & Poeppelmeier, K. R. Silver Delafossite Oxides. *Inorg. Chem.* **47**, 2696-2705, doi:10.1021/ic702197h (2008).
- 82 Sheets, W. C., Mugnier, E., Barnabe, A., Marks, T. J. & Poeppelmeier, K. R. Hydrothermal Synthesis of Delafossite-Type Oxides. *Chem. Mater.* **18**, 7-20, doi:10.1021/cm051791c (2006).
- 83 Gao, H. & Duan, H. 2d and 3d Graphene Materials: Preparation and Bioelectrochemical Applications. *Biosensors & Bioelectronics* **65**, 404-419, doi:10.1016/j.bios.2014.10.067 (2015).

- 84 Fan, X., Chen, X. & Dai, L. 3d Graphene Based Materials for Energy Storage. *Current Opinion in Colloid & Interface Science* **20**, 429-438, doi:10.1016/j.cocis.2015.11.005 (2015).
- 85 Zhou, G., Ye, Z., Shi, W., Liu, J. & Xi, F. Applications of Three Dimensional Graphene and Its Composite Materials. *Progress in Chemistry* **26**, 950-960, doi:10.7536/pc131250 (2014).
- 86 Luo, B. & Zhi, L. Design and Construction of Three Dimensional Graphene-Based Composites for Lithium Ion Battery Applications. *Energy & Environmental Science* **8**, 456-477, doi:10.1039/c4ee02578d (2015).
- 87 Jiang, L. & Fan, Z. Design of Advanced Porous Graphene Materials: From Graphene Nanomesh to 3d Architectures. *Nanoscale* **6**, 1922-1945, doi:10.1039/c3nr04555b (2014).
- 88 Shen, Y., Fang, Q. & Chen, B. Environmental Applications of Three-Dimensional Graphene-Based Macrostructures: Adsorption, Transformation, and Detection. *Environmental Science & Technology* **49**, 67-84, doi:10.1021/es504421y (2015).
- 89 Liu, X., Kou, Z. & Mu, S. Porous Graphene Materials. *Progress in Chemistry* **27**, 1566-1577, doi:10.7536/pc150508 (2015).
- 90 Han, S., Wu, D., Li, S., Zhang, F. & Feng, X. Porous Graphene Materials for Advanced Electrochemical Energy Storage and Conversion Devices. *Advanced Materials* **26**, 849-864, doi:10.1002/adma.201303115 (2014).
- 91 Xu, P., Yang, J., Wang, K., Zhou, Z. & Shen, P. Porous Graphene: Properties, Preparation, and Potential Applications. *Chinese Science Bulletin* **57**, 2948-2955, doi:10.1007/s11434-012-5121-3 (2012).

- 92 Yang, Z., Chabi, S., Xia, Y. & Zhu, Y. Preparation of 3d Graphene-Based Architectures and Their Applications in Supercapacitors. *Progress in Natural Science-Materials International* **25**, 554-562, doi:10.1016/j.pnsc.2015.11.010 (2015).
- 93 Zeng, M., Wang, W.-L. & Bai, X.-D. Preparing Three-Dimensional Graphene Architectures: Review of Recent Developments. *Chinese Physics B* **22**, doi:10.1088/1674-1056/22/9/098105 (2013).
- 94 Yan, Z., Yao, W., Hu, L., Liu, D., Wang, C. & Lee, C.-S. Progress in the Preparation and Application of Three-Dimensional Graphene-Based Porous Nanocomposites. *Nanoscale* **7**, 5563-5577, doi:10.1039/c5nr00030k (2015).
- 95 Zhang, X., Zhang, H., Li, C., Wang, K., Sun, X. & Ma, Y. Recent Advances in Porous Graphene Materials for Supercapacitor Applications. *Rsc Advances* **4**, 45862-45884, doi:10.1039/c4ra07869a (2014).
- 96 Xu, Y., Shi, G. & Duan, X. Self-Assembled Three-Dimensional Graphene Macrostructures: Synthesis and Applications in Supercapacitors. *Accounts of Chemical Research* **48**, 1666-1675, doi:10.1021/acs.accounts.5b00117 (2015).
- 97 Fang, Q., Shen, Y. & Chen, B. Synthesis, Decoration and Properties of Three-Dimensional Graphene-Based Macrostructures: A Review. *Chemical Engineering Journal* **264**, 753-771, doi:10.1016/j.cej.2014.12.001 (2015).
- 98 Russo, P., Hu, A. & Compagnini, G. Synthesis, Properties and Potential Applications of Porous Graphene: A Review. *Nano-Micro Letters* **5**, 260-273, doi:10.5101/nml.v5i4.p260-273 (2013).

- 99 Wang, H., Yuan, X., Zeng, G., Wu, Y., Liu, Y., Jiang, Q. & Gu, S. Three Dimensional Graphene Based Materials: Synthesis and Applications from Energy Storage and Conversion to Electrochemical Sensor and Environmental Remediation. *Advances in Colloid and Interface Science* **221**, 41-59, doi:10.1016/j.cis.2015.04.005 (2015).
- 100 Xia, X. H., Chao, D. L., Zhang, Y. Q., Shen, Z. X. & Fan, H. J. Three-Dimensional Graphene and Their Integrated Electrodes. *Nano Today* **9**, 785-807, doi:10.1016/j.nantod.2014.12.001 (2014).
- 101 Cao, X., Yin, Z. & Zhang, H. Three-Dimensional Graphene Materials: Preparation, Structures and Application in Supercapacitors. *Energy & Environmental Science* **7**, 1850-1865, doi:10.1039/c4ee00050a (2014).
- 102 Ma, Y. & Chen, Y. Three-Dimensional Graphene Networks: Synthesis, Properties and Applications. *National Science Review* **2**, 40-53, doi:10.1093/nsr/nwu072 (2015).
- 103 Mao, S., Lu, G. & Chen, J. Three-Dimensional Graphene-Based Composites for Energy Applications. *Nanoscale* **7**, 6924-6943, doi:10.1039/c4nr06609j (2015).
- 104 Ji, X., Zhang, X. & Zhang, X. Three-Dimensional Graphene-Based Nanomaterials as Electrocatalysts for Oxygen Reduction Reaction. *Journal of Nanomaterials*, doi:10.1155/2015/357196 (2015).
- 105 Novoselov, K. S., Geim, A. K., Morozov, S. V., Jiang, D., Zhang, Y., Dubonos, S. V., Grigorieva, I. V. & Firsov, A. A. Electric Field Effect in Atomically Thin Carbon Films. *Science* **306**, 666-669, doi:10.1126/science.1102896 (2004).

- 106 Eswaraiyah, V., Zeng, Q., Long, Y. & Liu, Z. Black Phosphorus Nanosheets: Synthesis, Characterization and Applications. *Small* **12**, 3480-3502, doi:10.1002/sml.201600032 (2016).
- 107 Butler, S. Z., Hollen, S. M., Cao, L., Cui, Y., Gupta, J. A., Gutierrez, H. R., Heinz, T. F., Hong, S. S., Huang, J. & Ismach, A. F. Progress, Challenges, and Opportunities in Two-Dimensional Materials Beyond Graphene. *ACS Nano* **7**, 2898-2926 (2013).
- 108 Bhimanapati, G. R., Lin, Z., Meunier, V., Jung, Y., Cha, J., Das, S., Xiao, D., Son, Y., Strano, M. S. & Cooper, V. R. Recent Advances in Two-Dimensional Materials Beyond Graphene. *ACS Nano* **9**, 11509-11539 (2015).
- 109 Xu, M., Liang, T., Shi, M. & Chen, H. Graphene-Like Two-Dimensional Materials. *Chemical reviews* **113**, 3766-3798, doi:10.1021/cr300263a (2013).
- 110 Akhtar, M., Anderson, G., Zhao, R., Alruqi, A., Mroczkowska, J. E., Sumanasekera, G. & Jasinski, J. B. Recent Advances in Synthesis, Properties, and Applications of Phosphorene. *npj 2D Materials and Applications* **1**, 5, doi:10.1038/s41699-017-0007-5 (2017).
- 111 Ferrari, A. C., Bonaccorso, F., Fal'Ko, V., Novoselov, K. S., Roche, S., Bøggild, P., Borini, S., Koppens, F. H., Palermo, V. & Pugno, N. Science and Technology Roadmap for Graphene, Related Two-Dimensional Crystals, and Hybrid Systems. *Nanoscale* **7**, 4598-4810 (2015).
- 112 Guo, G.-C., Wei, X.-L., Wang, D., Luo, Y. & Liu, L.-M. Pristine and Defect-Containing Phosphorene as Promising Anode Materials for Rechargeable Li

- Batteries. *Journal of Materials Chemistry A* **3**, 11246-11252, doi:10.1039/C5TA01661D (2015).
- 113 Xia, F., Wang, H. & Jia, Y. Rediscovering Black Phosphorus as an Anisotropic Layered Material for Optoelectronics and Electronics. *Nature Communications* **5** (2014).
- 114 Liu, H., Neal, A. T., Zhu, Z., Luo, Z., Xu, X., Tomanek, D. & Ye, P. D. Phosphorene: An Unexplored 2d Semiconductor with a High Hole Mobility. *ACS Nano* **8**, 4033-4041, doi:10.1021/nn501226z (2014).
- 115 Bridgman, P. W. Two New Modifications of Phosphorus. *Journal of the American Chemical Society* **36**, 1344-1363, doi:10.1021/ja02184a002 (1914).
- 116 Rodin, A. S., Carvalho, A. & Castro Neto, A. H. Strain-Induced Gap Modification in Black Phosphorus. *Physical Review Letters* **112**, 176801 (2014).
- 117 Castellanos-Gomez, A., Vicarelli, L., Prada, E., Island, J. O., Narasimha-Acharya, K. L., Blanter, S. I., Groenendijk, D. J., Buscema, M., Steele, G. A., Alvarez, J. V., Zandbergen, H. W., Palacios, J. J. & van der Zant, H. S. J. Isolation and Characterization of Few-Layer Black Phosphorus. *2D Materials* **1**, doi:10.1088/2053-1583/1/2/025001 (2014).
- 118 Appalakondaiah, S., Vaitheeswaran, G., Lebegue, S., Christensen, N. E. & Svane, A. Effect of Van Der Waals Interactions on the Structural and Elastic Properties of Black Phosphorus. *Physical Review B* **86**, doi:10.1103/PhysRevB.86.035105 (2012).
- 119 Dubrovinskaia, N., Dubrovinsky, L., Solopova, N. A., Abakumov, A., Turner, S., Hanfland, M., Bykova, E., Bykov, M., Prescher, C., Prakapenka, V. B.,

- Petitgirard, S., Chuvashova, I., Gasharova, B., Mathis, Y.-L., Ershov, P., Snigireva, I. & Snigirev, A. Terapascal Static Pressure Generation with Ultrahigh Yield Strength Nanodiamond. *Science Advances* **2**, doi:10.1126/sciadv.1600341 (2016).
- 120 Bassett, W. Diamond Anvil Cell, 50th Birthday. *International Journal of High Pressure Research* **29**, 163-186, doi:10.1080/08957950802597239 (2009).
- 121 Briggs, R. *In Situ Study of Polymorphism and Melting of Metals and Compounds under Extreme Conditions of High Pressure and High Temperature* Doctor of Philosophy thesis, University College London, (2012).
- 122 Characteristics of Silicone Fluid as a Pressure Transmitting Medium in Diamond Anvil Cells. *Review of Scientific Instruments* **75**, 4450-4454, doi:10.1063/1.1786355 (2004).
- 123 Evaluation of the Hydrostaticity of a Helium-Pressure Medium with Powder X-Ray Diffraction Techniques. *Journal of Applied Physics* **89**, 662-668, doi:10.1063/1.1328410 (2000).
- 124 Pressure Transmitting Medium for Fragile Structure or Single Crystal. *Review of Scientific Instruments* **38**, 135-136, doi:10.1063/1.1720510 (1967).
- 125 Wang, Q., He, D., Peng, F., Lei, L., Xiong, L., Wang, P. & Liu, J. Pressure Transmitting Medium-Dependent Structure Stability of Nanoanatase TiO₂ under High Pressure. *High Pressure Research* **34**, 259-265, doi:10.1080/08957959.2014.892939 (2014).
- 126 Adams, D. M., Appleby, R. & Sharma, S. K. Spectroscopy at Very High Pressures. X. Use of Ruby R-Lines in the Estimation of Pressure at Ambient and

- at Low Temperatures. *Journal of Physics E: Scientific Instruments* **9**, 1140 (1976).
- 127 Forman, R. A., Piermarini, G. J., Barnett, J. D. & Block, S. Pressure Measurement Made by the Utilization of Ruby Sharp-Line Luminescence. *Science* **176**, 284-285, doi:10.1126/science.176.4032.284 (1972).
- 128 Calibration of the Pressure Dependence of the R1 Ruby Fluorescence Line to 195 Kbar. *Journal of Applied Physics* **46**, 2774-2780, doi:10.1063/1.321957 (1975).
- 129 An Optical Fluorescence System for Quantitative Pressure Measurement in the Diamond-Anvil Cell. *Review of Scientific Instruments* **44**, 1-9, doi:10.1063/1.1685943 (1973).
- 130 Syassen, K. Ruby under Pressure. *High Pressure Research* **28**, 75-126, doi:10.1080/08957950802235640 (2008).
- 131 Dewaele, A., Torrent, M., Loubeyre, P. & Mezouar, M. Compression Curves of Transition Metals in the Mbar Range: Experiments and Projector Augmented-Wave Calculations. *Physical Review B* **78**, 104102 (2008).
- 132 Mao, H. K., Xu, J. & Bell, P. M. Calibration of the Ruby Pressure Gauge to 800 Kbar under Quasi-Hydrostatic Conditions. *Journal of Geophysical Research: Solid Earth* **91**, 4673-4676, doi:10.1029/JB091iB05p04673 (1986).
- 133 Köpf, M., Eckstein, N., Pfister, D., Grotz, C., Krüger, I., Greiwe, M., Hansen, T., Kohlmann, H. & Nilges, T. Access and in Situ Growth of Phosphorene-Precursor Black Phosphorus. *Journal of Crystal Growth* **405**, 6-10, doi:10.1016/j.jcrysgro.2014.07.029 (2014).

- 134 Lange, S., Schmidt, P. & Nilges, T. Au₃Sn₇@Black Phosphorus: An Easy Access to Black Phosphorus. *Inorganic Chemistry* **46**, 4028-4035, doi:10.1021/ic062192q (2007).
- 135 Nilges, T., Kersting, M. & Pfeifer, T. A Fast Low-Pressure Transport Route to Large Black Phosphorus Single Crystals. *Journal of Solid State Chemistry* **181**, 1707-1711, doi:10.1016/j.jssc.2008.03.008 (2008).
- 136 Kumar, S. & Gupta, H. C. Ab Initio Study of Structural, Bonding, and Vibrational Properties of Ag₂O (a=Ag,Cu) Delafossites. *Computational and Theoretical Chemistry* **977**, 78-85, doi:10.1016/j.comptc.2011.09.018 (2011).
- 137 Ouyang, S., Kikugawa, N., Chen, D., Zou, Z. & Ye, J. A Systematical Study on Photocatalytic Properties of Ag₂O₂ (M = Al, Ga, In): Effects of Chemical Compositions, Crystal Structures, and Electronic Structures. *Journal of Physical Chemistry C* **113**, 1560–1566, doi:10.1021/jp806513t (2009).
- 138 Mitchell, D. R. G. DiffTools: Electron Diffraction Software Tools for DigitalMicrograph™. *Microscopy Research and Technique* **71**, 588-593, doi:10.1002/jemt.20591 (2008).
- 139 Rodríguez-Carvajal, J. Recent Advances in Magnetic Structure Determination by Neutron Powder Diffraction. *Physica B* **192**, 55-69, doi:http://dx.doi.org/10.1016/0921-4526(93)90108-I (1993).
- 140 Andriotis, A. N., Mpourmpakis, G., Lisenkov, S., Sheetz, R. M. & Menon, M. U- Calculation of the LSDA+U Functional Using the Hybrid B3LYP and HSE Functionals. *Physica Status Solidi (b)* **250**, 356-363, doi:10.1002/pssb.201248215 (2013).

- 141 Dudarev, S. L., Botton, G. A., Savrasov, S. Y., Humphreys, C. J. & Sutton, A. P. Electron-Energy-Loss Spectra and the Structural Stability of Nickel Oxide: An Lsda+U Study. *Physical Review B* **57**, 1505-1509 (1998).
- 142 Kresse, G. & Joubert, D. From Ultrasoft Pseudopotentials to the Projector Augmented-Wave Method. *Physical Review B* **59**, 1758-1775 (1999).
- 143 Martina, I., Wiesinger, R., Jembrih-Simbürger, D. & Schreiner, M. Micro-Raman Characterisation of Silver Corrosion Products: Instrumental Set up and Reference Database. *e-PS* **9**, 1-8 (2012).
- 144 Dong, H., Li, Z., Xu, X., Ding, Z., Wu, L., Wang, X. & Fu, X. Visible Light-Induced Photocatalytic Activity of Delafossite AgMo₂ (M=Al, Ga, In) Prepared Via a Hydrothermal Method. *Applied Catalysis B: Environmental* **89**, 551-556, doi:10.1016/j.apcatb.2009.01.018 (2009).
- 145 Ferrari, A. C. & Basko, D. M. Raman Spectroscopy as a Versatile Tool for Studying the Properties of Graphene. *Nat Nano* **8**, 235-246, doi:http://www.nature.com/nnano/journal/v8/n4/abs/nnano.2013.46.html#supplementary-information (2013).
- 146 Malard, L. M., Pimenta, M. A., Dresselhaus, G. & Dresselhaus, M. S. Raman Spectroscopy in Graphene. *Physics Reports* **473**, 51-87, doi:https://doi.org/10.1016/j.physrep.2009.02.003 (2009).
- 147 Ferrari, A. C. Raman Spectroscopy of Graphene and Graphite: Disorder, Electron-Phonon Coupling, Doping and Nonadiabatic Effects. *Solid State Communications* **143**, 47-57, doi:https://doi.org/10.1016/j.ssc.2007.03.052 (2007).

- 148 Wang, Y., Shao, Y., Matson, D. W., Li, J. & Lin, Y. Nitrogen-Doped Graphene and Its Application in Electrochemical Biosensing. *ACS Nano* **4**, 1790-1798, doi:10.1021/nn100315s (2010).
- 149 Wang, H., Maiyalagan, T. & Wang, X. Review on Recent Progress in Nitrogen-Doped Graphene: Synthesis, Characterization, and Its Potential Applications. *ACS Catalysis* **2**, 781-794, doi:10.1021/cs200652y (2012).
- 150 Feng, Y., Zhou, J., Du, Y., Miao, F., Duan, C. G., Wang, B. & Wan, X. Raman Spectra of Few-Layer Phosphorene Studied from First-Principles Calculations. *J Phys Condens Matter* **27**, 185302, doi:10.1088/0953-8984/27/18/185302 (2015).
- 151 Carvalho, A., Wang, M., Zhu, X., Rodin, A. S., Su, H. & Castro Neto, A. H. Phosphorene: From Theory to Applications. *Nature Reviews Materials* **1**, 16061, doi:10.1038/natrevmats.2016.61 (2016).
- 152 Fei, R. & Yang, L. Lattice Vibrational Modes and Raman Scattering Spectra of Strained Phosphorene. *Applied Physics Letters* **105**, 083120, doi:10.1063/1.4894273 (2014).
- 153 Akahama, Y., Kobayashi, M. & Kawamura, H. Raman Study of Black Phosphorus up to 13 Gpa. *Solid State Communications* **104**, 311-315, doi:http://dx.doi.org/10.1016/S0038-1098(97)00325-6 (1997).
- 154 Vanderborgh, C. A. & Schiferl, D. Raman Studies of Black Phosphorus from 0.25 to 7.7 Gpa at 15 K. *Physical Review B* **40**, 9595-9599, doi:10.1103/PhysRevB.40.9595 (1989).

- 155 Sugai, S. & Shirotani, I. Raman and Infrared Reflection Spectroscopy in Black Phosphorus. *Solid State Communications* **53**, 753-755, doi:http://dx.doi.org/10.1016/0038-1098(85)90213-3 (1985).
- 156 Pressure Dependence of the Lattice Vibration in the Orthorhombic and Rhombohedral Structures of Black Phosphorus. *Journal of the Physical Society of Japan* **50**, 3356-3361, doi:10.1143/JPSJ.50.3356 (1981).
- 157 Ribeiro-Soares, J., Almeida, R. M., Cançado, L. G., Dresselhaus, M. S. & Jorio, A. Group Theory for Structural Analysis and Lattice Vibrations in Phosphorene Systems. *Physical Review B* **91**, doi:10.1103/PhysRevB.91.205421 (2015).
- 158 Wang, Y., Cong, C., Fei, R., Yang, W., Chen, Y., Cao, B., Yang, L. & Yu, T. Remarkable Anisotropic Phonon Response in Uniaxially Strained Few-Layer Black Phosphorus. *Nano Research* **8**, 3944-3953, doi:10.1007/s12274-015-0895-7 (2015).
- 159 Long, D. A. Intensities in Raman Spectra. I. A Bond Polarizability Theory. *Proceedings of the Royal Society A: Mathematical, Physical and Engineering Sciences* **217**, 203-221, doi:10.1098/rspa.1953.0057 (1953).
- 160 Wu, J., Mao, N., Xie, L., Xu, H. & Zhang, J. Identifying the Crystalline Orientation of Black Phosphorus Using Angle-Resolved Polarized Raman Spectroscopy. *Angew Chem Int Ed Engl* **54**, 2366-2369, doi:10.1002/anie.201410108 (2015).
- 161 Clark, S. M., Jeon, K.-J., Chen, J.-Y. & Yoo, C.-S. Few-Layer Graphene under High Pressure: Raman and X-Ray Diffraction Studies. *Solid State Communications* **154**, 15-18, doi:10.1016/j.ssc.2012.10.002 (2013).

- 162 Pressure and Temperature-Dependent Raman Spectra of Mos₂ Film. *Applied Physics Letters* **109**, 242101, doi:10.1063/1.4968534 (2016).
- 163 Nayak, A. P., Pandey, T., Voiry, D., Liu, J., Moran, S. T., Sharma, A., Tan, C., Chen, C.-H., Li, L.-J., Chhowalla, M., Lin, J.-F., Singh, A. K. & Akinwande, D. Pressure-Dependent Optical and Vibrational Properties of Monolayer Molybdenum Disulfide. *Nano Letters* **15**, 346-353, doi:10.1021/nl5036397 (2015).
- 164 Raman Scattering of 2h-Mos₂ at Simultaneous High Temperature and High Pressure (up to 600 K and 18.5 Gpa). *AIP Advances* **6**, 035214, doi:10.1063/1.4944832 (2016).

CURRICULUM VITA

NAME: Meysam Akhtar

ADDRESS: Department of Physics and Astronomy

102 Natural Science Building

University of Louisville

Louisville KY 40292

[Linkedin.com/in/meysamakhtar](https://www.linkedin.com/in/meysamakhtar)

EDUCATION & EXPERTISE:

Ph.D., Physics

University of Louisville (UofL)

2013 – 2017

M.Sc., Physics

University of Louisville (UofL)

2010 – 2013

B.Sc., Physics

Shahid Beheshti University

2002 - 2007

AWARDS:

- Recipient of “Doctoral Dissertation Completion Award”, UofL, Spring

2017

- Recipient of “Conference Travel Fund”, UofL, 2016
- Recipient of “Graduate Research Fund”, School of Interdisciplinary, UofL, 2015
- Recipient of “John Dillon Jr Physics Fellowship”, UofL, 2012-13

REFEREED JOURNALS:

- Journal of Physics D: Applied Physics
- Journal of Physics: Condensed Matter
- Nanotechnology

PROFESSIONAL ASSOCIATIONS:

- Associate member of Institute of Physics (IOP)
- Member of American Physical Society (APS)
- Member of American Association for the Advancement of Science (AAAS)
- Member of American Chemical Society (ACS)
- Member of Materials Research Society (MRS)

PUBLICATIONS:

- **Akhtar, M.**, Menon, M., Sunkara, M., Sumanasekera, G., Durygin, A., & Jasinski, J., High-pressure synthesis of rhombohedral α -AgGaO₂ via direct solid state reaction, *Journal of Alloys and Compounds* 641 (2015) 87–92.
- **Akhtar, M.**, Anderson, G., Zhao, R., Alruqi, A., Mroczkowska, J., Sumanasekera, G., Jasinski, J., Recent Advances in Synthesis, Properties, and Applications of Phosphorene, *npj 2D Materials and Applications* 1, 5 (2017).

- Zhao, R., Jayasingha, R., Sherehiy, A., Dharmasena, R., **Akhtar, M.**, Jasinski, J., Wu, S., Henner, V., Sumanasekera, G., In Situ Transport Measurements and Band Gap Formation of Fluorinated Graphene, *J. Phys. Chem. C* 119 (2015), 20150-20155.
- Ziolkowska, D., Jangam, J., Rudakov, G., Paronyan, T., **Akhtar, M.**, Sumanasekera, G., Jasinski, J., Simple synthesis of highly uniform bilayer-carbon nanocages, *Carbon* 115 (2017) 617-624.
- Zhao, R., **Akhtar, M.**, Alruqi, A., Dharmasena, R., Jasinski, J., Thantirige, R., Sumanasekera, G., Electrical Transport Properties of Graphene Grown at Low Temperature Using Plasma Enhanced Chemical Vapor Deposition, *Materials Research Express* (ACCEPTED).

PRESENTATIONS:

- Akhtar, M., Dilip, J.J.S., Sumanasekera, G., Jasinski, J., “Pyrolysis Synthesis of Three-Dimensional Graphene Network for Energy Applications”, MRS Fall Meeting, Boston, MA (USA), Nov 29-Dec 4, 2015. (Poster)
- Akhtar, M., Pishgar, S., Sumanasekera, G., & Jasinski, J., “In-situ Raman and PL spectroscopy of phosphorene under high-pressure”, APS March Meeting, New Orleans, LA USA, March 13-17, 2017. (Talk)
- Akhtar, M., Menon, M., Sunkara, M., Sumanasekera, G., Durygin, A., & Jasinski, J., “High-Pressure Synthesis of Rhombohedral Delafossite Structured of α -AgGaO₂”, APS March Meeting, Baltimore, MD USA, March 14-18, 2016. (Talk)